



中国地质调查局自然资源航空物探遥感中心

科技论文汇编 (2018)

科学技术处（项目管理处）
二〇一九年三月

中国地质调查局自然资源航空物探遥感中心

科技论文汇编(二〇一八年)

目 录

一、综述

- 1 精细地质初议.....刘刚, 梁树能, 燕云鹏, 等 (001)
- 2 光谱地质遥感研究进展.....甘甫平, 董新丰, 闫柏琨, 等 (014)
- 3 海洋航空物探数据库建设情况.....王林飞, 薛典军, 李芳, 等 (033)
- 4 高光谱遥感地质矿产工程化应用进展及展望.....董新丰, 闫柏琨, 甘甫平, 等 (040)
- 5 国际军事地球科学会议发展脉络及特点.....孟庆奎, 高维, 王晨阳 (050)

二、地质与矿产

- 1 Marine strata morphology of the South Yellow Sea based on high-resolution aeromagnetic and airborne gravity data.....*TONG Jing, ZHANG Xuanjie, ZHANG Wan, et al* (055)
- 2 The Quantitative Inversion of Iron Ore under Strong Constrain in Panzhihua-Baima Districts in Sichuan Province Based on the High-Precision Aeromagnetic Survey
.....*GE Tengfei, He Jingzi, Yang Xue, et al* (067)
- 3 中国航磁大地构造单元划分.....熊盛青, 杨海, 丁燕云, 等 (078)
- 4 青藏高原西部湖泊与构造背景关系遥感研究.....刘刚, 燕云鹏, 刘建宇 (101)
- 5 三塘湖盆地航磁异常特征及油气资源远景预测.....舒晴, 朱晓颖, 高维, 等 (109)
- 6 四川盆地的重磁场特征及地质意义.....李冰, 宋燕兵, 王启, 等 (119)
- 7 基于航空高光谱遥感的沉积变型铁矿找矿预测.....董新丰, 闫柏琨, 李娜, 等 (128)
- 8 日照—连云港地区重磁异常特征及其构造意义.....张婉, 张玄杰, 佟晶, 等 (139)
- 9 珠江口盆地断裂构造特征及对沉积盆地的控制作用
.....夏玲燕, 林畅松, 李筱, 等 (147)
- 10 贵州铜仁地区南华系大塘坡组黑色页岩型菱锰矿碳、氧同位素特征及锰矿成矿作用
.....瞿永泽, 徐林刚, 毛景文, 等 (156)
- 11 黔东地区航磁特征与岩性构造填图.....王卫平, 吴成平, 马勋表, 等 (173)
- 12 新疆可可托海航磁调查及主要成果.....刘前坤, 尹航, 张凯淞, 等 (180)
- 13 华北准地台的北界和西界之我见.....李冰, 宋燕兵, 等 (188)
- 14 磁场资料在西昆仑地区构造研究中的应用.....林晓星, 吴云, 邹为雷 (192)

三、地质灾害与环境调查

- 1 Vegetation monitoring by remote sensing technology for uninhabited islands of the XiSha Islands.....*LI Li, GUO Ya* (198)
- 2 Remote sensing monitoring of wetland of SanYa and LingShui in HaiNan Province, based on GF data.....*GUO Ya, LI Li* (202)
- 3 Application of domestic high-resolution satellite data On Geological Hazard Monitoring in Coal Mining Areas.....*WANG Jie, WANF Hao, YAO Weiling* (206)

- 4 Mining Subsidence Monitoring Using TerraSAR-X Data
..... YUAN Weilin, Huang Bo, WANG Qun, et al (214)
- 5 Building digital topography model of the intertidal zone
..... ZHANG Zonggui, WU Fang, LI Tianqi, et al (220)
- 6 基于“DEM-NDVI-土地覆盖分类”的天山博格达自然遗产地植被垂直带提取与变化分析..... 冀欣阳, 骆磊, 王心源, 等 (227)
- 7 天津滨海新区重点海岸带土地生态景观综合分析与评价
..... 刘春玲, 王永, 姚翔龙, 等 (238)
- 8 山西某地矿业开发占用土地状况遥感监测..... 王海庆, 武明德, 刘琼, 等 (245)
- 9 海南岛东部滨海砂矿开发状况遥感监测与生态恢复治理对策研究
..... 赵玉灵, 杨金中, 殷亚秋, 等 (250)
- 10 粤港澳大湾区自然资源遥感调查与保护建议..... 赵玉灵 (259)
- 11 基于 GF-1 光谱数据的青藏地区冰川资源现状的遥感调查
..... 安国英, 韩磊, 黄树春, 等 (268)
- 12 基于遥感调查的矿山综合评价研究..... 王昊, 汪洁, 李浩, 等 (279)
- 13 西藏日喀则矿山环境恢复治理效果分析..... 王海庆, 陈玲 (282)
- 14 典型矿山尾矿化学成分研究——以新疆某铜镍尾矿库为例
..... 王昊, 李浩, 宋伊圩, 等 (286)
- 15 资源一号 02C 卫星在江西重点矿区开发监测中的应用
..... 汪洁, 李迁, 刘小杨, 等 (289)
- 16 地基 InSAR 技术及其典型边坡监测应用..... 刘斌, 葛大庆, 李曼, 等 (294)
- 17 新疆东北地区矿产资源开发环境遥感监测成果..... 王昊, 李丽, 刘雪, 等 (303)
- 18 煤矿开采用地土地集约利用评价研究——以山西省阳泉市 21 个井工煤矿为例
..... 许文佳, 叶达 (311)
- 19 基于地理信息的地质灾害危险性空间分布特征分析
..... 汪洁, 姚维岭, 孙娅琴, 等 (316)
- 20 高分遥感影像在第三次全国国土调查中的应用潜力评价——以重庆市为例
..... 孙禧勇, 苗箐, 王锦, 等 (319)
- 21 通天河沿自然保护分区矿山环境遥感调查..... 王昊, 安娜, 步凡, 等 (330)
- 22 基于多源遥感数据的雄安新区近 40 年城镇扩展分析
..... 孙禧勇, 苗箐, 于航, 等 (332)
- 23 基于 TerraSAR-X 数据的矿区地面沉陷监测研究..... 袁蔚林, 范景辉, 黄波, 等 (337)
- 24 基于遥感和航磁数据的丹江口水库地震控制因素分析
..... 李逸川, 余学中, 李皎皎, 等 (341)

四、理论与方法研究

- 1 Generalized FPAR estimation methods from various satellite sensors and validation
..... LIU Rongyuan, REN Huazhong, LIU Suhong, et al (345)

- 2 Geometric Accuracy Evaluation of High-Resolution Satellite Images Based
on Xianning Test Field.....ZHENG Xiongwei, HUANG Qi, WANG Jingjing, et al (363)
- 3 Potential of Sentinel-2 data for alteration extraction in coal-bed methane reservoirs
.....CHEN Li, YANG Xiucheng, Zhen Guangwei (374)
- 4 Comparison of Inversion Accuracy of Soil Copper Content from Vegetation Indices under
Different Spectral Resolution.....SUN Zhongqing, SHANF Kun, JIA Lingjun (387)
- 5 Comparison of Water Extraction Methods in Tibet Based on GF-1 Data
.....JIA Lingjun, SHANG Kun, LIU Jing, et al (395)
- 6 Emissivity image generation of Gaofen-5s thermal infrared bands using ASTER data
.....LIU Yao, XIAO Chenchao (404)
- 7 Mineral information extraction based on Gaofen-5 thermal infrared data
.....SHANG Kun (408)
- 8 Study on White Birch Identification in Northeastern China using Hyperspectral Remote
Sensing Data.....SHANG Kun, LIU Yao, XIAO Chenchao (412)
- 9 A Simple Shadow Area Processing Method.....WANG Haiqing (416)
- 10 Typical applications of airborne LiDAR technology in geological investigation
.....ZHENG Xiongwei , XIAO Chunlei (420)
- 11 Application of Object-oriented Classification with Hierarchical Multi-Scale Segmentation
for Information Extraction in Nonoc Nickel Mine, the Philippines
.....CHEN Li, LI Wei, ZHANG Xian , et al (425)
- 12 Ultiparameter joint transformations of potential field and application to gravity gradiometry
Processing.....LUO Yao, LUO Feng, ZHANG Wenzhi, et al (428)
- 13 Comparative Analysis of the Fusion Methods Based on GF-3 Radar and
GF-1 Multispectral Data.....FU Zhengbo, QI Jianwei, ZHANG Dandan, et al (435)
- 14 Sensitivity analysis about FLAASH model parameters
.....WANG Jie, QI Jianwei, ZHANG Dandan, et al (440)
- 15 全张量磁梯度数据解释的均衡边界识别及深度成像技术
.....舒晴, 马国庆, 刘财, 等 (445)
- 16 逆 Laplace 变换新算法及其在时间域电磁相应计算中的应用.....王萌, 罗维斌 (455)
- 17 AS350B3 型直升机在中高山航空物探测量中的优势
.....李健, 郭亮, 肖刚毅, 等 (463)
- 18 航磁全轴梯度异常特征研究.....周德文, 孟庆奎, 杨怡, 等 (470)
- 19 城市群地质环境演化空间信息智能服务框架.....张丹丹, 李曼, 傅征博, 等 (476)
- 20 UC-X 系列航空数码像机几何精度评价.....李京, 陈洁, 李奇, 等 (481)
- 21 基于航磁数据的三维地质建模研究.....侯征, 王天意, 于长春, 等 (485)
- 22 基于航空瞬变电磁法的宝清地区含水体分布特征研究.....何怡原, 梁盛军, 连晟 (498)
- 23 任意形状水平接地导线源瞬变电磁法一维正反演研究.....李展辉, 黄清华 (506)
- 24 机载激光雷达技术在滑坡调查中的应用—以三峡库区张家湾滑坡为例

.....	杜磊, 陈洁, 李敏敏, 等 (517)
25	地面沉降光栅立体图研究制作.....范景辉, 王如意, 赵红丽, 等 (525)
26	基于 RasterCatalog 的海量遥感数据存储及快速浏览技术研究随欣欣, 王彦佐, 晋佩东, 等 (531)
27	基于 MapGIS 和 ArcGIS 的遥感解译成果图件数据库设计与实现随欣欣, 眇素文 (536)
28	面向遥感业务应用的解译成果数据管理体系研究和构建随欣欣, 眇素文, 刘锟 (544)
29	天宫一号高光谱数据烃类微渗漏信息提取.....杨达昌 (550)
30	航空 γ 能谱低能区与高能区信息综合应用研究.....张虹, 周锡华, 米耀辉 (557)
31	低频电磁探测技术在煤层气富集区的应用.....陈理, 秦其明, 王楠, 等 (563)
32	CBERS-04 星 PAN/MUX 图像几何定位精度评价魏丹丹, 甘甫平, 尚坤, 等 (571)
33	基于交叉点不符值统计的航空重力测量质量评估方法...姜作喜, 张虹, 屈进红, 等 (576)
34	基于二维经验模式分解的重力资料多尺度分析.....李芳, 王林飞, 何辉 (584)
35	航空物探遥感地质资料定密工作初探与实践.....郑向向, 王宁, 陈瑶, 等 (591)
36	航磁梯度数据实测与计算对比研究.....贾志业, 安战锋, 赵廷严 (597)
37	基于 Hough 变换的重磁数据线性特征提取技术.....李芳, 王林飞, 何辉, 等 (600)
38	海岸带数字航空摄影质量控制与评价.....陈洁, 高子弘, 杜磊, 等 (610)
39	隔离网闸在地质数据信息化方面的应用探索.....刘宏娟 (617)
40	基于新疆哈密遥感地质资源评价综合应用试验场的资源一号 02C 卫星绝对辐射 定标研究.....魏丹丹, 肖晨超, 梁树能, 等 (620)
41	岩心成像光谱仪数据处理方法研究及应用.....董新丰, 闫柏琨, 李娜, 等 (624)
42	GXL 二次开发在国产卫星数据处理中的应用研究张伟, 齐建伟, 张丹丹, 等 (631)
43	海岸带航空物探遥感数据融合与成果集成表达分析张宗贵, 金鼎坚, 吴芳, 等 (638)
44	基于 Web 的在线协同式解译系统实现研究.....徐航, 孙嘉琪, 张振华, 等 (649)
45	论斜轴投影编制小比例尺世界地图.....李敬敏, 周伟, 何辉, 等 (653)
46	航空物探遥感地质信息服务需求分析.....郑向向, 王宁, 付小茗 (659)
47	基于航空高光谱数据的土壤重金属含量反演研究刘榕源, 闫柏琨, 甘甫平, 等 (672)
48	基于深度学习的高分遥感影像森林识别.....杨会赟, 闫柏琨, 刘榕源, 等 (681)
49	位场多参量联合转换及在航空重力梯度中的应用.....骆遥, 吴美平, 罗锋, 等 (686)
50	02C 卫星影像质量改进并行处理软件测试和产品质量评价孙禧勇, 蒋永华, 步凡, 等 (692)

五、其他

- 1 《国土资源遥感》载文情况及高被引论文分析·····陈理, 李瑜, 张仙 (707)
- 2 地球科学“西学东渐”肇始——国家宝藏之《坤舆万国全图》·····骆遥, 李敬敏 (714)
- 3 “天眼”望矿山: 十年磨一剑·····姚维岭, 杨金中, 王晓红 (720)
- 4 中国矿山开发环境遥感监测漫谈·····姚维岭, 许文佳, 杨金中 (724)
- 5 浅谈航空电磁探测技术在资源环境调查中的应用·····何怡原, 梁盛军, 余学中 (731)
- 6 GRACE 卫星: 通过重力场变化认识地球·····张婉 (732)
- 7 地球重力在地球科学中的应用·····李筱, 张婉 (734)
- 8 探究人工智能在计算机网络技术中的应用·····张智轩 (736)
- 9 计算机网络安全问题及其防范措施·····张智轩 (737)

DOI: 10.13745/j. esf. yx. 2017-6-10

精细地质初议

刘 刚, 梁树能, 燕云鹏, 闫柏琨, 王 喆

中国国土资源航空物探遥感中心, 北京 100083

LIU Gang, LIANG Shuneng, YAN Yunpeng, YAN Bokun, WANG Zhe

China Aero Geophysical Survey and Remote Sensing Center for Land and Resources, Beijing 100083, China

LIU Gang, LIANG Shuneng, YAN Yunpeng, et al. Overview of fine geology. *Earth Science Frontiers*, 2018, 25(2): 267-279

Abstract: The necessity of fine geology study is put forward in this paper through requirements analysis of economic development, resource exploration, environmental protection and development of geosciences. The concept and technical system of fine geology are illustrated. Fine geology involves precise and detailed study of geological phenomena based on advanced technology and high sensitivity of the measuring instrument; results obtained from such study can be used for the advancement of scientific research, exploration and economic construction. The technical system of fine geology include remote sensing, geophysical prospecting, geochemical exploration, drilling, isotopic dating, space positioning techniques and computer technology, etc, and an integrated full range air-surface-subsurface 3-dimensional survey usually completes the fine geology study. Taking remote sensing as an example, the feasibility of fine geology is described through analyses of the development and application of geophysics, remote sensing, isotope and geochemistry in fine geology studies at home and abroad. The prospects of applying fine geology in mineral resource exploration, geological research, environmental protection, national defense and geological disaster investigation are discussed in this paper.

Key words: fine geology; concept; technology system; present situation; possibility; application prospect

摘要:通过对经济建设、资源勘探、环境保护和地学发展的需求分析,提出了进行精细地质研究的必要性,诠释了精细地质的概念及其技术体系。认为精细地质是以先进的技术方法和高灵敏度的测量仪器,对地质体进行精确细致的研究,形成先进、精确、实用的成果,达到提高地学科研与调查水平,高效服务经济建设的目的。精细地质的技术体系包括遥感、物探、化探、钻探、同位素测年、空间定位技术、计算机技术等,通过空中-地表-地下全方位立体化的综合调查,完成对研究对象的精细研究。通过物探、遥感、同位素测年、化探等核心技术在国内外精细地质研究中的发展应用状况分析,以遥感技术为例,阐述了进行精细地质调查研究的可能性,展望了精细地质在矿产资源勘探、地学研究、环境保护、国防建设、地质灾害调查等领域的应用前景。

关键词:精细地质;概念;技术体系;现状;可能性;应用前景

中图分类号:P62 **文献标志码:**A **文章编号:**1005-2321(2018)02-0267-13

0 引言

近十几年来,我国国民经济处于高速发展阶段, 高速铁路、公路、跨海桥梁、大型水电站等公共设施

建设规模庞大,城市规模不断扩展,京津冀、长三角、珠三角等沿海地区涌现出一系列城市群。经济建设

收稿日期:2016-11-02;修回日期:2017-03-24

基金项目:中国地质调查局“西北边境明铁盖地区基础地质遥感解译”(DD2016007602)

作者简介:刘 刚(1963—),男,高级工程师,主要从事遥感地质研究。E-mail:lgang666@126.com

庞大的公共设施建设需要精确的大比例尺地质测绘资料及可供消耗的矿产资源作为支撑;另一方面,国民经济的高速发展及落后的工艺水平对资源的过度消耗,造成的环境压力越来越大,土壤、空气和水污染、地面沉降、滑坡泥石流等灾害事件频发,建设宜居的和谐社会,需要对我们赖以生存的环境现状及其发展趋势进行调查监测,危害较大的地质灾害需要进行精细的定量调查和分析。

目前,公共设施建设所需的大比例尺地质资料非常匮乏。我国陆域现有基础地质资料,大部分属于20世纪和21世纪初编制的1:20万和1:25万区域地质调查资料,由于精度不高只能作为背景参考。经济建设的具体实施需要1:5万及更大比例尺的工程地质、水文地质和环境地质等专业性很强的地质资料。目前1:5万区域地质调查资料不但数量少,而且主要分布在山区,而京津冀、长三角、珠三角等东部经济发达地区,大部分位于第四系分布区。更大比例尺的区调资料及矿产勘查、工程地质、水文地质等专业地质资料不属于公益性数据,更为稀缺。所以现有资料的精度、种类明显不能满足经济建设需求。

现有矿产资源难以保障经济持续良性发展。十几年来,国民经济的高速发展导致我国矿产资源消费长期保持两位数增长,由于20世纪末期我国矿产调查投入过度萎缩及勘查技术的落后,导致我国大宗矿产品对外依存度居高不下。虽然近几年由于经济低迷的影响,矿产品的需求有所下降,但从国家经济安全角度出发,大宗矿产品对外依存度必须保持在安全临界线以内。同时,经济持续良性发展需要有一定规模的资源保障,因此找矿仍然是一项重要任务。但是,随着矿产勘查的深入露头矿已经发现殆尽,勘查的难度越来越大,成本越来越高。目前勘查的主要方向已转向隐伏矿床和深部矿床的勘探,必须探索在复杂地质条件下的新一代勘探技术,以促进矿产勘查的新突破^[1]。

常规技术手段难以应对日趋严峻的环境问题。危害较大的地下水超采引起的地面沉降遍布华北,大部分沉降区的面积都超过十几万平方千米,但每年的沉降速率却在毫米量级;滑坡、泥石流及其导致的堰塞湖需要灾后立即对其进行规模及危害程度进行精细的定量调查和监测,而且前提是必须得到已经被破坏的灾前地形地貌的高精度数据;洪水灾害威胁需要以小时为周期进行不间断准确评估及监

测。类似以上区域性环境与灾害问题,传统的调查监测手段受技术水平、费用、可操作性等因素的限制,已经难以满足现代社会的需求,需要采用新技术加以解决。

近几十年来,地质学在理论研究和技术方法方面有很大的发展,但我国却鲜有创新性研究成果。董树文和李廷栋^[2]认为,近30年的地质科学理论的提出,绝大多数依赖于对地球深部认识的突破。王晋年等^[3]指出地球深部信息的缺失,是导致我国地质科学理论创新、资源勘查和地质灾害预警能力全面落后的重要原因。笔者认为,深部信息的缺失只是问题的表象或一个方面,精细的多学科综合调查与研究体系的缺位,是我国科研与调查工作落后的根本原因。无论是经济发展赖以生存的基础地质调查、矿产勘查,还是环境保护和地学研究,都需要充分利用新的技术手段对工作对象进行深入细致的综合性调查研究。

20世纪末以来,航天遥感、航空物探、全球定位系统、计算机、网络等信息技术有了长足的进步,为以隐伏矿床为代表的深部信息的探测、分析,以及地表环境的变化、监测等提供了新的技术手段,使深入细致的地质调查和地学研究成为可能。我们应该摒弃粗放型的工作思路,充分利用现代科学技术手段,对地质现象进行空中-地表-地下三维立体精细研究,通过科技创新为科研、经济建设、矿产勘查、环境保护等提供先进的技术方法和具体实用的成果,推动地球科学的发展进步。这种集多种科学技术于一身,对地质和环境进行深入细致研究的工作,应该是一个新的地学边缘学科——“精细地质学”(Precision Geology)。

1 精细地质学概念

“精细地质学”,在某种程度上类似于“精细农业”(Precision Farming)。精细农业是20世纪80年代由美国、加拿大的一些学者和农业科研部门提出的^[3-4]。精细农业将遥感技术、地理信息系统、全球卫星定位系统、计算机技术、自动化技术、网络技术等高科技应用于农业生产,根据时空变异,定位、定时、定量地实施一整套现代化操作与管理,实现精细化、信息化的现代控制农业。其中,4S技术是精细农业的技术支撑:GPS(全球定位系统)的作用是田间信息采集过程的精确定位、耕种作业机械自动

导航等;RS(遥感技术)是运用高分辨率传感器对作物长势及其背景进行实时监测;GIS(地理信息系统)是精细农业的大脑,它对网络等传输技术接收的GPS、RS传感器的大量实时信息进行分析、统计,为差异性决策及实施调控提供决策处方信息;DSS(决策支持系统)利用GPS、RS获得的各种信息及GIS建立的数据库,根据前期建立的分析模型对农作物生长环境和生长条件在时间和空间上存在的差异做出分布式变量投入^[4],从而达到精细种植的目的。

精细农业抛弃传统农业粗放式大面积平均投入的耕作方法,通过科技创新实现产业更新换代的思路,应该是21世纪地质工作方式方法创新转型的范本。20世纪是工业社会(尤其是中国等发展中国家),地质工作主要目的是解决工业化过程的资源供给问题,获取地质信息的手段在很大程度上还依靠肉眼观察(虽然遥感、物探等技术已经使用,但实施范围有限,精度不高)。21世纪是信息社会,需要解决资源有效供给和环境保护等社会可持续发展问题,获取地质信息的手段将逐步转向遥感、物探、化探等信息技术,通过综合运用高效、高精度的现代高新技术进行“深耕细作”,依靠技术进步来满足社会需求,解决发展与环境的矛盾问题。

到目前为止,精细地质还没有一个非常明确的概念。“精细地质”一词出现频率最多的是石油地质行业^[5-11],常见的描述有“精细地质”^[5]、“精细地质分析”、“精细地质建模”^[6]、“精细地质研究”^[7]等等。20世纪80年代以来,世界一些主要产油国的油气田相继进入高成熟开发阶段,由于勘探成本的大幅度上升,提高油气采收率便成为老油田获取最大经济效益的一条有效途径,因而要求储层地质研究向更精细、量化方向发展。于是便产生了石油行业所谓的“精细地质”:主要是建立在密集井网测井资料及现代沉积学发展基础之上的,即对石油储层的沉积相进行精细研究,详细划分开发单元,建立相应的精细化储层地质模型,协助进行油田的科学高效开发。在石油地质行业,精细地质的研究对象大部分是石油储层,相关数据的采集、定位依靠密集的井网测井资料和高精度三维地震资料等,数据解释借助于先进的计算机软硬件;精细化储层地质模型的建立,来源于层序地层学^[12]等相对较新的地质理论;研究成果则用于油田的科学高效开发。整个工作过程与“精细农业”有相似之处,属于精细地质的范畴,但不应是精细地质的全部内涵。

从地质大行业角度来看,精细地质的研究领域不应局限于石油行业,更不能仅局限于对石油储层的研究,应该包括区域地质、矿产地质、工程地质、水文地质、环境地质等诸多地质行业,研究对象小到矿物、岩石、矿床、矿田、工程基址、港口、城镇,大到造山带、成矿带、经济带以至全球。精细地质涉及的技术手段也不仅是测井、高精度三维地震等个别地球物理技术,应该包括遥感、物探、化探、放射性、探矿工程自动编录、计算机等多种技术方法。即精细地质研究者所使用的工作方法和测量仪器应该代表当时的先进水平,通过使用高灵敏度的仪器和先进的技术方法,使研究工作在数据采集、时空定位及处理分析等关键环节相对精准,从而得到客观可靠的研究成果。所以“精细地质”应该是:以先进的技术方法和高灵敏度的测量仪器,对地质体(现象)进行非常细致的研究,形成精确、实用的成果,达到提高地学科研与调查水平,高效服务经济建设的目的,使科学技术迅速转化为生产力。

2 精细地质技术体系

2.1 数据采集技术

21世纪已经进入信息社会,信息技术自人类社会形成以来就存在,并随着科学技术的进步而不断变化,以现代电子信息技术为代表的第四次工业革命使人类利用信息的手段发生了质的飞跃,机器被用于收集、处理、控制、存储信息,扩大了人类的思维和感官功能。21世纪的地质工作将与20世纪有很大的区别,信息技术会逐步成为地质工作的支柱,不同探测技术所获取的大量信息的综合运用,将是地学研究及调查工作突破的关键。因此,遥感、物探、化探等延伸了人类感官的信息探测技术,应该是精细地质的主要组成部分。

地质学起源于地面观察,但由于视域和识别能力的限制,仅仅依靠肉眼难以全面深入了解复杂的地质问题,因此,遥感、物探和化探技术被引入到地质研究之中,这三种技术有一个共同点,那就是具有远程探测人体感官无法识别的信息的能力。遥感技术具有宏观性、综合性特点,主要通过对地物光谱、形态、地貌等信息的探测,获取地表地质信息,其短波红外和热红外谱段可探测肉眼无法识别的地物波谱信息,极大地拓宽了人类的视野和探索能力,已成为地质研究和地质勘查不可缺少的技术手段,在地

质调查、矿产勘查、地质环境评价、地质灾害监测和基础地质研究等方面都发挥了越来越大的作用^[13]。地质学最原始的地下探测技术是坑探和槽探,后来发展到钻探,现在物探尤其是航空物探,已经是快速、高效、全面探测地球深部信息的主要技术,在地质研究和矿产勘查工作中具有重要的作用。化探是系统研究地球化学勘查的理论、方法和技术的一门科学,由于矿产资源的形成和环境问题的产生均与化学元素及其化合物的分布有关,因此,系统测量元素空间分布和变化的特性,使之既可用于地表调查,也可用于深部研究。数字化岩心扫描及解译系统,是近期伴随高光谱(Hyper-spectral,又称成像光谱,指光谱分辨率很高,可获取地物连续且完整的光谱曲线的遥感技术^[13-14])发展起来的新型地下探测技术,该系统可以快速、相对准确地获取钻孔、探槽中岩石的高光谱数据,以廉价成本得到大量地下岩石的矿物组成、成分及空间分布信息^[13],显然也可以应用于各种探矿工程的编录和信息采集。

2.2 数据处理及时空定位技术

地质作用的时空演化过程、机制及演化结果,是地质研究的普遍问题,地质工作过程通常包括数据(样品)采集、时空定位和对数据(样品)的处理、分析,最后得出结论。数据采集阶段涉及遥感、物探、化探和探矿工程编录等信息采集技术,处理过程一般由计算机完成,所以计算机技术已经成为现代地学研究不可或缺的工具。由于硬件性能指标的迅速提高,计算机的数据存储能力、计算速度已经非常强大,为高精度的遥感、物探和化探海量数据处理提供了保障。神经网络、模糊数学、专家系统等技术和理论的引入,大大提高了计算机模拟能力,为各种数学模型的建立提供了有力的支持。此外,数据采集和分析离不开对时间和空间的精确定位。地质事件发生时间的确定,一般靠同位素测年来实现,测年精度的高低决定了地质事件年龄的准确程度。地质研究的空间问题,包括观察对象的空间准确定位和观察平台的动态定位,也包括显微、微观观察及其精准定位。目前主流的宏观空间定位系统以GPS为主,随着北斗系统的逐步完善,国产空间定位系统有可能成为精细地质研究的备选技术。

2.3 技术融合

由于地质作用的特殊性和复杂性,依靠单一的

技术方法进行精细研究难度很大,遥感、物探、化探、计算机、全球定位系统等多种前缘技术的综合利用,是实施精细研究、实现科技创新的关键。澳大利亚为解决资源需求,在1998年提出了“玻璃地球计划”^[15],目的是通过三维可视化和地质模拟等技术,使大陆表层一公里“像玻璃一样透明”,填制一个信息丰富的四维澳大利亚“地图”。其模式为:借助新的航空物探技术、航空和航天遥感技术、先进的地球化学勘探技术及高级钻探技术获取地面和地下的成矿信息,利用地理信息系统、模拟技术、三维可视化、数据融合和转化技术等,综合处理各种成矿和找矿信息。通过网络技术实现信息共享,从而使大陆表层一千米“像玻璃一样透明”^[15]。为满足我国对矿产资源的巨大需求,探索新一代矿产勘查技术,王晋年等^[1]在2012年提出了“光谱地壳计划”,旨在针对地表和地壳表层,实现高光谱技术对地球表面的地质填图和矿物蚀变信息的遥感探测,以及对钻探岩心的光谱探测,建立地壳高光谱数据库集,满足以高光谱探测技术对地壳表层一定范围内矿物的识别和探矿需求。该计划拟通过天基、空基、地基、地下岩心遥感探测构成的一体化,建立遥感立体探测体系,结合物探、化探、钻探技术,解决遥感直接找矿和深部找矿的难题,带动我国整体勘查技术水平的提高和发展。“玻璃地球计划”涉及航空物探、遥感、地球化学、钻探、地理信息系统、模拟和三维可视化、数据融合及转化等,突破了传统运用单一手段进行地表浅部资源勘探的局限,强调综合运用新技术、新方法进行矿产资源全方位的识别探测,实现矿产勘查能力的革命性进步。“光谱地壳计划”以高光谱遥感为核心,综合利用物探、化探等数据,建立以遥感技术为主的立体探测体系,其数据处理及解释过程,同样涉及地理信息系统、模拟技术、三维可视化、数据融合等辅助技术。“玻璃地球计划”和“光谱地壳计划”的核心要素均是航空物探、遥感、地球化学等信息探测技术,属于精细地质的研究体系。两个计划以矿产勘查为目的,强调多种技术的综合运用和对地球的立体研究,体现了精细地质的理念和工作方式,代表了现代地质工作的方向。

由于我们的研究对象是具有长期复杂演化过程的庞大综合体,无论是基础地质研究、矿产勘查开发还是地质环境的调查监测,多技术的交叉融合已经是大的趋势,无论是理论创新、技术创新还是应用模式创新,都离不开多种先进技术手段的综合运用和

精细分析。所以,精细地质的主要技术体系包括:遥感、物探、化探、同位素测年、计算机、全球定位系统、网络等,当然也包括肉眼观察和各种勘查工程的信息采集。通过空中-地表-地下全方位立体化的综合调查,实现研究对象的精细分析。在这个技术体系中,遥感图像是多种技术实现融合、进行工作、显示成果的理想平台,所以遥感技术处于核心地位。大部分地学研究,其工作部署、具体实施和最终成果的演示都需要一个空间平台,20世纪最通用的平台是地形图,虽然现在地形图实现了数字化,但地表的植被、坡度、坡向、冲沟、水系、雪被、建筑物等自然和人文景观难以得到直观的体现,需要人脑根据图面符号和读图规则,通过逻辑推理或数学计算间接获得相关信息。而且,植被、积雪、水体、交通、建筑、地质灾害等具有动态变化的要素,地形图不能提供准确的信息。遥感图像不但含有丰富的上述地表景观信息,而且仅根据目视解译就能掌握大部分信息,还可以根据需求对动态要素进行实时更新,其直观性、适用性是地形图所无法比拟的;遥感图像含有精确的地形空间信息,其精度已经达到亚米级,能够满足大部分地学研究的要求;具有数字化空间属性特点的遥感技术(RS),已经与地理信息系统(GIS)、全球定位系统(GPS)实现3S技术的无缝衔接,在三维立体研究与显示方面具有很大的优势;遥感影像含有丰富的矿物、岩石、构造、地貌等地学信息,可以与物探、化探、钻探等技术实现理想的融合。因此,集精确的空间地形信息、多样的地表景观信息和丰富的地学信息于一体的遥感技术,是多种地学方法技术融合、工作、显示的理想平台,是精细地质技术体系的核心要素。

3 国内外研究现状

3.1 国外研究现状

在西方发达国家,精细地质调查工作已经有几十年的历史,从20世纪末期用于石油勘探开发的高分辨率层序地层学^[16]、高精度三维地震开始,已经产生了直接的经济效益,现在高分辨率遥感和高精度航空物探也成为精细地质调查研究的主要技术手段。澳大利亚、加拿大和美国等国家开发出了直接为找矿和环境监测服务的高分辨率、超高分辨率航空物探技术,“包括高灵敏度测量仪器组成的航空物探测量系统、大比例尺高精度航空勘查技术、精细的

数据处理和解释方法等。其利用直升机、无人机、飞艇等运载工具,可以实现最低10 m的超低空飞行”(常规调查的固定翼飞机飞行高度通常在200 m以上),“采用高灵敏度磁力仪、电磁仪和伽马能谱仪器组成的测量系统,采样间距一般为几米(常规调查的采样间距十几米~几十米),采用差分GPS精确定位,定位精度可达米级甚至亚米级。由于仪器灵敏度及采样空间分辨率的提高,采集的信息丰富,解释技术的改进,使地质找矿能力大大提高,甚至可根据异常定量解释的结果直接布钻,从而降低成本、缩短找矿周期”^[17]。

高分辨率遥感在国外已经逐步用于不同目的精细地质调查:高空间分辨率的民用卫星图像(GeoEye-1卫星在美国本土地面分辨率达到0.4 m,WorldView-3分辨率达到0.31 m),可实现1:1 500的大比例尺快速地质测绘填图和灾害调查;重访周期几小时到1天的高时间分辨率遥感卫星(Worldview-2重访周期2次/天,编队飞行的卫星星座重访周期甚至可缩短至数小时)已经在环境地质、灾害地质调查与监测领域发挥重要作用,使单纯的变化监测逐渐发展为对地物或现象演化过程的细致研究^[13];高光谱分辨率遥感(简称高光谱,下同)用于直接识别地物类型^[18]、组成和成分^[19-20],反演地物的物理、化学参数,建立以遥感为主要信息源的找矿预测与环境评价定量模型,通过利用天空、地面、地下的光谱数据识别矿物的三维空间分布及组合特征,研究地质体的空间分布、相互关系以及地质流体的运移通道^[13]。利用高光谱数据直接提取矿物信息,对地质体进行精细研究的方法,已经应用于基础地质研究、地质勘查、行星探测、地质环境监测和矿山采选等领域^[13,20-23]。

为进行地质矿产资源的深部探测和三维立体探测,澳大利亚联邦科工组织(CSIRO)研制出了数字化岩心扫描及解译系统 Hylogging System^[24]。该系统能够沿岩心方向连续获取矿物反射光谱及高分辨率彩色影像,分析和识别多种地质单元和热液蚀变聚合物,为地质矿产资源的深部探测和三维立体探测提供了一种非常便利的技术手段。利用地面成像光谱仪获取地表岩石矿物的精确高光谱信息、岩心光谱扫描系统获取地下岩石矿物的高光谱数据,以开展矿物的地表和地下的全方位立体填图,成为了目前世界各国研究的热点^[1]。

时间与空间是地学研究的两个重要约束条件,

同位素用于岩石年龄的测定已经有比较长的历史,但20世纪后期随着封闭温度理论的提出与发展^[25-27]、测年实验流程的改进、模拟技术的提高,至20世纪末,集同位素年代学、构造地质学、岩石矿物学、计算机模拟技术为一体的构造-热年代学开始崛起,其测试结果含有测定对象的形成时间、形成温度(深度)等信息,可对不同尺度构造的变形时间、山体抬升和盆地沉降速率等提供精细的年代与热作用信息^[28]。构造-热年代学是对大陆造山带形成过程时空演化序列精细测定的一次革命,为大陆动力学研究提供了新的技术手段。

3.2 国内研究现状

我国在20世纪已经开始了精细地质的生产和研究工作,最原始的精细地质应该是应用于矿产勘探开发和工程地质勘查工作,如在矿区和大型工程场址开展的大比例尺($\geq 1:25\,000$)详细地质填图、利用密集钻孔和坑道进行针对隐伏(深部)金属矿床勘查的大比例尺井中物探、针对桥隧工程进行的高精度物探等^[29]。

20世纪90年代在石油系统发展起来的含油储层精细研究,是我国前期规模化精细地质研究的典型代表:以高精度三维地震和密集井网测井资料,对储层的沉积相进行精细研究,建立高精度的储层地层格架及三维建造,更好地确定和预测储集层及遮挡层的空间展布,实现对油田的科学高效开发。其中,计算机技术在资料处理解释、精细化地质模型的建立等过程中起到了重要作用。

高精度三维地震在20世纪末期开始用于煤炭勘查开发工作^[30-32],为煤矿采区的开发决策、巷道布置与开拓提供了可靠依据。尤其在勘探小断层、褶曲、陷落柱、老窑、采空区等方面显示了传统二维勘探无法比拟的优势,在预测采区煤层厚度,顶底板岩性等方面都展示了潜在的能力。

高精度同位素测年在环境地质、构造地质等方面也有精细研究的成功案例^[33-40]。李建芬和王宏^[33-34]通过²¹⁰Pb和¹³⁷Cs短半衰期同位素示踪,对现代海岸带泥质沉积物进行精细测年,初步查明了渤海湾西岸近150年以来海岸带现代沉积速率。进而结合地表高程、下沉速率和海面上升速率,预测了以2050年为时限的渤海湾西岸海平面相对变化趋势。周爱锋等^[35]通过对六盘山天池湖泊沉积物进行孢粉、磁化率、沉积物色度指标分析,结合陆源植物残体的高精度AMS测年控制,获得了中晚全新

世6 200 a来的高分辨率气候变化记录。我国的地质年代学家利用20世纪末发展起来的构造-热年代学方法技术,在中新世代构造隆升、剥蚀和构造变形的精确定年,以及精细复原造山带内部同构造块体增生拼贴的时空过程等方面,也取得了重要的成果^[36-41]。

近十几年,我国地球化学工作者通过原生晕测量方法创新、在土壤覆盖层中以微米筛分仪为主的土壤粒级精加工技术研发、元素迁移机理研究、浅钻化探立体填图等,以及在深穿透地球化学调查方法技术与异常形成机理研究等方面都有重要进展,取得了显著的找矿效果,为隐伏矿床的勘探提供了有力的技术支持^[42-43],使中国化探技术总体上继续保持国际先进水平^[42]。

高分辨率遥感是精确获取地表地质与环境信息的关键技术之一。21世纪以来,高分辨率遥感在国内基础地质调查、矿产勘查、环境监测、工程地质调查、水文地质调查、灾害地质调查和地貌调查等方面,开始了规模化应用^[46-61],遥感技术已经进入亚米级高分辨率时代。目前应用领域包括利用高空间分辨率数据进行大比例尺地质填图、湿地和矿产开发环境的监测与评价^[46,51,56]、利用高光谱和多光谱数据进行以矿产勘查为目的蚀变信息精细提取^[47-49]、利用干涉雷达(InSAR)进行冰川和地面沉降等区域性地表缓变形(监测周期内变形量在几毫米~十几毫米)的精确测量与监测^[52-53]、利用高光谱数据进行矿山环境调查^[50,56]、利用高空间分辨率影像对滑坡和塌陷等地质灾害进行定量精细调查研究^[58-60]、利用高精度机载LiDAR数据生成的大比例尺DEM(数字高程模型)进行高精度地貌填图^[61]等。

高分辨率物探技术,是获取深部地质信息的主要手段。近几年来,高分辨率航空物探测量与精细解释技术得到迅速发展,已经在危机矿山深部找矿与地下煤火探测等领域发挥了重要作用^[62]。目前“国内直升机航空物探测量系统的最大勘探比例尺已达1:5 000,探头离地高度最低可达30~80 m,采样间隔可达1~3 m左右,DGPS(差分GPS)平面定位精度好于1 m,是地形复杂地区精细矿产勘查工作最新的技术手段。同地面物探相比,直升机测量具有速度快、测量精度高、信息丰富、异常分辨率高等优点”^[62]。2000年以来,我国自主研制的航空氡光泵磁力仪探测精度达到0.001 nT,比以前提高了两个数量级,实现了对地表弱信息的空中探测,技

术达到世界领先水平。结合地质和钻孔资料进行航磁剖面的三维精细反演及显示,大大提高了解释精度。另外,地面物探技术也向重磁电的综合运用及高分辨率精细解释方向发展^[63-64]。

由于计算机软硬件技术的迅速发展,虚拟现实、三维可视化技术已经普遍用于地质模型的建立、航空物探和遥感数据的解释之中,大大提高了解释精度和准确性。

4 实现的可能性

进入21世纪以来,信息科学与技术的发展进入快车道,与精细地质有关的遥感技术、物探技术、化探技术、空间定位技术、计算机及网络技术等进入高精度、高速度、智能化阶段,完全可以支撑精细地质的实施。

以遥感技术为例,从20世纪末至今,用于地质研究的光学传感器,空间分辨率从30 m提高到0.31 m,光谱分辨率从40~200 nm提高至2.3~15 nm(表1),干涉雷达技术已经可以监测到毫米级别的地表沉降。在几十年的时间内,遥感地质完成了从小比例尺定性研究到大比例尺精细定量研究的飞跃。20世纪80年代,地质调查所用的遥感数据以空间分辨率30 m的美国陆地卫星(Landsat 5)TM多光谱数据为主,20世纪90年代以改进型的ETM+(Landsat 7,全色波段分辨率提高到15 m)多光谱数据为主,由于数据的空间分辨率不高,基本上以中小比例尺($\leq 1:100\,000$)的区域性地质调查和矿产调查为主,工程地质、灾害地质、环境地质等精度要求较高的工作,很少使用航天遥感数据。20世纪90年代,空间分辨率10 m(全色波段,后来提高到5 m)的法国SPOT卫星数据开始进入地质调查领域,但由于其高昂的价格和谱段设置方面的缺陷(谱段范围可见光—近红外,岩性识别受限),难以在地学领域大规模使用。这一时期,地学领域使用较高分辨率(优于5 m)的遥感影像是航空相片,但由于受成本、气候、空域管制等诸多因素的限制,仅能在局部地区、局部领域进行小规模的探索性工作。21世纪初期开始,优于2.5 m的高空间分辨率航天传感器大量出现,QuickBird、WorldView、IKONOS、SPOT-5是典型代表,由于差分GPS技术和高性能计算机的普及,解决了长期困扰高空间分辨率遥感影像的定位、纠正和数据处理问题,推动了高空间分辨率遥感的

使用。2013年以来,空间分辨率分别为2 m、1 m和2.1 m的高分1号(GF-1)、高分2号(GF-2)、资源3号(ZY-3)等系列高分辨率国产卫星的升空,使数据的成本直线下降,推动了高分数据在地学领域的使用。这一时期,传感器不但在空间分辨率上得到了大幅度的提升,在光谱分辨率上也有了革命性进展,高光谱遥感在地学领域的应用也逐渐发展起来。高光谱(Hyperspectral)遥感是遥感技术的前缘领域,其利用地面或天空平台上的成像光谱仪,在电磁波谱的紫外~热红外波段范围内,以上百个非常窄的光谱波段对目标同时成像(表1,CASI-1500、SASI-600),获取目标的空间、辐射和光谱三重信息。高光谱遥感可以根据精细的光谱特征识别多光谱遥感无法识别的地物,如矿物类型^[18](图1)、矿物化学成分(图2)及其含量的变化^[19-20,47]等。多光谱遥感的研究对象是岩石,而高光谱的研究对象已经精确到矿物,前者以定性研究为主,后者为定量半定量研究。目前,高光谱遥感理论上可识别褐铁矿、赤铁矿、针铁矿、绿泥石/绿帘石、透闪石/滑石、角闪石/阳起石、绢(白)云母/伊利石/蒙脱石、高岭石、蛇纹石、地开石、叶蜡石/明矾石、辉石、橄榄石、符山石、电气石、黄玉、黑云母、金云母、方解石、白云石、菱铁矿、菱镁矿、孔雀石、石膏、黄钾铁矾、石英等30~40种矿物的种类成分以及含量信息^[13]。高光谱遥感在信息提取的种类、可靠性、定量化程度等方面均有显著提高,可以进行区域性大视角的岩石学(图3(a),图4)、矿床学(图2(a),图3(b))和构造地质学的定量半定量研究,为地学研究的精细化、定量化提供了新的平台和基础数据,有可能带来地学研究的革命。

雷达干涉技术(InSAR)是与高光谱同时发展起来的另一项可对地表进行精细定量探测的前缘遥感技术。它利用雷达卫星对同一个区域在不同时相、不同位置探测雷达波的相位差,反演地表三维空间位置及其微小变化。理论上,差分InSAR技术能够探测毫米级地表形变,实际应用中,在气候与地理环境状况适合的地区,测量误差可低于5 mm^[13],由于该技术具有高精度、高效率,可进行大区域面状探测的特点,目前被广泛应用于地面沉降、矿区沉陷、滑坡、构造活动、火山活动、冰川活动及地震形变等地表形变的调查和监测^[13]。近期,中国地质调查局利用InSAR技术,对全国三大严重地面沉降区开展了连续的地面沉降调查和监测工作,仅用5年的时间,

就获取了华北、长三角和汾渭盆地几十万平方千米的地面沉降精确数据,为中国中东部人口密集、工业发达地区的经济建设、减灾防灾、环境保护战略决策的制定和实际工作的实施提供了可靠依据,体现了精细地质在经济建设和环境保护中的高效率和实用

性。图5为某地矿山开采引起的地表沉降航天雷达干涉图像,在70天的监测周期内,南北向分布的沉降区最大沉降幅度为84 mm。目前,InSAR已经与水准测量、GPS一起成为地表形变测量的支柱技术。

表1 用于地学研究的代表性光学传感器参数

Table 1 Parameters of representative optics sensors for geological research

类型	名称	谱段范围	最高光谱分辨率/nm	最高空间分辨率/m	波段个数	特点
低分辨率	ETM+	VNIR	60	15	5	主要用于1:100 000等中小比例尺的区域
		SWIR	200	30	2	性宏观地学研究
	ASTER	VNIR	60	15	3	主要用于1:100 000等中小比例尺的区域
		SWIR	40	30	6	性宏观地学研究
高空间分辨率	GF-2	VNIR	60	1	5	弥补了普通多光谱图像在空间分辨率方面的缺陷,可进行细致的地学研究;成图比例尺可达1:5 000,价格低廉
	ZY-3	VNIR	60	2.1	5	弥补了普通多光谱图像在空间分辨率方面的缺陷,可进行比较细致的地学研究;成图比例尺可达1:10 000,价格低廉
	QuickBird	VNIR	60	0.61	5	弥补了普通多光谱图像在空间分辨率方面的缺陷,高清影像可进行精细的地学研究;成图比例尺可达1:3 000
	WorldView-3	VNIR	8	0.31	16	突破了高空间分辨率卫星在岩性识别等方面局限性;阴霾穿透能力使图像更加清晰,可进行精细的地学研究;超高分辨率使成图比例尺达到惊人的1:1 500
高光谱分辨率		SWIR	30	1.24	12	
HyMap	VNIR	15		64	数百个纳米级高光谱分辨率的波段连续成像,实现了由岩石识别到矿物识别、由定性研究到定量分析的飞跃;对矿物含量及空间分布的精细分析有可能带来地学研究在技术方法上的革命性变化	
	SWIR	13		64		
CASI-1500	VNIR	2.3		288		
SASI-600	SWIR	15		100		

注:VNIR为可见光—近红外谱段;SWIR为短波红外谱段。

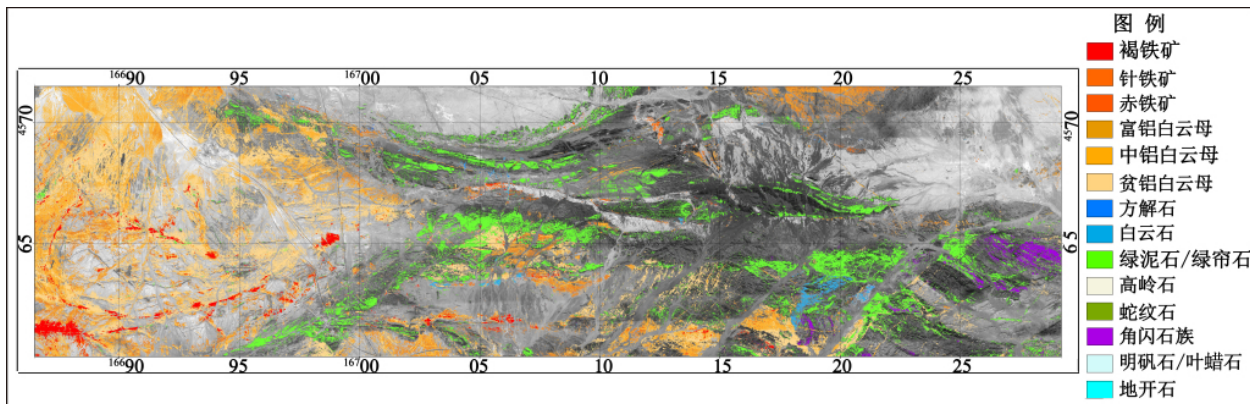
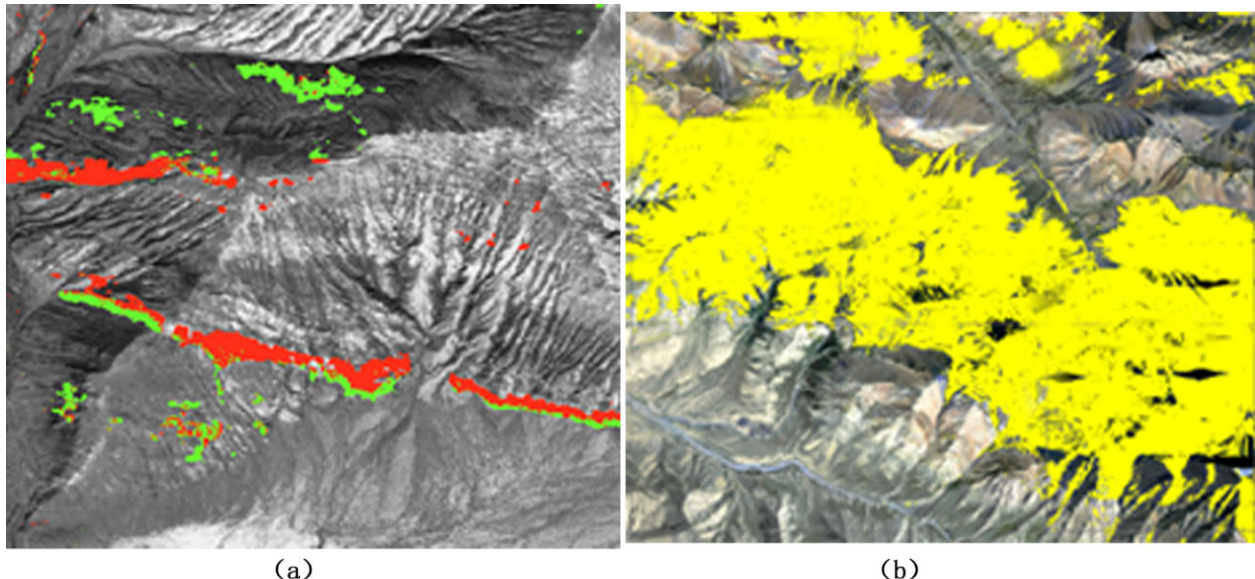


图1 甘肃省柳园地区航空CASI/SASI高光谱遥感矿物分布图

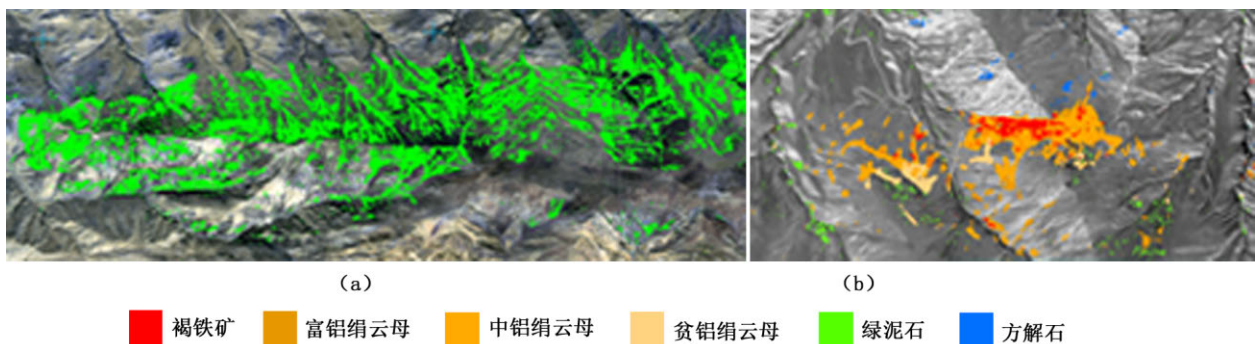
Fig. 1 Minerals distribution from CASI/SASI hyperspectral data of Liuyuan area in Gansu Province



(a) —与热液蚀变有关的富铝白云母(红色)和中铝白云母(绿色);(b) —与成岩有关的低铝白云母(黄色)。

图 2 航空 CASI/SASI 高光谱数据检测出的不同成分白云母

Fig. 2 Muscovites detected from CASI/SASI hyperspectral data



(a) — 区域变质作用形成的绿泥石; (b) — 金矿及周边呈带状分布的热液型蚀变矿物组合。

图 3 航空 CASI/SASI 高光谱数据检测出的区域变质矿物及热液蚀变矿物

Fig. 3 Regional metamorphic and hydrothermal minerals detected from CASI/SASI hyperspectral data

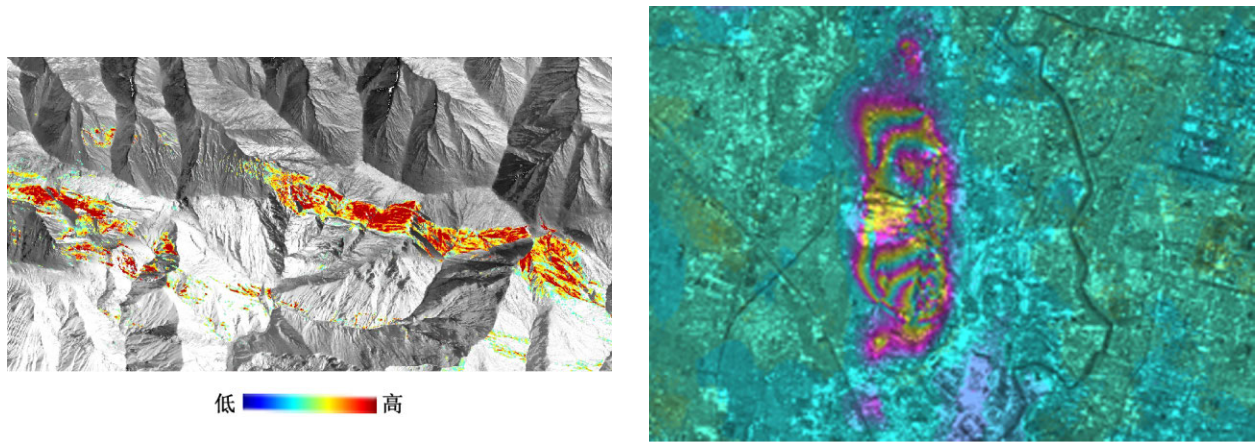


图 4 航空 CASI/SASI 高光谱数据检测出的方解石丰度图

Fig. 4 Content of calcite detected from CASI/SASI hyperspectral data

图 5 矿山开采引起的地面沉降雷达干涉图像
Fig. 5 InSAR image of land subsidence caused by mining

以上论述说明:高分辨率遥感可以使地质学家从宏观的视野(地质体尺度(km)),以微观的机理^[65-66](矿物尺度(mm)),对历史悠久(百万年尺度(ma))、错综复杂的地球进行精细化研究。其工作方法从辐射范围有限的离散式点状野外肉眼观察,升级为区域性面状连续的影像数据计算机自动识别,从传统的定性描述转为定量研究,如果再结合物化探和各种勘探工程采集的数据,就可以实现全面的立体精细化研究。所以,依据高光谱分辨率和高空间分辨率遥感、高性能计算机、高精度空间定位系统等高精尖前缘技术,可以实现精细的定量半定量地质调查与研究。

和遥感技术一样,作为精细地质体系的主要技术,物探、化探等在数据采集的精度、解释方法^[62]、机理研究^[42]等方面也有了突破性进展,给精细地质研究工作提供了有力支持。计算机技术的迅猛发展,解决了高精度数据采集过程形成的海量数据的处理问题,高精度空间定位技术解决了畸变纠正和数据采集的精确定位问题,高速网络技术解决了数据的传输问题,地理信息系统和虚拟现实技术助力可靠模型的建立与地质现象的三维精细立体分析,所以精细地质在技术层面是可以实现的。该学科在研究平台、研究方向和技术方法上代表了地学领域的发展趋势,必将带来革命性的变化。

5 实例

我国存在一批可采资源储量近于枯竭的老矿山,急需在矿区深部或周边地区发现新的接续矿体,避免矿山关闭的风险。由于这些老矿区前期已进行了大量的勘探工作,地质工作程度高,要发现新的矿体必须使用更加先进的理论和技术方法,进行精细的地质研究。高精度直升机航磁测量在大冶铁矿深部找矿的突破,是精细地质缓解储量危机的成功范例。

大冶铁矿经过近 50 年的开采,截至 2004 年 12 月底保有资源储量仅 2 798 万吨,占探明矿山储量的 17%,是典型的危机矿山。矿区周边地形复杂,最大高差达 420 m。“矿区勘探线间距 150 m,钻孔最小间距仅 50 m。在这样复杂地形条件下和如此详细勘探地区,实现找矿突破需采用新方法才能够完成”^[67]。根据矿区的地形、地质背景,中国国土资源航空物探遥感中心使用具国际先进水平的硬架式直升机航磁

测量系统对矿区进行了精细地质调查。航磁调查采用高精度 HC-2000K 型航空磁力仪、DSC-1 航空磁自动数字软补偿仪,工作比例尺 1:10 000^[67]。“测线飞行采用沿地形起伏飞行的方法,平均飞行高度仅 144 m,测线间距 100 m,导航定位精度好于 1 m,测量总精度优于 2 nT”^[17]。研究人员对获取的高精度测量数据,“使用起伏地形条件下高精度重磁剖面解释系统,完成勘探线航磁异常定量反演,最后使用 SUR-PAC 三维建模技术,将反演结果、磁场、钻孔设计位置进行立体显示,为钻探工作布置提供依据”^[67]。“根据航磁异常实施的 ZK 21-8 钻孔,于孔深 721.98~770.37 m 间发现了 6 层铁矿体,累计厚 14.8 m;ZK 26-6 钻孔于孔深 732 m 见矿,铁矿体厚度为 4.44 m;ZK 13-8 于孔深 703.49~732.66 m 之间见到 3 层铁矿,总厚度为 11 m。直升机高精度航磁测量工作,实现了在既有矿体之下深部找矿的重要进展,进一步证实了大冶铁矿龙洞-象鼻山地段深部存在 3 个台阶成矿的认识,增强了在类似危机矿山深部找矿的信心”^[17]。大冶铁矿深部找矿突破的主要原因是探测仪器精度高、空间定位精度高、数据分辨率高、处理解释精细,发现了被前期工作遗漏的弱小异常^[17],工作过程综合使用了物探、GPS、GIS、钻探等技术,是精细地质成功用于找矿勘探的实例。

6 展望

近十几年来中国等人口大国迅速崛起,导致对资源的需求成倍增长(仅北京市就有 500 多万辆汽车的保有量),同时面临的环境问题也日益突出,资源与环境的双重压力,迫使国家政策转向发展与环保并重、长期可持续发展的战略。近期,中国地质调查局也提出了向“深空、深地、深海”进军的工作目标。因此,21 世纪中后期地质工作将由过去单纯满足资源需求,转向经济建设与民生并重,依靠科技进步,在提高矿产资源勘查效率的同时,逐渐向环保、防灾、国安等领域扩展。要实现以上目标,需要遥感、物探、化探等远距离精确探测技术进行高效细致的综合研究。高精度遥感、航空物探已经在汶川地震、福岛核电站泄露及近几年国内发生的数次灾难性滑坡、泥石流等地质灾害的评估、救助、预防等方面发挥了巨大作用。所以,地质工作应转变思路,通过技术方法的更新换代,利用精细调查研究满足资

源供给与环境保护的巨大需求,推动地学研究的进步,实现社会的健康和谐发展。根据技术特点及研究对象的性质分析,精细地质能够在如下领域发挥作用。

以高精度物探技术、高精度空间定位技术以及计算机技术为主体,服务于能源勘查开发行业的精细地质研究。石油行业利用高精度三维地震、密集井网测井资料和计算机建模,对储层物性及其空间展布进行精细研究,为油田的高效勘探与开发提供技术支持;煤炭行业利用高精度三维地震和计算机技术,对常规勘探难以发现的小断层、陷落柱、老窑、采空区等进行精细研究,为煤矿勘探及采区的开发决策、巷道布置与开拓提供可靠依据。

以高精度物探,高精度空间定位及计算机精细解释技术为主体,服务于以铁矿为代表的金属矿产勘查开发,尤其是隐伏矿体和深部矿体的勘探。典型代表是硬架式直升机航磁/放射性测量系统。

以高光谱遥感、数字化岩心扫描、探矿工程信息编录采集和高精度空间定位及计算机解译系统为主体,在矿化蚀变发育的典型矿区,通过空中、地表、地下连续获取三维空间的矿物反射光谱及较高分辨率彩色影像,识别多种地质单元和热液蚀变聚合物,分析成矿流体的运移、就位路径和机制,建立精细的成矿模式及遥感立体找矿模型,利用高新技术推动矿床学的发展,指导矿产资源的勘查开发。

以高光谱遥感、化探、(航空)物探、高精度空间定位技术及计算机解释系统为主体,在重要成矿带利用遥感找矿模型,通过空中、地表、地下多种技术的三维立体综合探测,进行以金属矿产为目的的矿产资源快速详细勘查。

以高空间分辨率和高光谱分辨率遥感,高精度空间定位、显微岩矿鉴定技术为主体,在矿产勘查重点地区、大型电站等重大工程目标区、地学研究热点区等,进行大比例尺区域地质调查,为经济建设、地学基础研究和矿产勘查提供高精度基础地质资料。

以高空间分辨率遥感,同位素精确测年和显微组构研究为主要技术手段,在关键区域对造山作用等重大地质事件演化的时空过程进行精细研究,推动构造地质学的发展。

以高空间分辨率和高时间分辨率遥感,同位素精确测年和高精度空间定位系统为主要技术手段,对海岸带、湖泊、湿地、现代冰川等地质环境敏感地区进行精细调查监测,为现代社会可持续发展提供

决策依据。

以高空间分辨率遥感、高时间分辨率遥感,高精度 DEM 和高精度空间定位系统为主要技术手段,对重要的战略要地进行精细的地质、地理、地貌研究,为国防建设提供具有参考价值的资料。

以高空间分辨率遥感、微波遥感(InSAR)和高精度空间定位系统为主要技术手段,在地质灾害高发区对地表沉降、滑坡、断层构造活动、火山活动等进行定量精细研究,为政府减灾防灾提供依据。

在上述诸多领域实践的基础上,应能逐步总结出各种高新技术在地学调查与研究中融合应用的一般规律,形成比较成熟、系统的工作方法和技术体系,即精细地质调查与研究技术体系(可简称“精细地质技术体系”)。这样,既可满足经济社会发展的需要,又深化了地学研究。假以时日,必能像“精细农业”一样,拓展为集多种科学技术于一身,对地质和环境进行深入细致研究的、新的地学边缘学科——“精细地质学”(Precision Geology)。

本论文就精细地质的现状、发展趋势等问题与中国地质大学(北京)李述靖研究员进行了多次探讨,受益匪浅,在此表示诚挚的感谢!中国国土资源航空物探遥感中心教授级高级工程师乔日新先生和王永江先生,就航空物探测量精度问题进行了探讨,中国国土资源航空物探遥感中心高级工程师张玲提供了干涉雷达的图片,在此一并表示感谢!

参考文献

- [1] 王晋年,李忠志,张立福,等.光谱地壳计划:探索新一代矿产勘查技术[J].地球信息科学学报,2012,14(3):344-351.
- [2] 董树文,李廷栋. Sino Probe:中国深部探测实验[J]. 地质学报,2009,83(7):895-909.
- [3] 常捷,李斌. 3S技术与精细农业[J]. 河南科技,2002,12:26-27.
- [4] 耿爱军,张晓辉,宋涛,等. 精细农业与信息化技术的研究现状与发展趋势[J]. 中国农机化,2011,6:38-41.
- [5] 吴诗勇,李自安. 精细地质研究现状及发展趋势[J]. 地球科学与环境学报,2006,28(2):58-64.
- [6] 赵跃军,范广娟. 精细地质建模中的沉积时间单元标准化研究[J]. 科学技术与工程,2011,11(13):3095-3097.
- [7] 马利民,齐玉柱,高双. 北三区主力油层精细地质研究及剩余油分布探讨[J]. 大庆石油地质与开发,2000,19(1):22-26.
- [8] 隋怡冰. 精细地质研究在实现老区扩边增储中的应用:以锦45-29-281井区为例[J]. 长江大学学报(自然科学版),2012,9(6):43-44.

- [9] 乌丽娟. 精细地质研究锦 45-7-16 块综合调整提高采油速度技术[J]. 内蒙古石油化工, 2010, 6: 6-8.
- [10] 高洋. 运用精细地质研究成果对萨高合采井区开发的再认识[J]. 内蒙古石油化工, 2012, 9: 143-144.
- [11] 李继庆, 姜喜庆, 杜晓明, 等. 精细地质研究在聚合物驱开发中的应用[J]. 大庆石油地质与开发, 2001, 20(2): 57-59.
- [12] 孙致学, 凌庆珍, 邓虎成, 等. 高分辨率层序地层学在油田深度开发中的应用[J]. 石油学报, 2008, 29(2): 239-245.
- [13] 王润生, 熊盛青, 聂洪峰, 等. 遥感地质勘查技术与应用研究[J]. 地质学报, 2011, 85(11): 1699-1733.
- [14] VANE G, GOETZ A F H. Terrestrial imaging spectrometry: current status, future trends[J]. Remote Sensing of Environment, 1993, 44: 117-126.
- [15] 刘树臣. 发展新一代矿产勘探技术: 澳大利亚玻璃地球计划的启示[J]. 地质与勘探, 2003, 39(5): 53-56.
- [16] POSAMENTIER H W, ALLEN G P, JAMES D P. High resolution sequence stratigraphy: the East Coulee Delta, Alberta[J]. Journal of Sedimentary Petrology, 1992, 62(2): 310-317.
- [17] 熊盛青, 于长春, 王卫平, 等. 直升机大比例尺航空物探在深部找矿中的应用前景[J]. 地球科学进展, 2008, 23(3): 270-275.
- [18] CLARK R N, KING T V V, KLEJWA M. High spectral resolution reflection spectroscopy of minerals[J]. Journal of Geophysical Research, 1990, 95(B-8): 12653-12680.
- [19] CLARK N R. Spectroscopy of rocks and minerals, and principles of spectroscopy[R/OL]. United States Geological Survey, 1999-06-25[2016-11-23]. <http://speclab.cr.usgs.gov>.
- [20] BEDINI E. Mineral mapping in the Kap Simpson complex central East Greenland using HyMap and ASTER remote sensing data[J]. Advances in Space Research, 2011, 47(1): 60-73.
- [21] EHLMANN B L, MUSTARD J F, MURCHIE S L. Geologic setting of serpentine deposits on Mars[J]. Geophysical Research Letters, 2010, 37(3): L06201.
- [22] PIETERS C M, GOSWAMI J N, CLARK R N, et al. Character and spatial distribution of OH/H₂O on the surface of the Moon seen by M3 on Chandrayaan-1[J]. Science, 2009, 326: 568-572.
- [23] EUNYOUNG C, FREEK V D M, FRANK V R, et al. Mapping of heavy metal pollution in stream sediments using combined geochemistry, field spectroscopy, and hyperspectral remote sensing: a case study of the Rodalquilar mining area, SE Spain[J]. Remote Sensing of Environment, 2008, 112: 3222-3233.
- [24] GOETZ A F H, CURTISS B, SHILEY D A. Rapid gangue mineral concentration measurement over conveyors by NIR reflectance spectroscopy[J]. Minerals Engineering, 2009, 22: 490-499.
- [25] DONSON M H. Closure temperature in cooling geochronological and petrological systems[J]. Contributions to Mineralogy and Petrology, 1973, 40: 259-279.
- [26] LOVERA O M, RICHTER F M, HARRISON T M. The ⁴⁰Ar/³⁹Ar thermochronometry for slowly cooled samples having a distribution of diffusion domain sizes[J]. Journal of Geophysical Research, 1989, 94: 917-935.
- [27] LOVERA O M, RICHTER F M, HARRISON T M. Diffusion domains determined by ³⁹Ar released during step heating[J]. Journal of Geophysical Research, 1991, 96(B2): 2057-2069.
- [28] 王瑜. 构造-热年代学: 发展与思考[J]. 地学前缘, 2004, 11(4): 435-443.
- [29] 郭毅. 精细磁法在新疆某地隧道工程地质勘察中的应用[J]. 新疆有色金属, 2009(增刊2): 71-73.
- [30] 张彦果. 三维地震勘探资料解释方法[J]. 河北煤炭, 2003, 3: 3-4.
- [31] 李新安. 高分辨率地震技术在宁东煤田构造勘查中的应用[J]. 中国煤炭地质, 2009, 21(7): 57-61.
- [32] 王赟, 卢俊, 于光明. 能识别煤层中垂直断距小于3m的断层吗? [J]. 煤炭学报, 2010, 35(4): 630-634.
- [33] 王宏. 渤海湾西岸海岸带第四纪地质研究成果概述[J]. 地质调查与研究, 2011, 35(2): 81-97.
- [34] 李建芬, 王宏. 泥质海岸现代地质作用(沉积、剥蚀与岸线变迁)及精细测年研究[J]. 科技成果管理与研究, 2013, 82(8): 74-75.
- [35] 周爱锋, 孙惠玲, 陈发虎, 等. 黄土高原六盘山天池记录的中晚全新世高分辨率气候[J]. 科学通报, 2010, 55(22): 2263-2266.
- [36] 王瑜, 李锦铁, 李文铅. 东天山造山带右行剪切变形及构造演化的⁴⁰Ar-³⁹Ar 年代学证据[J]. 新疆地质, 2002, 20(4): 315-319.
- [37] 李齐, 王瑜, 万景林, 等. 秦岭造山带中段中、新生代构造-热冷却过程[J]. 地质论评, 2002, 48(增刊): 135-139.
- [38] 陈文寄, 计凤桔, 王非. 年轻地质体系的年代测定(续): 新方法、新进展[M]. 北京: 地震出版社, 1999: 25-56.
- [39] 陈江峰, 谢智, 刘顺生, 等. 大别山造山带冷却年龄的⁴⁰Ar/³⁹Ar 和裂变径迹年龄测定[J]. 中国科学: B辑, 1995, 25: 1086-109.
- [40] 同全人, 王宗起, 同臻, 等. 构造变形/变质作用的精细测年及其在造山带研究中的应用[J]. 地学前缘, 2001, 8(3): 147-156.
- [41] 李大明, 李齐, 郑德文. K-Ar 和 Ar-Ar 方法的精细测年及其检验[J]. 地震地质, 2005, 27(4): 609-614.
- [42] 杨少平, 孙跃, 弓秋丽. “十一五”以来化探方法技术研究主要进展[J]. 物探与化探, 2014, 38(2): 194-199.
- [43] 刘崇民, 马生明, 胡树起. 金属矿床原生晕勘查指标[J]. 物探与化探, 2010, 34(6): 765-771.
- [44] 李惠, 禹斌, 李德亮. 构造叠加晕找盲矿法及找矿效果[M]. 北京: 地质出版社, 2011.

- [45] 张必敏. 戈壁覆盖区深穿透地球化学异常形成机理与找矿方法[D]. 北京: 中国地质科学院, 2011.
- [46] 杨金中, 孙延贵, 秦绪文, 等. 高分辨率遥感地质调查[M]. 北京: 测绘出版社, 2013: 66-209.
- [47] 王润生, 甘甫平, 闫柏琨, 等. 高光谱矿物填图技术与应用研究[J]. 国土资源遥感, 2010, 84(1): 1-13.
- [48] 甘甫平, 王润生, 马萬乃, 等. 遥感地质信息提取集成与矿物遥感地质分析模型[J]. 遥感学报, 2003, 7(4): 207-213.
- [49] 甘甫平, 王润生, 马萬乃. 基于特征谱带的高光谱遥感矿物谱系识别[J]. 地学前缘, 2003, 10(2): 445-453.
- [50] 刘圣伟, 甘甫平, 王润生. 用卫星高光谱数据提取江西德兴铜矿山废水 pH 值污染指标[J]. 地质通报, 2003, 22(11/12): 1013-1020.
- [51] 杨佳佳, 姜琦刚, 陈永良, 等. 基于最小二乘支持向量机和高分辨率遥感影像的大尺度区域岩性划分[J]. 中国石油大学学报(自然科学版), 2012, 36(1): 60-67.
- [52] 葛大庆, 王艳, 郭小方, 等. 基于相干点目标的多基线 D-InSAR 技术与地表形变监测[J]. 遥感学报, 2007, 11(4): 574-580.
- [53] 葛大庆, 王艳, 郭小方, 等. 利用短基线差分干涉纹图集监测地表形变场[J]. 大地测量与地球动力学, 2008, 28(2): 61-66.
- [54] 崔丽萍, 王晓青, 窦爱霞, 等. 基于高分辨率合成孔径雷达影像建筑物成像几何结构的震害特征分析[J]. 地震学报, 2016, 38(2): 272-282.
- [55] 和正民, 燕云鹏, 冯敏, 等. 区域生态地质环境综合评价系统设计与示范应用[J]. 国土资源遥感, 2007, 81(4): 118-121.
- [56] 杨金中, 秦绪文, 聂洪峰, 等. 中国矿山遥感监测[M]. 北京: 测绘出版社, 2014: 1-66.
- [57] 刘刚, 燕云鹏, 刘建宇, 等. 中国西部艰险地区遥感地质综合调查工作指南[M]. 北京: 地质出版社, 2016: 19-50.
- [58] 王治华. 数字滑坡技术及其应用[J]. 现代地质, 2005, 19(2): 157-164.
- [59] 王治华. 中国滑坡遥感及新进展[J]. 国土资源遥感, 2007, 4(4): 7-10.
- [60] 李勇, 王志勇, 马全明. 利用 3S 集成技术进行矿区沉陷精确调查与分析[J]. 测绘通报, 2014(7): 63-65.
- [61] 李占飞, 刘静, 邵延秀, 等. 基于 LiDAR 的海原断裂松山段断错地貌分析与古地震探槽选址实例[J]. 地质通报, 2016, 35(1): 104-116.
- [62] 熊盛青. “十五”以来我国航空物探进展与展望[J]. 物探与化探, 2007, 31(6): 479-484.
- [63] 王丹丹, 李世臻, 周新桂, 等. 大兴安岭地区突泉盆地高精度重磁电特征及其构造格架[J]. 吉林大学学报(地球科学版), 2016, 46(1): 240-253.
- [64] 杨春成, 韩革命, 杨亚斌, 等. 高精度重磁测量在大兴安岭找矿工作中的应用[J]. 地球物理学进展, 2013, 28(3): 1472-1482.
- [65] 王林峰, 刘刚, 周永章. 自相似性在遥感构造研究中的应用[J]. 国土资源遥感, 2010, 84(2): 1-6.
- [66] 刘颖, 刘刚. 显微构造研究方法在韧性剪切带遥感分析中的应用[J]. 吉林大学学报(地球科学版), 2010, 40(3): 597-602.
- [67] 于长春, 范正国, 王乃东, 等. 高分辨率航磁方法及在大冶铁矿区的应用[J]. 地球物理学进展, 2007, 22(3): 979-983.



光谱地质遥感研究进展

摘要

地质遥感是最能体现与发挥光谱遥感技术特点与优势的应用领域之一。本文从矿物岩石光谱模拟、矿物岩石光谱特征分析、遥感光谱仪技术指标的优化设计、辐射定标与数据辐射校正、地表光谱反演、信息提取、信息产品验证、地质应用 8 个方面总结了最新的研究进展，并对目前光谱遥感地质应用存在的问题和发展趋势进行了深入的论述。

关键词

地质遥感；找矿预测；光谱模拟；信息提取

中图分类号 TP79;P627

文献标志码 A

0 引言

自 20 世纪 80 年代成像光谱遥感 (Imaging Spectral Remote Sensing) 概念出现以来，成像光谱仪快速发展，每个像元均可获取数十至数百个谱段 (光谱分辨率达到 $\lambda/100$ 甚至更高)，组成一条近连续的光谱曲线，进而可根据地物光谱精细特征进行信息提取与反演^[1]，使遥感地物识别能力大幅提升，同时促进了数据处理技术的发展。由于光谱分辨率较高，也称为高光谱。成像光谱技术的兴起与发展，极大地增强了遥感对地观测能力和对地物的鉴别能力，使遥感从鉴别 (discrimination) 发展到对地物的直接识别 (identification)，使遥感工作方法由图像分析转变为以谱分析为主的图谱结合模式，也使遥感应用逐渐摆脱“看图识字”的阶段，而越来越依赖于对地物波谱特征的定量分析和理解。

光谱地质遥感的主要研究内容有矿物岩石光谱模拟、矿物岩石光谱特征分析、遥感光谱仪技术指标的优化设计、辐射定标与数据辐射校正、地表光谱反演、信息提取、信息产品验证、应用研究 8 个方面 (图 1)。地表光谱反演是消除大气、地表温度获得地表反射/发射光谱的过程，不同的谱段方法不同，在热红外谱段包括大气校正与温度-发射率分离，在中红外谱段包括反射-发射分离，本文统称为地表光谱反演。本文从矿物岩石光谱模拟、地表光谱反演、信息提取、信息产品验证、应用研究等方面对研究进展进行了分析，最后从上述 8 个方面对目前进展、存在问题及发展趋势进行了讨论，提出一家之见，以资参考。

1 矿物岩石光谱模拟

地物波谱谱形和特征与地表物质成分、物理状态 (如粗糙度、阴影等)、观测几何条件 (光源-地物-探测器的相互几何关系) 等因素有关，了解这些因素如何影响地物波谱特征变化是开展遥感信息提取及应用的重要基础。长期以来对这些知识的获取主要依靠大量的波谱测试，进而进行归纳总结。随着遥感技术定量化、精细化的不断发展，数值模拟技术逐渐成为人们深入了解光线与传输介质 (陆地、水体、大气等) 相互作用机理的有力工具，发展了针对不同行业应用的多种模型，如大气辐射传输模型、植被辐射传输模型、几何光学模型等。针对粉末状岩矿反射光谱模型最常用的是辐射传输模型，其中 Hapke

收稿日期 2017-11-24

资助项目 重大科学仪器设备开发专项(2012YQ05025006)；国防科工局高分专项(04-Y20A35-9001-15/17)；国家自然科学基金(41102208)；中国地质调查局项目(DD20160068)

作者简介

甘甫平，男，博士，研究员，主要从事国产卫星国土资源应用综合论证、高光谱遥感技术方法研究和地学应用工作。fpgan@aliyun.com

1 中国国土资源航空物探遥感中心，北京，100083

2 国土资源部航空地球物理与遥感地质重点实验室，北京，100083

模型最有代表性^[2],但模型应用、参数求解仍不十分明确

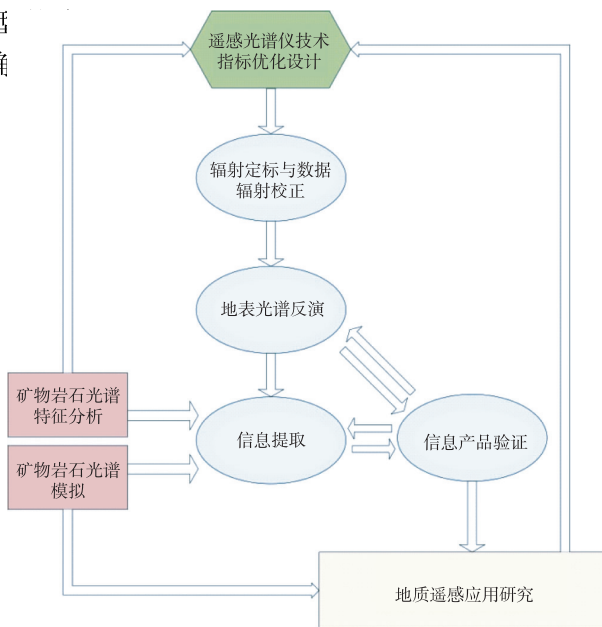


图1 光谱地质遥感主要研究内容及相互关系

Fig. 1 Main contents of spectral geological remote sensing and relationships among them

文献[3]以LSCC月壤作为光谱模拟分析的试验样品,进行了光谱模拟试验。选择月壤的原因有:1)月壤的矿物组成复杂,特别是空间风化形成的单质铁含量少,对光谱的影响大,模拟难度大,可更彻底地检验模型的模拟能力;2)LSCC样品测试分析条件严格,数据齐全,测试科目包括光谱、矿物组成及含量、粒度等。运用Hapke各向异性的多次散射近似(AMSA)辐射传输模型,反演各个矿物端元的光学常数。光学常数作为矿物成分的函数不可以认为在任何情况下都是确定不变的,它依赖于模型的质量以及粒子样本的选择。在反演矿物光学常数时,让矿物粒径在实测粒径范围内迭代,考虑光学常数符合一定光学意义以及反演误差尽可能低,筛选得到最优的粒径及矿物光学常数。同时,采用蒙特卡罗的思想,反演矿物光学常数时在一定约束条件下随机设置反演初值并进行优化求解,找到所有优化结果中的最优解,进一步克服了模型优化中陷入局部最优解的问题,提高了利用Hapke模型反演光学常数的准确性。

利用反演得到的矿物端元的光学常数,模拟了不同粒径、观测条件及矿物混合比例下的月壤光谱数据集。模拟的数据在光谱、矿物含量、粒径3个方面与实测数据吻合度很高,足以说明上述模拟思路可实现矿物光谱的高精度模拟。光谱的模拟误差为0.003~0.005(均值为0.004,图2),矿物含量模拟

复相关系数为0.81~0.99(均值为0.94,图3),单质铁的含量模拟相关系数为0.61~0.66,粒度范围为0~45 μm,与实测值一致。

2 地表光谱反演

2.1 可见-短波红外反射率反演

国内外针对可见光-短波红外谱段(0.35~2.5 μm)的大气校正方法,归纳起来大致可分为以下3大类:1)根据图像统计特征对图像辐射值作归一化处理的相对辐射校正方法,如暗目标法;2)利用地面实测波谱的地空回归分析方法;3)基于大气辐射传输模型的方法。前2种方法普适性、可推广性、精度较低,支撑业务化应用主要是第3种方法。

大气水汽时空变化大,对光谱的影响大、范围宽,是在可见光-短波红外谱段大气校正中需考虑的主要影响因素。对于高光谱数据,可利用820、940、1135 nm附近的大气水汽吸收谱带进行大气水汽分布反演,进而最大程度地消除大气影响^[4];对于多光谱数据,特别是水汽吸收谱带处未设置谱段的数据,大气校正难度较大,需要借助一定的地面光谱先验知识、数据,大致估算整景影像内的大气水汽值^[5]。

大气校正模块HATCH(High-accuracy Atmospheric Correction for Hyperspectral Data)中除应用更高精度的大气辐射传输模型外^[6],还改变了以往采用的3波段比值法,而采用“光谱平滑度”法进

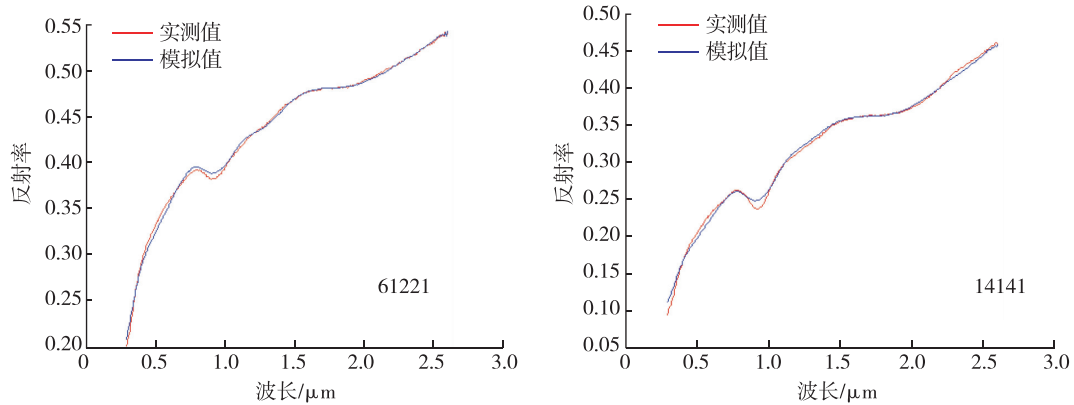


图 2 矿物粉末集合体(月壤)模拟与实测光谱对比^[3]

Fig. 2 Comparisons between simulated and measured spectra of mineral powder aggregate (lunar soil)^[3]

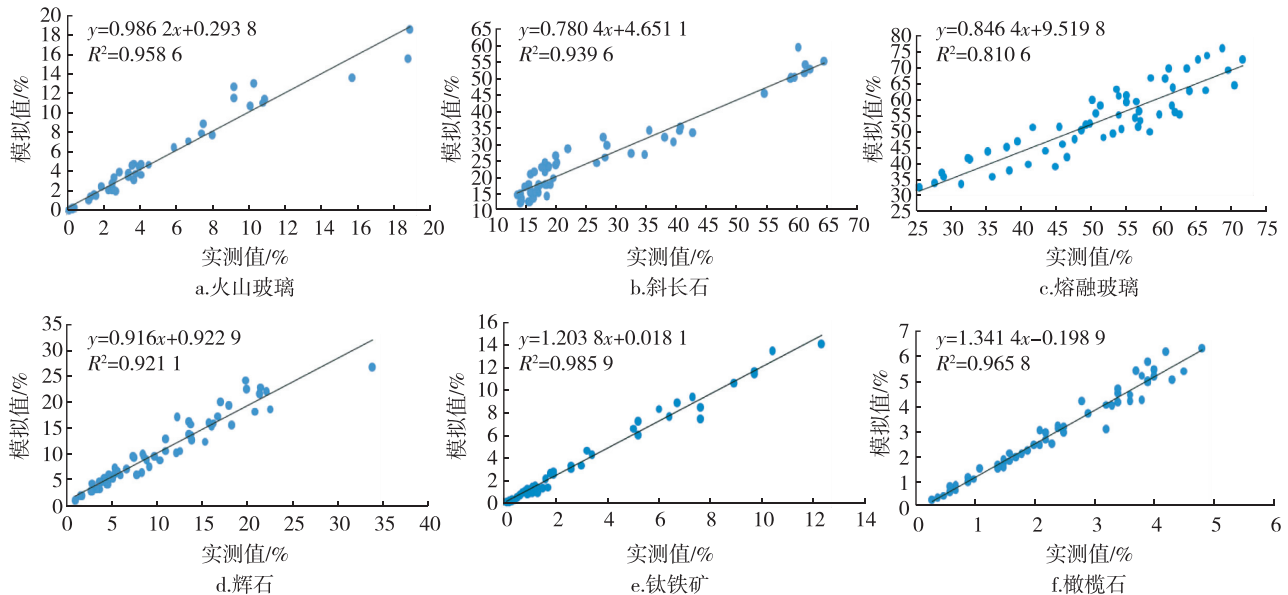


图 3 LSCL 月壤样本模拟与实测矿物丰度对比^[3]

Fig. 3 Comparisons between simulated and measured mineral abundance of LSCL samples^[3]

行大气水汽含量提取,可避免 1 135 nm 等大气水汽吸收谱段地物光谱的影响.

2.2 中红外谱段反射率反演

中红外谱段信息传输原理示意如图 4 所示. 传感器接收到的辐射信息包括 5 个部分, 其中 L_1 代表大气程辐射, L_2 表示大气反射太阳辐射, L_3 表示地表反射辐射经大气传输到达传感器的辐亮度, L_4 表示地表发射辐射经大气辐射传输到达传感器的辐亮度, L_5 表示临近地物的辐射经大气传输到达传感器的辐亮度. 可见, 全谱段相机的中红外谱段数据其实同时包含了目标地物的发射信息和反射信息, 这就造成了中红外波段数据发射率反演的复杂性. 目前针对中红外谱段大气校正和发射率反演技术相对其

他谱段研究较少, 但基本原理清晰.

根据图 4, 中热红外谱段辐射传输公式为

$$\begin{aligned} L &= L_1 + L_2 + L_3 + L_4 + L_5 = \\ &= L_1 + L_2 + (E_1 + E_2)(1 - \varepsilon) / \pi + \\ &\quad P(T)\varepsilon\tau + L_d(1 - \varepsilon), \end{aligned}$$

其中 $L_1, L_2, E_1 + E_2, \tau, L_d, P(T), \varepsilon$ 分别为大气程辐射、大气反射太阳辐射、地表的太阳辐照度(包括直接辐射与大气散射辐射)、大气透过率、大气下行辐射、黑体辐射亮度、地表发射率. 前 5 个参数可基于大气辐射传输模型计算得出, 黑体辐射亮度可基于热红外谱段得到的地表温度, 再根据普朗克定律计算得到. 得到这些参数后, 可利用上式计算得到地表发射率.

综合上述分析,在地质遥感中,中红外谱段的反射、发射分离,进行反射光谱反演,必须有热红外谱段,并可以用地表温度数据作辅助.

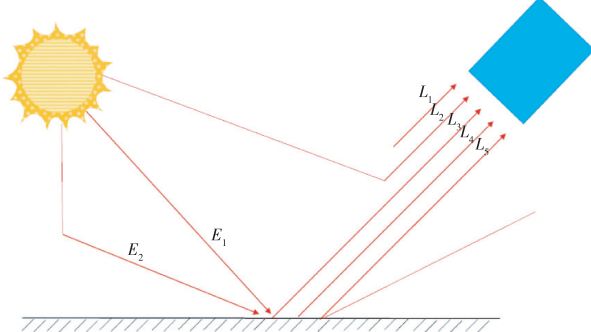


图 4 中红外谱段信息传输原理

Fig. 4 Schematic diagram of information transmission in the middle infrared spectrum

2.3 热红外谱段发射率反演

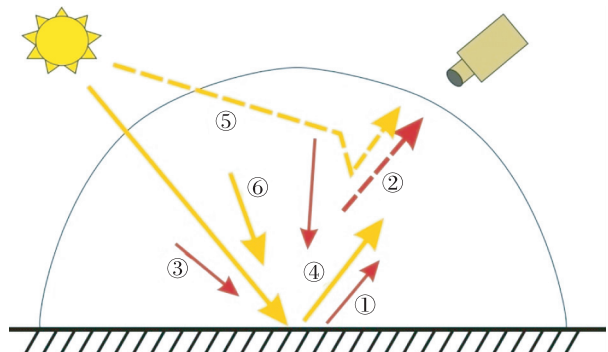
2.3.1 大气辐射传输

热红外窗口,传感器接收总辐射能的包括 6 个部分(图 5):地表热辐射能、程辐射能(大气上行辐射能)、反射的大气热辐射能(大气下行辐射)、反射的太阳直射辐射能、散射太阳辐射能和反射太阳散射辐射能,公式表示如下^[7]:

$$L(\lambda, \mu) = t_1(\lambda, \mu) \times \varepsilon(\lambda, \mu) \times B(\lambda, T_s) + L_a(\lambda, \mu) + L_s(\lambda, \mu, \mu_0, \varphi_0) + t_2(\lambda, \mu, \mu_0) \times \mu_0 \times E_0(\lambda) \times f_r(\mu, \mu_0, \varphi) + \int_0^{2\pi} \int_0^1 \mu' \times f_r(\mu, \mu', \phi') \times [t_3(\lambda, \mu) \times L_d(\lambda, -\mu', \phi') + t_4(\lambda, \mu) \times L_t(\lambda, -\mu', \phi')] d\mu' d\phi',$$

式中 μ 为观测天顶角的余弦, μ_0 为太阳天顶角的余弦, $B(\lambda, T_s)$ 是地表温度为 T_s 的黑体辐射值, φ_0 为观测方位与太阳入射方位之间的相对方位角, $\varepsilon(\lambda, \mu)$ 为地表发射率, $L(\lambda, \mu)$ 为传感器接收总辐射能, $L_a(\lambda, \mu)$ 为程辐射能, $L_s(\lambda, \mu, \mu_0, \varphi_0)$ 为散射的大气热辐射能, $E_0(\lambda)$ 为大气顶层的太阳总辐射, $f_r(\mu, \mu_0, \varphi)$ 为双向反射率分布函数, $L_d(\lambda, -\mu', \varphi')$ 为向下太阳漫射辐射能, $L_t(\lambda, -\mu', \varphi')$ 为大气下行辐射能, 入射方向为 $-\mu', \varphi'$, $t_i (i=1, 2, 3, 4)$ 为相应的传递函数.

在热红外大气窗口内,太阳辐射可以忽略,即忽略反射的太阳直射辐射、散射的太阳辐射、反射的太阳散射辐射. 传感器接收的总辐射能主要包括 3 部分:地表热辐射能、大气下行辐射能、大气上行辐射能. 在基于地表朗伯体的假设下,结合基尔霍夫定



①地表热辐射;②大气上行辐射;③反射的大气热辐射;
④反射的太阳直射辐射;⑤散射的太阳辐射;⑥反射的太阳散射辐射

图 5 传感器接收辐射能

Fig. 5 Schematic diagram of sensor receiving radiation energy

律,可知地表反射率 $\rho(\lambda) = 1 - \varepsilon(\lambda)$, 因此传感器接收的总辐射能可以表示为

$$L(\lambda) = \tau(\lambda)(\varepsilon(\lambda)B(\lambda, T) + (1 - \varepsilon(\lambda))L_{down}) + L_{up},$$

式中, λ 为对应的波长, $L(\lambda)$ 为传感器记录的目标地物辐亮度值, $B(\lambda, T)$ 为温度为 T 时的黑体辐亮度, $\tau(\lambda)$ 为大气透过率, L_{down} 为大气下行辐射, L_{up} 为大气上行辐射. 可用 $L_{grd} = \varepsilon(\lambda)B(\lambda, T) + (1 - \varepsilon(\lambda))L_{down}$ 表示为地表出射辐射能. 同时大气辐射传输公式也说明热红外探测是一个地-气耦合的体系.

2.3.2 大气校正

大气校正的主要任务就是反演大气上行辐射、大气下行辐射和透过率^[8](图 6). 目前, 热红外谱段常用的大气校正方法包括: 基于图像自身的大气校正、基于辐射传输模型的大气校正. 基于图像自身的大气校正假设整景影像内大气条件均一, 以及影像内有接近于黑体的地物(水体、植被)存在, 并且在校正中忽略大气下行辐射的影响. 首先, 计算每个像元的亮温(假设发射率为 1), 然后在亮温-卫星辐射亮度值散点图的基础上进行线性拟合, 其斜率就是大气透过率, 截距就是大气上行辐射^[9]. 该方法简单易行, 但难以大面积推广应用, 在大多数情况下可能校正效果很差. 基于辐射传输模型的大气校正一般用 MODTRAN 计算出大气透过率、大气上行辐射、大气下行辐射等大气校正参数, 之后利用这些参数实现大气校正. 大气温度廓线、湿度廓线、臭氧等大气状态参数是大气校正参数能否准确计算的关键. 同步大气温度廓线、湿度廓线可利用 MODIS 数据及气象数据反演得到.

在以往的研究中,对于岩矿信息提取而言,采用

标准大气廓线进行大气校正同样可以得到令人满意的效果,初步模拟试验也表明大气廓线误差主要影响温度信息提取,对于发射率谱形影响相对较小.因此,在地质遥感中,利用其他遥感数据同步反演大气廓线并进行热红外数据大气校正是长远的发展趋势,但基于标准大气模式廓线进行大气校正可能会在今后相当一段时间内是主流方法.

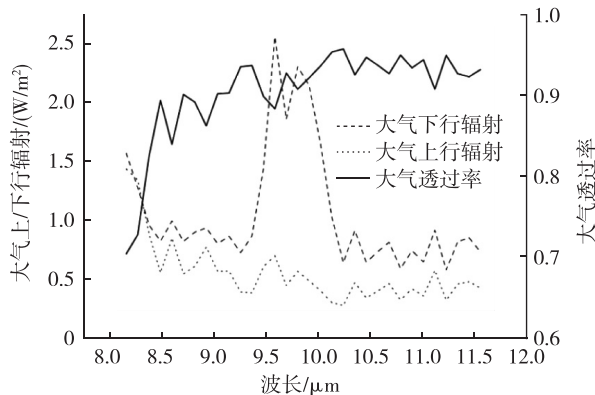


图 6 MODTRAN 反演得到的与 TASI 波段
对应的大气上下行辐射和透过率^[8]

Fig. 6 The upwelling path radiance, down-welling sky radiance, and atmospheric transmittance from the MODTRAN software for the TASI data^[8]

2.3.3 温度发射率分离

热红外波段温度发射率分离方法有模式发射率法、昼夜法、灰体发射率法、比值法、发射率归一化法、温度-发射率分离法等.其中发射率归一化法在地质遥感中应用普遍,该方法允许最大发射率 ε_{\max} 波长随像元而改变. ε_{\max} 最大值是固定的,然而不关心是哪一个通道.由于该算法允许对应 ε_{\max} 的波长改变,因此将比简单的模型发射率算法有更小的误差.ASTER 热红外数据温度发射率迭代分离方法是在

发射率归一化法的基础上发展而来的,可同时反演地表温度与发射率.数值模拟研究表明^[10], ASTER 热红外数据 TES 反演温度误差一般小于 1.5 K, 发射率误差一般小于 0.015, 精度分别为 0.4 K 与 0.03.

基于上述温度-发射率分离算法,进行了机载 TASI 数据(核工业北京地质研究院获取)温度发射率分离^[8](图 7、8).

3 信息提取

3.1 传统信息提取方法及问题

国内外发展的矿物信息提取方法有基于光谱相似性与基于光谱特征参量的 2 大类.基于光谱相似性就是将重建光谱与参考光谱相比较,在某种光谱相似性测度(光谱距离、光谱角等)下计算端元光谱与像元光谱相似性来完成矿物信息识别.常用的光谱匹配方法有距离法(欧式、马氏距离)^[11]、光谱角^[12]、匹配滤波、光谱信息散度^[13-14]、混合调制匹配滤波等方法.光谱匹配又可分为整体光谱匹配和局部光谱匹配.整体匹配利用了整个光谱的形状特性,受照度、光谱定标和光谱重建精度等的影响较小,但受矿物光谱的不确定性影响较大,对矿物光谱的微小差异不够敏感,容易受地形、背景等外界干扰,且无法突出光谱吸收谷谱形在相似性计算中的重要性;局部匹配方法对矿物光谱的微小差异比较敏感,但仅利用了特定的一些特征,受图像的信噪比、光谱定标和光谱重建精度等因素的影响较大^[15].

基于光谱特征参量信息提取是以诊断性光谱吸收谱带的特征参量为基础的局部光谱识别方法.光谱吸收谱带的特征可以用一些特征参数来度量,这些参数有谱带的波长位置(P)、波段深度(H)、宽度(W)、斜率(K)、面积(A)及对称度(S)等^[16].代表性



图 7 TASI 数据 Band32/22/11 波段假彩色合成图像^[8]

Fig. 7 False color composite image of TASI data (R:band 32, G:band 22, B:band 11)

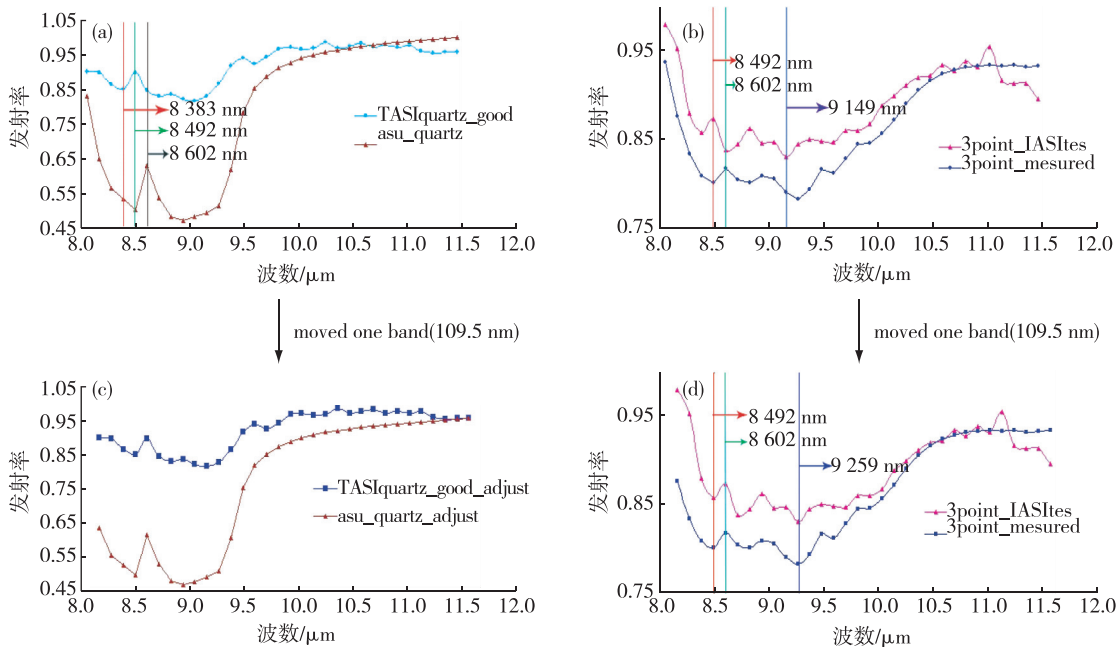


图 8 通过 TES 方法反演的石英、花岗岩发射率波谱曲线与 ASU 光谱库中两者重采样自 TASI 波谱范围的波谱曲线对比,
(a) 石英,(b)花岗岩,(c)石英移动一个波段,(d) 花岗岩移动一个波段^[8]

Fig. 8 Comparisons between the quartz and granite emissivity spectral curves retrieved from TASI data by the TES method and their spectral curves in the ASU spectrum resampled from the spectrum range of TASI,
(a) quartz,(b) granite,(c) quartz after moving one band, and (d) granite after moving one band^[8]

的方法有光谱特征拟合(SFF, Spectral Feature Fitting)、光谱吸收指数(SAI, Spectral Absorption Index)和吸收谱带定位分析(AABP, Analysis of Absorption Band Positioning)等。甘甫平等^[17]提出了基于特征谱带的高光谱遥感矿物谱系识别方法,该方法根据矿物诊断性吸收谱带特征、多谱带组合特征的相似性和稳定性以及不同具体矿物谱带特征的变异性,初步建立了“矿物大类-族-种-亚种”的矿物识别分层谱系。基于光谱特征参量法相对于光谱匹配法,增强了对地物的区分能力,但在实际应用中,易受光谱信噪比、矿物混合影响^[15]。

如果在光谱匹配结果的基础上,再运用光谱特征参量法,将会极大地提高光谱特征参量法的优势,但这需要以准确的匹配结果为基础。

3.2 现有光谱匹配度识别能力分析

基于模拟的混合光谱,对光谱角、信息散度、相关系数、特征拟合、匹配滤波等常用的光谱匹配度识别算法的识别能力进行分析。各识别指数对矿物的识别能力的评价方法为,计算识别指数与待识别矿物含量的相关系数,相同矿物(端元与待识别矿物相同)的相关系数越大,不同矿物(端元与待识别矿物不同)的相关系数越小,说明该识别指数的识别能力越强。如,将高 Al 白云母作为端元计算与模拟的混合光谱之间的光谱角,得到的光谱角与高 Al 白云母含量的相关性越大,说明光谱角对矿物的识别能力较高,与其他矿物含量之间的相关性越小,说明光谱角的抗误识别能力较高。据此,提出了如下表征光谱相似性指数区分识别不同矿物的能力的误识别指数:

$$I = \text{abs} \left(E_{ii} - \frac{\sum_{k=1, k \neq i}^n E_{ik}}{n} \right),$$

式中, I 为判别指数, E_{ik} 为 i 端元矿物与 k 矿物相似性指数与其 k 矿物含量的相关系数。误识别指数越大,抗误识别能力越强。用所有矿物相似性识别指数与含量相关系数的绝对值作为相似性算法的识别指数,识别指数越大,对矿物的识别能力越强。

混合光谱模拟计算流程如图 9 所示。从 USGS 光谱库中选取所需的端元光谱,运用 Hapke 模型进行随机非线性混合,生成地面随机混合光谱。之后,所有光谱乘以一个随机乘性因子,用于模拟地形对光谱的影响。最后,加入随机加性噪声,用于模拟仪器与大气噪声,生成模拟光谱库。真实的成像光谱数据获取时,地面与大气之间有多次散射作用,模拟难度

较大,该试验利用一个随机乘性因子模拟地形影响而忽略了这一复杂的物理过程.对于仪器噪声,采用加性噪声模拟.大气对光谱的影响以大气水汽影响为主,水汽校正误差较大时会在光谱中加入锯齿状的噪声,试验中同样运用随机加性噪声模拟.

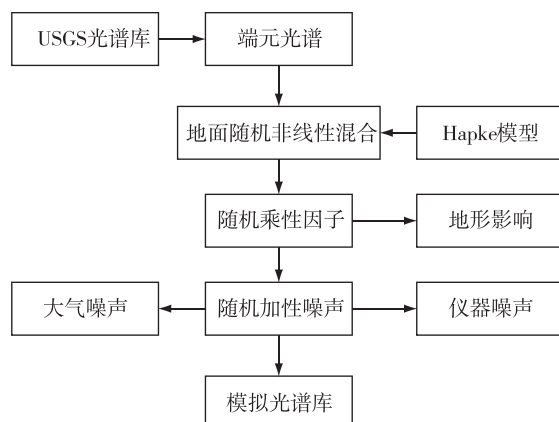


图9 混合光谱模拟计算流程

Fig. 9 Simulation process of mixed spectrum

基于上述模拟流程,模拟计算了黄铁绢英岩化、青盘岩化、铁染3种常见的金属矿床蚀变类型的反射光谱(400~2 500 nm)(表1).在黄铁绢英岩化、青盘岩化、铁染3种蚀变岩性光谱模拟中,均加入了黄铁矿与石英,目的是更好地模拟在可见光-短波红外无吸收特征的矿物对光谱特征的影响,使模拟结果更接近于真实情况.

根据最后的识别指数统计结果,识别能力排序为匹配滤波、相关系数、光谱角、信息散度、光谱特征拟合(表2).

通过分析认为上述匹配度识别能力低的原因有2方面:1)匹配度容易受光谱背景干扰;2)匹配度容

易受光谱特征强度的影响.

表1 混合光谱端元列表

Table 1 Mixed spectrum endelement list

蚀变岩性	混合端元矿物
黄铁绢英岩化	高铝白云母、中铝云母、低铝白云母、高岭石、高铝蒙脱石、低铝蒙脱石、地开石、埃洛石、伊利石、石英、黄铁矿
青盘岩化	绿泥石、绿帘石、方解石、白云石、石英、黄铁矿、蛇纹石、透闪石
铁染	褐铁矿、针铁矿、赤铁矿、黄钾铁矾、石英、黄铁矿、绿泥石、绿帘石

表2 矿物误识别指数统计

Table 2 Statistics of mineral identification index

光谱角 识别指数	信息散度 0.41	相关系数 0.39	匹配滤波 0.45	光谱特征拟合 0.59	0.177

3.3 基于光谱特征增强的匹配度算法

在上述分析的基础上,我们提出了基于光谱特征增强的匹配度算法.光谱特征增强匹配的核心步骤(图10)有:1)参考光谱与影像光谱均应首先去连续统;2)对影像光谱进行增强之后计算匹配度.匹配度以所有波段反射率(去连续统后)之差的绝对值之和除以波段数.光谱特征增强的基本原理是,假设光谱是反射率值为1的端元光谱与光谱自身的线性混合,通过调整二者的混合比例(比例可以为负),直至参考光谱最小位置处参考光谱与影像光谱重合.

以Cuprite地区的AVIRIS高光谱数据为例,分别用匹配滤波方法和光谱特征增强匹配度法对明矾石进行匹配识别.将USGS光谱库中的明矾石光谱重采样到AVIRIS影像光谱,依据明矾石的光谱谱形特征,选取2.08~2.25 μm谱段进行匹配(图11).从匹配结果上看(图12),基于光谱特征增强匹配法识别

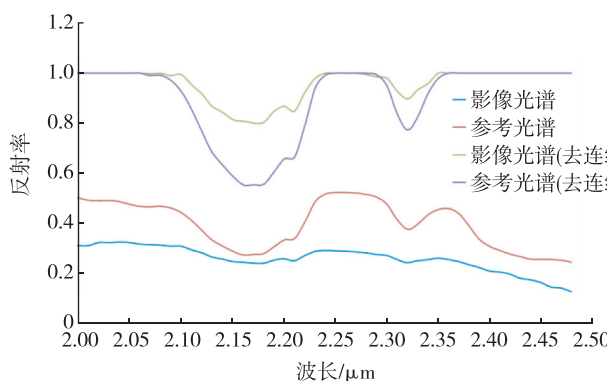


图10 光谱特征增强匹配度概念图

Fig. 10 Conceptual map of spectral feature enhancement matching degree

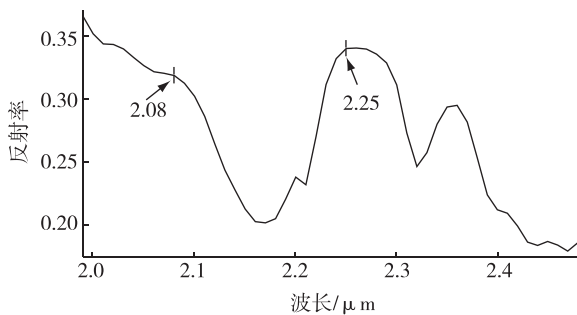


图 11 重采样至 AVIRIS 影像的明矾石光谱

Fig. 11 Alunite spectra resampled from USGS to AVIRIS images

的明矾石范围明显要比匹配滤波法广泛。根据匹配结果,对影像光谱进行检查,在图 12 中点 1 匹配滤波没有识别出明矾石信息,但影像光谱检查发现该点确实含有明矾石(图 13,左图)。同时,从图 12 中还可明显发现,在点 2 和点 3 匹配滤波方法识别出了明矾石信息,而光谱特征增强匹配法并没有识别出明矾石。通过检查影像光谱发现,点 2、3 处没有明矾石信息,可能为绢云母信息(图 13)。从整体上看,用匹配滤波方法识别出的明矾石像元数约为 15 000 个(含误识别像元),而光谱特征增强匹配度法识别出

的明矾石像元数约为 65 000 个,这大约是匹配滤波方法矿物识别检出率的 4~5 倍。随机选择了 50 个验证点,对 2 种方法的正确率进行了估算,其中匹配滤波发现 10 个验证点识别错误,而光谱特征增强匹配度法有 2 个验证点被认为可能识别有误,因此,光谱特征增强匹配度法相对于匹配滤波法明矾石的识别正确率由大约 80% 左右提升至了 95% 以上。

由此可见,光谱特征增强匹配法要比匹配滤波法识别矿物信息的检出限更低,正确率更高。

用光谱特征增强匹配法对矿物混合体识别检出率进行了实验,以福建紫金山金铜矿样品为试验对象进行了分析。紫金山金铜矿样品主要矿物组合为明矾石、地开石、石英和少量的黄铁矿,共 65 件粉末样品。明矾石和地开石在主要特征谱带重合度相对较高,对两者混合样开展识别检出率试验具有一定的代表性。但受样品数量、样品中矿物种类所限,该分析结果仅作为参考。依据明矾石和地开石矿物的谱形特征,选取相对容易区分其他矿物的光谱段进行匹配,明矾石在 1 380~1 540 nm 光谱段的匹配结果显示,当样品低于 6% 时,匹配结果会出现误识别,样品中含有明矾石的,均含有地开石;当样品含有明

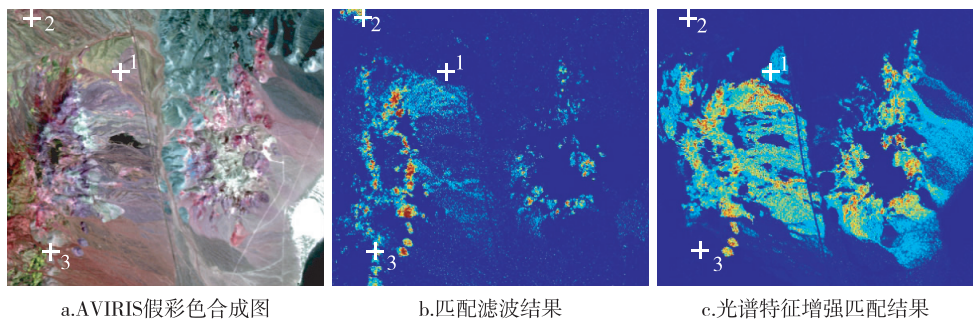


图 12 明矾石匹配结果

Fig. 12 Matching results of alunite. The AVIRIS false color composite image (a), the matched filtering results (b), and spectral feature enhancement matching results (c)

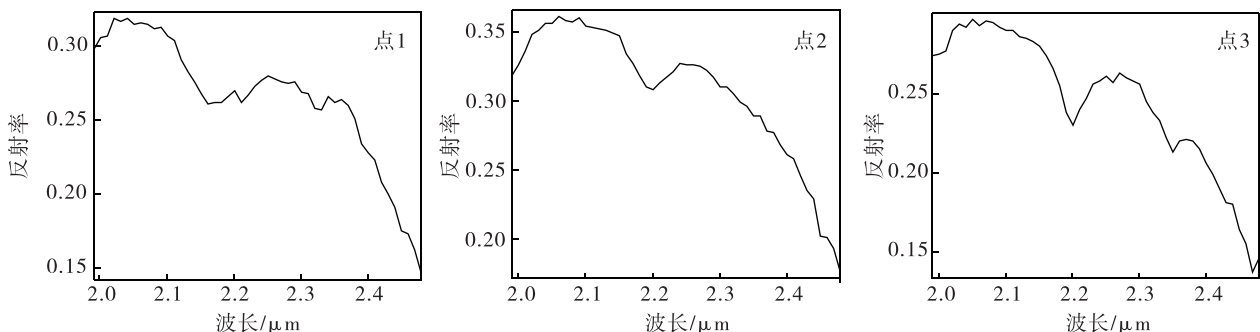


图 13 检查点影像光谱

Fig. 13 Image spectra of checkpoints

矾石时(大于4%),无论是否含有地开石,其匹配值均在0.053以上.地开石在2 130~2 240 nm光谱段的匹配结果显示,当样品中地开石含量低于4%,同时含有明矾石矿物时,匹配结果低于0.07时,会出现误识别;当样品中不含明矾石时,石英含量为99%、地开石为1%时,匹配值为0.1(表3).

表3 实验室矿物混合体识别检出率

Table 3 Detection rates of mineral mixture identification

序号	矿物	谱段/nm	识别检出率/%
1	明矾石(含地开石)	1 380~1 540	6
	地开石(不含明矾石)	2 130~2 240	1
2	地开石(含明矾石)	2 130~2 240	4

3.4 基于全约束光谱分解矿物含量半定量提取方法

一种基于全约束光谱分解的矿物含量半定量提取方法——矿物含量/丰度反演方法流程见图14.第1步:端元选择,可基于先验知识的端元选择,也可基于图像的端元选择,运用高光谱遥感端元提取的方法提取端元.端元的光谱在USGS光谱库中选取.第2步:运用Hapke模型计算随机混合光谱,端元光谱除第1步选取的光谱之外,应加如一些造岩矿物

或金属矿物光谱,随机混合光谱的计算方法为运用Hapke将各端元光谱转换为单次散射反照率,运用线性混合原理计算随机混合的单次散射反照率,再运用Hapke模型将随机混合的单次散射反照率转换为混合反射率.第3步:对随机混合的反射光谱进行去连续统分解,分解前对端元光谱与混合光谱去连续统,在端元光谱中加入所有谱段均为“1”的光谱代表光谱不活跃的端元,建立光谱分解的丰度与光谱随机混合时随机设定的丰度之间的统计关系.第4步:对高光谱数据进行去连续统分解,得到光谱分解丰度,根据第3步建立的统计关系,将光谱分解丰度转换为矿物丰度.

同样以福建紫金山金铜矿样品为试验对象,对该方法进行了测试.端元选择根据样品XRD(X射线衍射分析)测试结果,选取了地开石、明矾石、伊利石、石英.采用图14的方法与流程进行了矿物丰度的反演.运用Hapke模型建立了各种矿物光谱分解丰度与真实丰度的统计关系,用于修正光谱非线性混合效应所致的误差.从图15可看出,反演的地开石含量与样品XRD测试结果相关性很高, R^2 达到0.762,线性关系基本接近“ $y=x$ ”,计算反演值与实测值的均方根值(RMS)为12.4%.

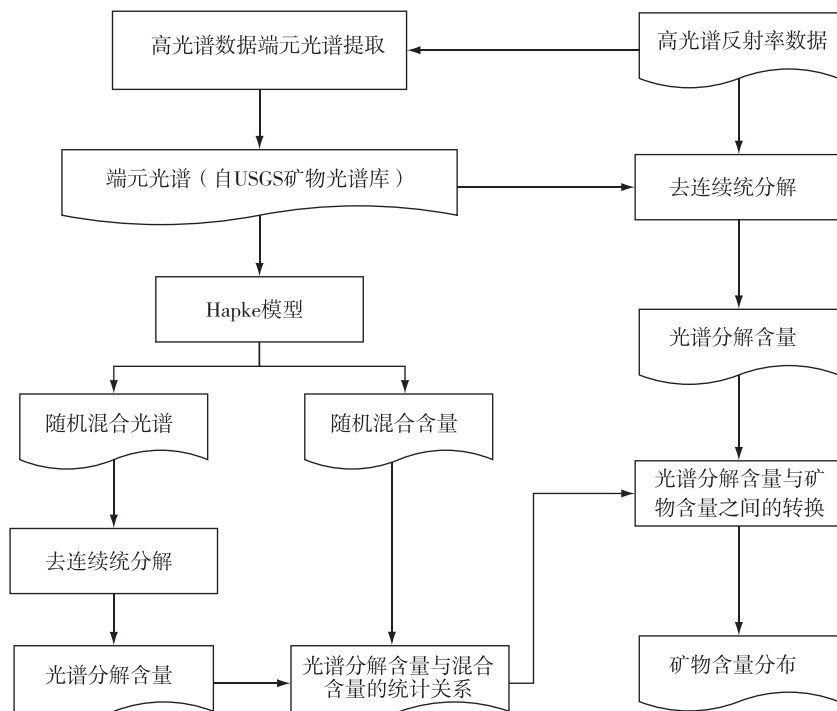


图14 高光谱矿物丰度反演方法流程

Fig. 14 Process of hyperspectral mineral abundance inversion

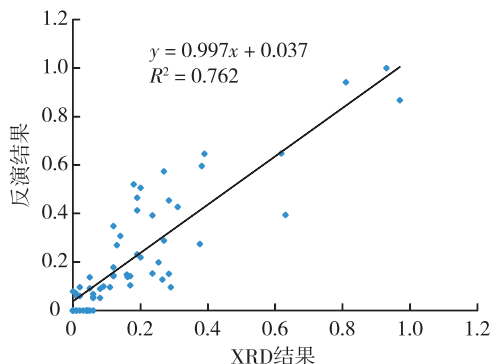


图 15 地开石反演含量与 XRD 测试结果散点图

Fig. 15 Dickite inversion content and XRD test result

4 信息产品验证

4.1 光谱重建产品验证

光谱重建产品验证一般通过对图像和实地同一位置的地物特征光谱波长进行比较,来评价图像光谱的失真度,通常选择具有特征光谱吸收峰的矿物为对象.该方法对地物选择要求较高,需要地形平坦、物质成分均一、波谱特征稳定,且面积较大(不得小于 5×5 个像元)的地方.以可见-短波红外光谱为例,检测的方法是:将具有特征光谱的已知点上影像的反射光谱特征吸收峰波长位置与该点地面实测光谱的特征吸收峰波长位置逐个进行比对,分析影像光谱相对于地面光谱的特征吸收峰波长位置偏移量.由于地面光谱仪的光谱

分辨率可达到 $1\sim 2$ nm,因此在分析偏移量时要根据成像光谱仪光谱分辨率和谱带宽特点,判断其是否在一个合理的光谱区间.如偏移量在一个合理的光谱区间内,则图像光谱代表了实际地物的光谱特征;如差异性较大,则需重新进行辐射校正等一系列的处理.

4.2 遥感地质产品验证

对由经过验证的反射率/发射率数据获得的地学信息产品的检验,主要验证方法有影像光谱检查、实地对应点光谱检查、实地对应点样品的 X 射线衍射分析(XRD)、扫描电子显微镜(包括元素分析)、矿物化学数据的电子显微镜分析等.根据验证目的不同,方法有所不同.针对矿物种类识别信息的验证,以影像光谱验证和野外实地光谱对比验证为主;针对矿物含量的验证除室内光谱和野外实地光谱对比验证外,能结合对应点样品的 X 射线衍射分析(XRD)最佳;矿物精细成分信息、结构信息验证除光谱验证外,多以样品测试分析为主.

矿物含量一般用特征吸收位置的深度来反映.Cudahy 等^[18]以 2200 nm 吸收特征的深度来表示 Al-粘土的含量,通过对机载 HyMap 反射率数据 4 次拟合多项式计算了 Al-粘土(包括高岭土、白云母和 Al-蒙皂石矿物族)的含量.将图像上 33 个验证点的 $2200D$ (2200 nm 处的吸收深度值)与野外同点 ASD 光谱的 $2200D$ 对比,结果显示两者具有很高的相关性(图 16).

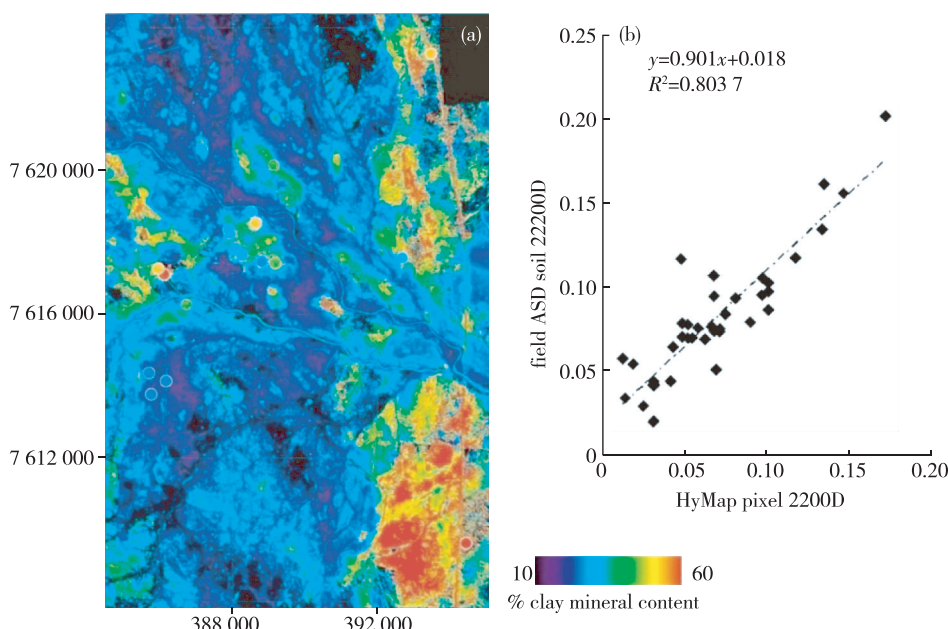
图 16 (a) Al-粘土含量分布图;(b) HyMap 光谱 2200D 与地面同点 ASD 光谱 2200D 散点图^[18]

Fig. 16 (a) Al-clay content map of the Tick Hill area, derived from HyMap reflectance data together with field ASD spectra of soil samples from 33 sites (coloured circles).(b) Scattergram for the predicted AL-clay based on the depth of the 2200 nm absorption feature (2200D) from the HyMap ROI's versus the soil sample spectral data from the same area/site

Doublier 等^[19]对采自法国南部 Montagne Noire 地区不同变质条件下的 41 件样品用 SWIR 光谱(光谱分辨率约 8 nm)建立了 4 种绿泥石光谱指数(CSI(H_2O)、CSI(H_2O)_{sum}、CSI(2250) 和 CSI_{sum}) ,并将其与由样品 XRD 测试结果建立的 Kubler 指数(KI)^[20]进行对比分析.结果显示,全部 41 个样品的 $R^2 = 0.545\sim0.674$ (图 17),排除由 ÁI^[21]和 KI 方法得出不同变质级别的 5 个样品(图 17,灰色符号)后,其相关性也大大提高($R^2 = 0.704\sim0.769$).采用样品内部方差法对所有绿泥石光谱参数的可再现性进行检验,样品内部方差^[22]介于 3.34% (CSI(2250)) ~ 2.31% (CSI(H_2O)_{sum}) 之间,表明所有参数都具有良好的可再现性.

5 应用研究

5.1 区域性矿产资源调查

初步总结了一套“矿物—蚀变异常—找矿蚀变异常”的 2 级信息筛选找矿预测方法.为了更好地服务地质调查工作,聚焦地质调查与找矿预测需求,本工作结合高光谱遥感技术特征,总结出了一套高光

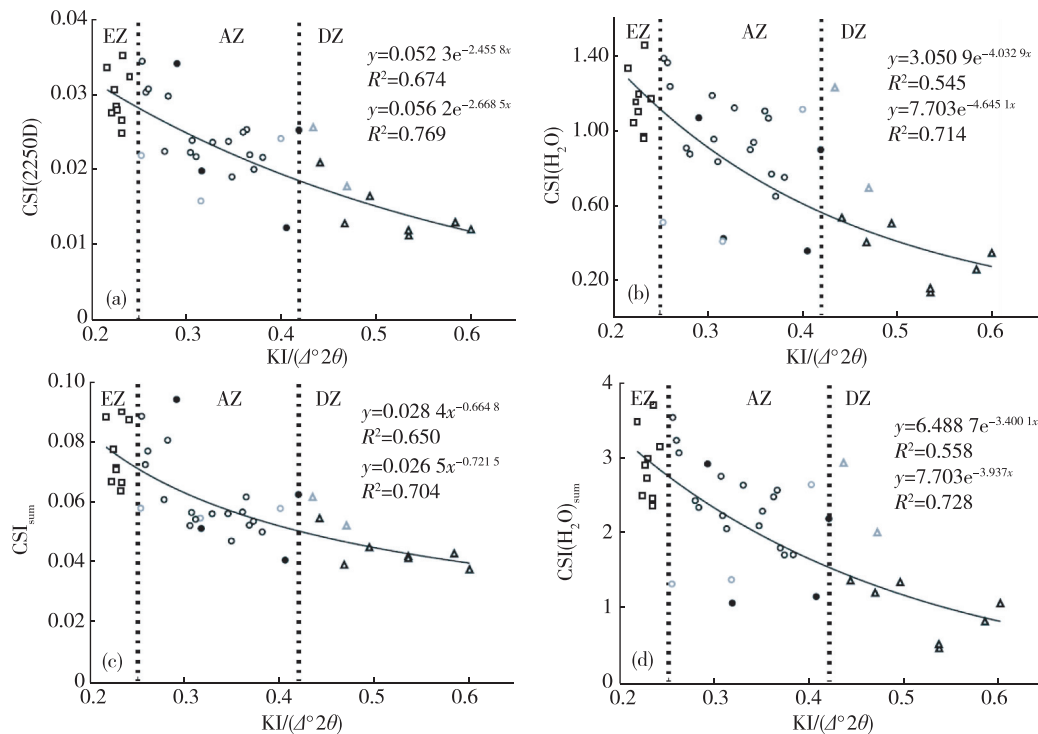
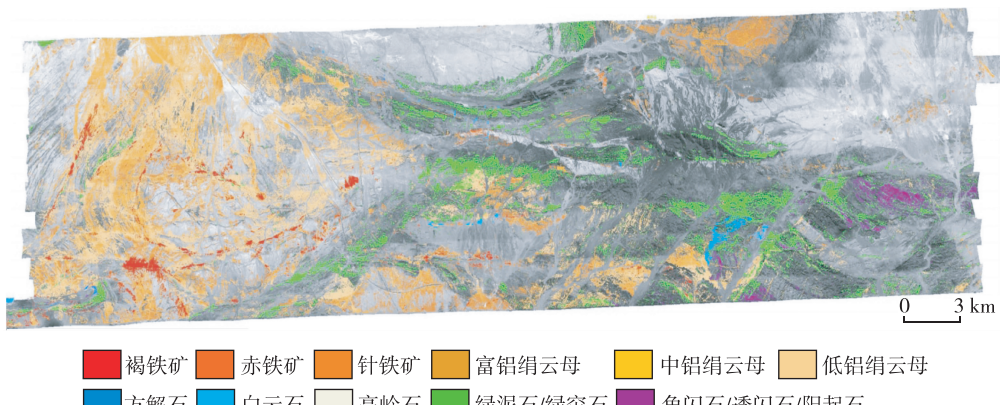
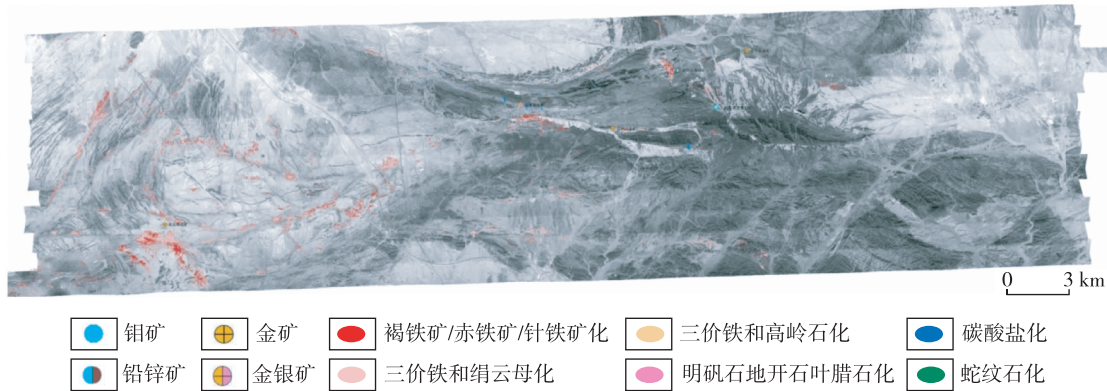


图 17 绿泥石光谱指数 CSI 与 KI 指数关系(EZ、AZ、DZ 分别为浅变质带、近变质带、成岩带)^[19]

Fig. 17 Correlation between CSI and KI (in $\Delta^{\circ} 2\theta$). (a) reflectance 2250D index, (b) reflectance 2250D/1900D index, (c) reflectance 2350D+2250D×1.7 index, and (d) reflectance (2350D+2250D×1.7)/1900D index. Samples are coded according to KI: EZ—epizone, AZ—anchizone, DZ—diagenetic zone. For the five samples in grey XRD based ÁI and KI indicate different metamorphic conditions. The grey formula represents the correlation without these five samples^[19]

Fig. 18 The mineral distribution map of aero CASI_SASI hyperspectral remote sensing^[23]Fig. 19 The alteration anomaly distribution map of aero CASI_SASI hyperspectral remote sensing^[23]

量的地表组合样品的金品位为 0.14~1.04 g/t;1 处矽卡岩型预测区内 Au 品位为 0.32~1.74 g/t.此外,在 2014 年甘肃祁连山调查区内,除发现多处沉积变质型铁矿外,还发现 1 处 Au 矿点,通过地表连续采样化学分析,认为有进一步进行地面勘查工程控制的必要,这也为该地区除寻找铁铜矿外,提供了新的找矿方向.

5.2 成矿地质环境分析

成矿地质环境分析是根据矿物种类、组成、类质同像替换信息对温度、压力、酸碱度等成矿条件进行推断分析.在热液成矿系统中,不同的蚀变矿物组合对应着一定的温压条件和 pH 值范围(表 4、图 21).常见的蚀变组合有泥化、高级泥化、绢英岩化、青磐岩化、外/次青磐岩化、钾化及矽卡岩化.泥化蚀变矿物形成于热液系统冷却退化的低温(<250 °C)阶段^[24],或外生流体混入程度增加的环境,在中低 pH

(大约 4~5)、相对低温(<200~250 °C)条件下,以低温高岭石和蒙脱石为主,含少量的伊利石组矿物;高级泥化反映较强的酸性环境,形成于低 pH(≤4)条件,发育有石英、高温粘土(如地开石或叶腊石)、水铝石及明矾石等矿物,明矾石含量越高,酸性越强.绢英岩化形成于与泥化蚀变相似的 pH 范围和较高温度(>200~250 °C)条件,酸性流体致使长石类矿物发生水解,以绢云母/云母出现为特征,可含少量石英、绿泥石等矿物^[25].青磐岩化形成于近中性到碱性条件,为循环对流的大气水流体与围岩反应发生弱氢交代,以绿泥石/绿帘石的出现为特征,次生角闪石(一般为阳起石)一般出现在高温条件(>280~300 °C),是内青磐岩化蚀变特征.在相对低温条件(<200~250 °C)沸石替代绿帘石而占主导,被称为外/次青磐岩化^[25].钾化一般形成于中性到碱性,高温(一般为 500~600 °C)条件,由高温流体的钾质交代与水解作用形成,以黑云母或钾长石出现为特征.



图 20 航空 CASI_SASI 高光谱遥感找矿预测^[23]

Fig. 20 The prospecting prediction map of aero CASI_SASI hyperspectral remote sensing^[23]

表 4 成矿环境与矿物组成的关系

Table 4 Relationship between metallogenic environment and minerals composition

矿物信息	成矿环境
矿物组合 见图 21	
矿物成分 绢云母/伊利石: 四面体位 Al/Si 以及八面体位 Al/(Fe + Mg) 等类质替换	1) 主要受流体温度、压力、pH 值影响; 2) 在造山型金矿环境下, 温度是主要影响因素, 温度越高越富 Si; 3) 在斑岩型、浅成低温热液等岩浆流体中, 温度、pH 值是主要影响因素, 温度越高越富 Si, pH 值影响相反; 4) 在变质矿床环境中, 温度、压力是主要影响因素, 温度、压力越高越富 Si
明矾石: K/Na 类质替换	1) 主要受流体温度影响; 2) 温度越高越富 Na
绿泥石: Fe/Mg 类质替换	1) 主要受流体温度影响; 2) 温度越高越富 Mg
矿物结构 高岭石/地开石结晶度	1) 结晶度越好, 形成温度越高; 2) 原地型高岭石/地开石的结晶度高于搬运型

矽卡岩化出现于与钾化相似条件, 当同富钙质围岩接触发生汽水热液交代作用, 形成钙石榴石、单斜辉石和透闪石等钙硅酸盐矿物^[25-26].

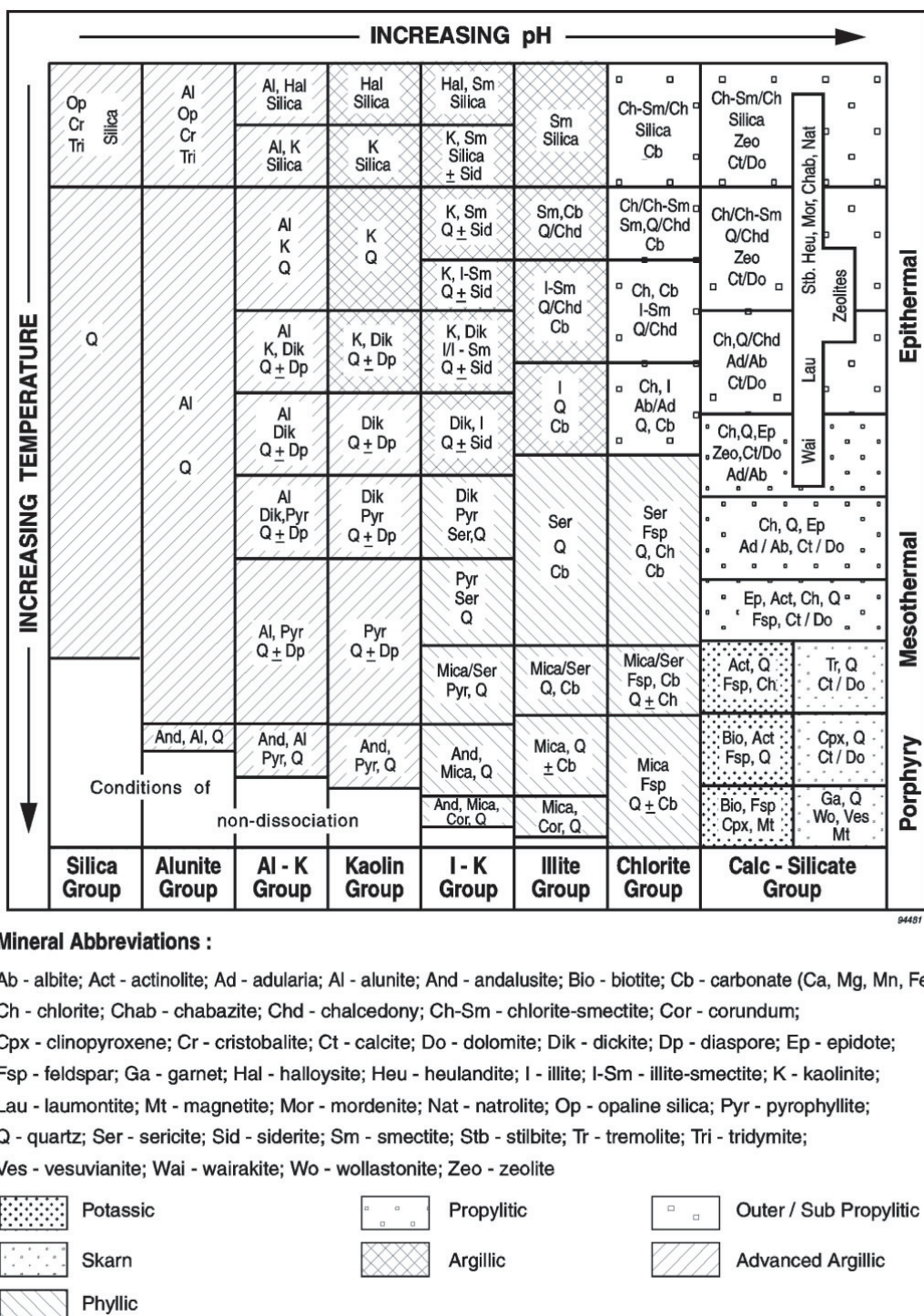
通过矿物的类质同像分析, 可推测其形成时的物理化学条件, 为成矿地质环境分析提供指示信息。如绢云母受四面体位 Al/Si 以及八面体位 Al/(Fe + Mg) 等类质替换影响, 其特征吸收位置在 2 195 ~ 2 225 nm 之间变化, 向长波方向, Al 含量减少; 明矾石的 K/Na 类质替换主要表现在 1 480 nm 处吸收位置的变化, 向长波方向, Na 含量增加, 反之, K 含量增加; 绿泥石的 Fe/Mg 类质替换主要表现在 2 246 ~ 2 262 nm 变化, 向长波方向, Fe 含量增加, 反之, Mg 含量增加。绢云母的类质同像主要受流体温度、压力、pH 值影响, 但是在不同的地质背景中, 三者对其影响权重有所不同。明矾石的类质同像主要受温度

影响, 温度越高越富 Na。绿泥石的 Fe/Mg 类质替换同样主要受流体温度影响, 温度越高越富 Mg。

另外通过矿物光谱的精细特征变化, 还可对矿物的晶体结构进行分析, 如高岭石结晶度。当高岭石结晶度由高变低时, 次级吸收特征位置由 2 160 nm 向 2 180 nm 漂移, 且吸收深度逐渐变浅。高岭石结晶度一般受形成温度影响, 温度越高, 结晶度越好。

5.3 矿山环境监测

矿山的开采、选冶、尾矿库、矿渣堆放等, 均可被酸溶出含重金属离子的矿山酸性废水, 随着矿山排水和降雨使之带入水环境(如河流等)或直接进入土壤, 造成土壤、水体、植被等重金属污染和 pH 值变化。目前针对矿山环境监测主要有矿区次生矿物识别、利用次生矿物或水体对 pH 值估算、对土壤等重

图 21 热液系统中常见的蚀变矿物^[25]Fig. 21 Common alteration minerals in the hydrothermal system^[25]

金属成分含量反演、矿区污染植被信息提取等,以及在此基础上的矿山环境动态变化监测。

矿山活动中,在不同的环境条件下,会产生一系列次生矿物或矿物组合。对次生矿物识别可对其进行的地球化学条件和演化规律进行指示,进而对矿

山环境进行评估^[27-28]。不同次生矿物,特别是含铁矿物的生成对应着一定的 pH 值范围^[29-30]。Kopačková 等^[31]在对捷克 Sokolov 褐煤矿山 pH 环境研究中,发现当 pH<3.0 时有黄铁矿、黄钾铁矾或褐煤等存在,无论是单独存在,还是混合分布;当黄钾铁矾与针铁

矿伴生时,pH 值升高(3.0~6.5);而在针铁矿单独存在时,pH 值为中性或较高(>6.5).以多范围光谱特征拟合(Multi Range Spectral Feature Fitting, MRS-FF)技术,对上述矿物进行了识别和填图,并据此对矿区及外围地表 pH 值进行了估算(图 22).甘甫平等^[32]在江西德兴铜矿区利用水体在 600 nm 附近的光谱吸收特征差异,区分出了尾矿区水体中的酸性水、碱性水和中性水(图 23).

目前主要以矿区水系沉积物、土壤等地物中的重金属成分含量与地面反射光谱特征参量之间建立统计模型来反演重金属含量^[33-34],该方法在不同的矿区环境中特征参数也不尽相同.利用光谱技术开

展重金属成分含量反演大多还处于探索研究阶段,进一步的研究工作仍有待深入.

植被的长势理化特征,如植被光谱特征"红移"、"蓝移"等主要吸收特征参数的变化等能够很好地反映矿山环境特征^[35-36].但是,由于矿山污染情况复杂,除了研究植被反射率受矿山污染的影响之外,还需研究矿山污染物对植被生长过程的影响机制等问题,了解一年之中植被光谱反射率随着植被生长而出现的动态变化特征,然后再通过遥感异常信息提取技术,可以有效可靠地提取出由矿山不同类型的污染所引起的植被异常^[37].

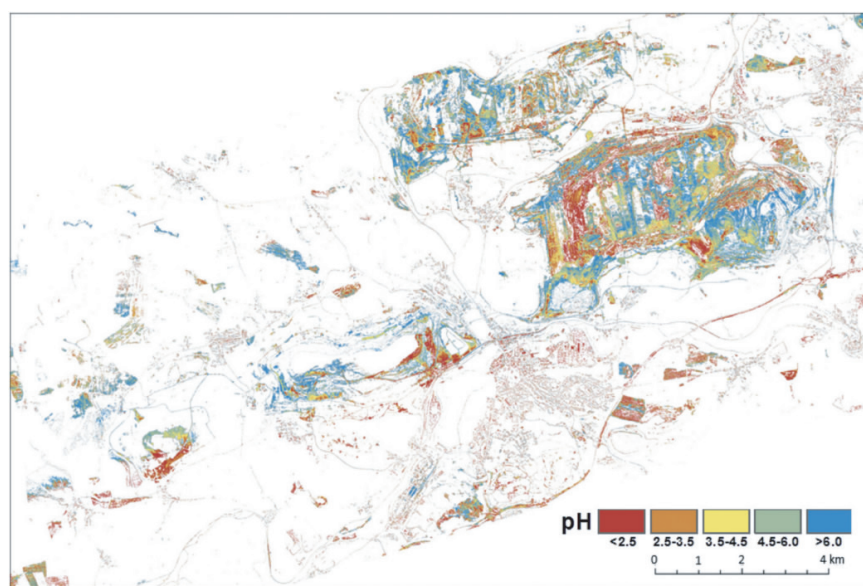


图 22 Sokolov 褐煤盆地 pH 估算值^[31]

Fig. 22 The Sokolov lignite basin: estimated pH^[31]

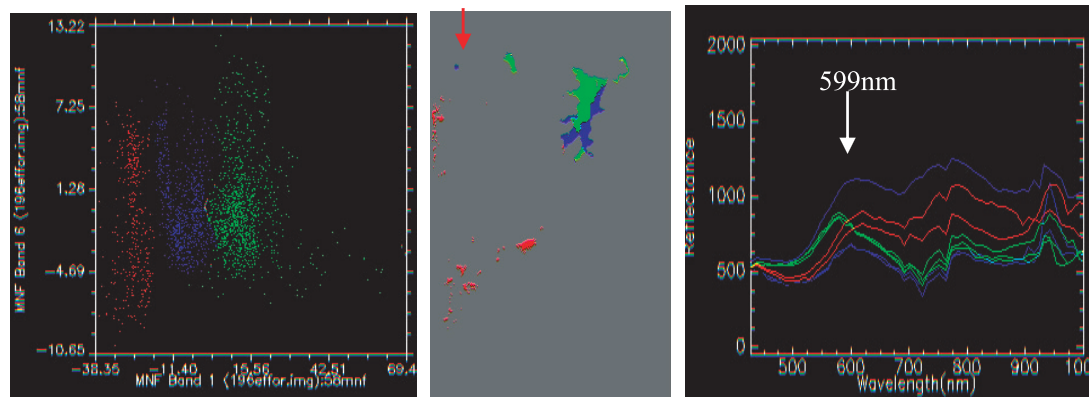


图 23 MNF B1 与 MNF B6 散点图(左)、水体酸碱度信息(中)与水体影像光谱(右)^[32]

Fig. 23 Relative pH information segmenting of water: scatter plot between MNF B1 and MNF B6(left); relative pH for various water (middle), red shows relative low pH, blue shows relative middle pH, and green shows relative high pH; and spectra corresponding to different pH water (right)^[32]

5.4 (成像)光谱矿床三维建模

利用(成像)光谱技术对矿区岩芯进行光谱采集、分析,深入挖掘海量岩芯数据中隐含的矿物信息及示矿信息,已逐渐应用到资源勘查、深部找矿预测工作中^[38].通过岩芯(成像)光谱数据不仅可对矿物识别,还可研究矿物成分与含量.如图 24 所示,根据岩芯光谱扫描仪可快速、准确、无损地识别出岩芯中的蚀变矿物种类及含量.将识别和提取的各钻孔岩芯光谱矿物类型信息、含量信息、矿物光谱特征参数等信息作为基础分析数据,再结合钻孔点位、钻孔编录信息、各测点深度等信息,利用 3D Mine、Vulcan 等三维软件,以主要蚀变带、勘探线为单元,可构建钻孔岩芯光谱矿物信息三维建模(图 25),将不同矿物信息的空间展布特征直观地展示出来.

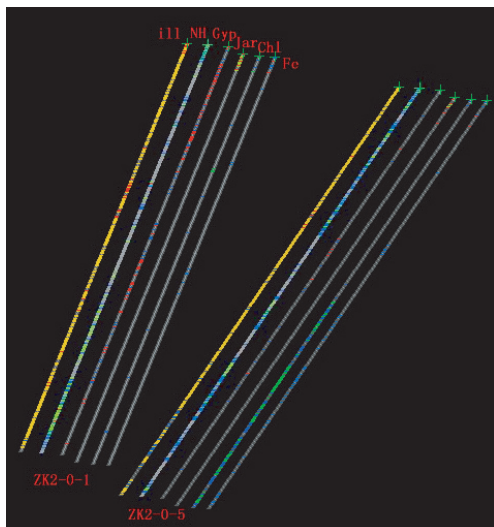


图 24 新疆绿源矿区 2 个钻孔蚀变矿物组合及丰度图
(ill—伊利石; NH—含 NH₄ 矿物; Gyp—石膏;
Jar—黄钾铁矾; Chl—绿泥石; Fe—含铁氧化物)

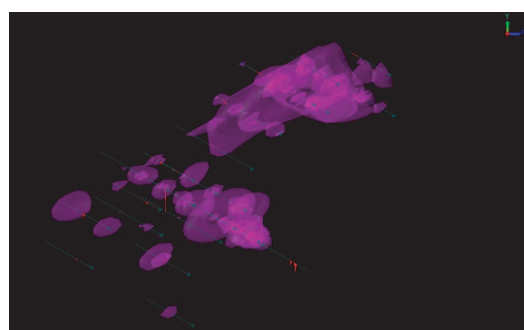
Fig. 24 The alteration mineral assemblage and abundance map of two drill holes (ill—illite; NH—NH₄ bearing minerals; Gyp—Gypsum; Jar—Jarosite; Chl—Chlorite; Fe—iron oxide)

结合矿床地质背景,从三维空间分析其蚀变矿物类型、组合特征和分布规律,为矿床蚀变特征分析、找矿预测提供了重要参考依据.同时矿物成分信息可对成矿环境进行约束,进而为成矿流体物理化学条件、流体运移以及矿床成因机制研究提供科学支撑.

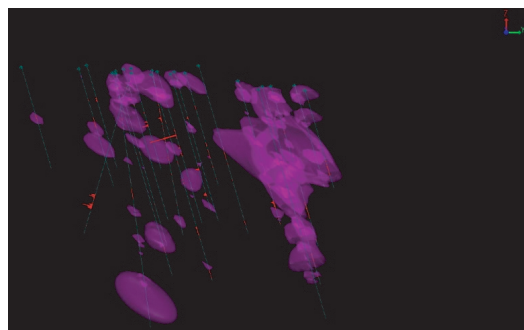
6 讨论

6.1 基础理论与方法

目前的矿物岩石光谱模拟精度已达比较高的程



a.XY方向



b.YZ方向

图 25 新疆绿源矿区含 NH₄ 蚀变矿物丰度三维分布

Fig. 25 The 3-D distribution maps of NH₄ bearing minerals abundances in XY direction (above) and YZ direction (below)

度,模拟精度可能不再是需要关注的主要问题,实现全光谱段的模拟,融合地形、大气、传感器噪声的全链路模拟以及应用是发展方向.最重要的潜在应用方向可能是传感器技术指标的优化设计.

对矿物光谱的认识,特别是光谱特征的指派主要 20 世纪 80 年代总结的成果^[39],这也是目前高光谱地质遥感的主要理论基础.但随着遥感技术定量化、精细化的不断发展,对矿物光谱认识的精度程度、全面程度需要进一步的提升,主要表现在 3 个方面:一是矿物光谱特征的成因指派方法未得到应有的重视,未形成系统的测试、分析方法;二是矿物的类质同像等微观成分与结构对光谱的影响认识还不够全面;三是中红外、热红外谱段光谱特征的指派有待突破.

光谱仪技术指标的优化设计是应用的基础,关键是指派方法的优化设计,根据需求、探测对象特性,合理优化谱段组合、光谱分辨率、空间分辨率、信噪比、幅宽指标,使其综合性能最大化.严密可行的优化设计技术有待形成.

辐射定标与辐射校正仪器研制、数据预处理的难点,尤其是机上、星上定标,定标源包括太阳、月球、定标场、人工光源.从光路的完整讲,包括全光谱

与半光路定标.辐射定标方案多样,到底如何更精确跟踪遥感器在室内、运输、发射、运行过程中的辐射特性变化并加以校正仍需进一步明确.

6.2 数据处理与信息提取技术

目前的辐射传输模型法在可见-短波红外谱段,在大气条件好、地形平坦的地区应用效果很好,但面向全球应用的效果评价方法改进仍有待深入.

信息提取主要分为光谱特征参量、光谱匹配度2大类,二者各有优缺点,在实现高精度、自动化、高效率时表现均不能令人满意.以分层谱系的理念为基础,综合光谱特征增强匹配算法和特征参量,开发提取软件,可能是较好的解决方案.此外,光谱遥感与影像遥感采用的信息提取技术相差很大,互无借鉴,充分融合机器学习算法与光谱识别算法研究成果,可能是形成高度自动化、可支撑业务化与大区域应用的遥感信息提取、识别、分类、变化检测技术体系的关键.

理想情况下,对所有产品都应作定量误差分析,但受混合像元、野外实地采样点的代表性的影晌,目前验证多为定性或半定量验证.

6.3 应用研究

在成矿环境分析应用方面难度较大,应加强研究.但其应用尺度、研究对象、方法与区域性找矿预测完全不同,不可简单套用.光谱在成矿环境分析应用中,隐含一个基本的地质前提条件,就是研究的对象必须是一个(接近)独立、封闭的成矿系统,岩芯光谱扫描技术可发挥更大作用.

矿区次生矿物识别和矿区及外围土壤、水体、植被等目标中重金属反演是矿山开发活动、矿山环境监测的重要技术手段,但多处于探索研究阶段,进一步的研究工作仍有待深入,技术体系有待建立.主要表现在2个方面:1)不同矿区次生矿物种类及其成因认识还不全面,相应矿物光谱库不够完善;2)矿区及外围土壤等目标中重金属在光谱上的响应机制仍不是很清晰,基于统计方法建立的地面光谱与重金属之间的部分统计关系,由于样本数量不足,其可靠性缺乏一定的说服力,影响了技术的进一步推广应用.

(成像)光谱矿床三维建模与传统的地质三维建模有所不同,依据的是识别出的矿物信息,而非传统的地质体,其空间展布特征、发育情况相对地质体要复杂得多,因此需要对传统的三维建模思路进一步改进和完善,使(成像)光谱矿床三维建模更符合

实际地质情况.

另外,盐渍化类型识别、土地沙化半定量提取可能也是发挥光谱优势的应用领域.土地质量监测需求与发展潜力很大,目前的研究几乎完全是基于各种统计算法,以特定样品为对象进行的反演试验,其效果、可靠性、推广性、重现性、可对比性等方面在支撑业务化应用上还有差距,需要进一步深入研究.

7 结论

成像光谱遥感在信息提取、区域性找矿预测方面得到了快速发展,取得很好的应用效果.但在光谱仪技术指标的优化设计、辐射定标上,需要与应用更好的结合,为应用提供综合性能指标最高的、“最好用”的数据源.信息提取软件有待开发,应对大区域,甚至全球化的数据处理,才能发挥光谱遥感兼具宏观、快速、精细的优势.促进光谱遥感与影像遥感技术的融合,改变各自为战的局面,可能是成像光谱遥感面临的最大问题,也是光学遥感面临的最大问题.

参考文献

References

- [1] Vane G, Goetz A F H. Terrestrial imaging spectrometry: Current status, future trends [J]. Remote Sensing of Environment, 1993, 44(2/3) : 117-126
- [2] Hapke B. Theory of reflectance and emittance spectroscopy [M]. New York: Cambridge University Press, 2005
- [3] 赵哲,周萍,闫柏琨,等.基于Hapke辐射传输模型的月壤光谱模拟 [J].地学前缘,2015,23(3) : 1-13
ZHAO Zhe, ZHOU Ping, YAN Bokun, et al. Spectra simulation of lunar regolith based on the Hapke radiative transfer model [J]. Earth Science Frontiers, 2015, 23(3) : 1-13
- [4] Gao B C, Montes M J, Davis C O, et al. Atmospheric correction algorithms for hyperspectral remote sensing data of land and ocean [J]. Remote Sensing of Environment, 2009, 113(9) : S17-S24
- [5] Cui J, Yan B K, Wang R S, et al. Regional-scale mineral mapping using ASTER VNIR/SWIR data and validation of reflectance and mineral map products using airborne hyperspectral CASI/SASI data [J]. International Journal of Applied Earth Observation and Geoinformation, 2014, 33(1) : 127-141
- [6] Qu Z, Kindel B C, Goetz A F H. The high accuracy atmospheric correction for hyperspectral data (HATCH) model [J]. IEEE Transactions on Geoscience and Remote Sensing, 2003, 41(6) : 1223-1231
- [7] Wan Z M, Li Z L. A physics-based algorithm for retrieving land-surface emissivity and temperature from EOS/MODIS data [J]. IEEE Transactions on Geoscience and Remote Sensing, 1997, 35(4) : 980-996

- [8] Cui J, Yan B K, Dong X F, et al. Temperature and emissivity separation and mineral mapping based on airborne TASI hyperspectral thermal infrared data [J]. International Journal of Applied Earth Observation and Geoinformation, 2015, 40: 19-28
- [9] Vaughan R G, Calvin W M, Taranki J V. SEBASS hyperspectral thermal infrared data; Surface emissivity measurement and mineral mapping [J]. Remote Sensing of Environment, 2003, 85(1): 48-63
- [10] Gillespie A R, Rokugawa S, Matsunaga T, et al. A temperature and emissivity separation algorithm for Advanced Spaceborne Thermal Emission and Reflection Radiometer (ASTER) images [J]. IEEE Transactions on Geoscience and Remote Sensing, 1998, 36 (4): 1113-1126
- [11] Fenstermaker L K, Miller J R. Identification of fluvially redistribute mill tailings using high spectral resolution aircraft data [J]. Photogrammetric Engineering & Remote Sensing, 1994, 60(8): 989-995
- [12] Yuhas R H, Geotz F H A, Boardman J W. Descrimination among semi-arid landscape endmembers using the Spectral Angle Mapper (SAM) algorithm [C] // Summaries of the Third Annual JPL Airborne Geoscience Workshop, 1992: 147-149
- [13] Chang C I. An information-theoretic approach to spectral variability, similarity, and discrimination for hyperspectral image [J]. IEEE Transactions on Information Theory, 2000, 46(5): 1927-1932
- [14] Van der Meer F. The effectiveness of spectral similarity measures for the analysis of hyperspectral imagery [J]. International Journal of Applied Earth Observation and Geoinformation, 2006, 8(1): 3-17
- [15] 王润生, 杨苏明, 闫柏琨. 成像光谱矿物识别方法与识别模型评述 [J]. 国土资源遥感, 2007, 19(1): 1-9
WANG Runsheng, YANG Suming, YAN Bokun. A review of mineral spectral identification methods and models with imaging spectrometer [J]. Remote Sensing for Land & Resources, 2007, 19(1): 1-9
- [16] Clark R N, King T V V, Klejwa M, et al. High spectral resolution reflectance spectroscopy of minerals [J]. Journal of Geophysical Research, 1990, 95 (B8): 12653-12680
- [17] 甘甫平, 王润生, 马蔚乃. 基于特征谱带的高光谱遥感矿物谱系识别 [J]. 地学前缘, 2003, 10(2): 445-454
GAN Fuping, WANG Runsheng, MA Ainai. Spectral identification tree (SIT) for mineral extraction based on spectral characteristics of minerals [J]. Earth Science Frontiers, 2003, 10(2): 445-454
- [18] Cudahy T, Jones M, Thomas M, et al. Next generation mineral mapping: Queensland airborne HyMap and satellite ASTER surveys 2006–2008 [R]. CSIRO report P2007/364, 2008, DOI: 10.13140/RG.2.1.2828.1844
- [19] Doublier M P, Roache T, Potel S, et al. Short-wavelength infrared spectroscopy of chlorite can be used to determine very low metamorphic grades [J]. European Journal of Mineralogy, 2012, 24(24): 891-902
- [20] Guggenheim S, Bain D C, Bergaya F, et al. Report of the Association Internationale pour l'Étude Des Argiles (AIPEA) nomenclature committee for 2001: Order, disorder and crystallinity in phyllosilicates and the use of the "crystallinity index" [J]. Clays and Clay Minerals, 2002, 50(3): 406-409
- [21] Árkai P. Chlorite crystallinity: An empirical approach and correlation with illite crystallinity, coal rank and mineral facies as exemplified by Palaeozoic and Mesozoic rocks of northeast Hungary [J]. Journal of Metamorphic Geology, 1991, 9(6): 723-734
- [22] Robinson D, Warr L N, Bevins R E. The illite "crystallinity" technique: A critical appraisal of its precision [J]. Journal of Metamorphic Geology, 1990, 8: 333-344
- [23] 闫柏琨, 董新丰, 王喆, 等. 航空高光谱遥感矿物信息提取技术及其应用进展:以中国西部成矿带调查为例 [J]. 中国地质调查, 2016, 3(4): 55-62
YAN Bokun, DONG Xinfeng, WANG Zhe, et al. Mineral information extraction technology by airborne hyperspectral remote sensing and its application progress: An example of mineralization belts of western China [J]. Geological Survey of China, 2016, 3(4): 55-62
- [24] Fournier R O. Hydrothermal processes related to movement of fluid from plastic into brittle rock in the magmatic-epithermal environment [J]. Economic Geology and the Bulletin of the Society of Economic Geologists, 1999, 94(8): 1193-1211
- [25] Corbett G J, Leach T M. Southwest Pacific Rim gold-copper systems: Structure, alteration and mineralization [M]. Special Publications of Society of Economic Geologist, 1998: 1-236
- [26] Tosdal R M, Dilles J H, Cooke D R. From source to sinks in auriferous magmatic-hydrothermal porphyry and epithermal deposits [J]. Elements, 2009, 5(5): 289-295
- [27] Riaza A, Ong B C, Müller C A. Dehydration and oxidation of pyrite mud and potential acid mine drainage using hyperspectral DAIS 7915 data (Aznalcóllar, Spain) [C] // The International Archives of the Photogrammetry, Remote Sensing and Spatial Information Sciences, 2006, 34, Part XXX
- [28] Shang J L, Morris B, Howarth P, et al. Mapping mine tailing surface mineralogy using hyperspectral remote sensing [J]. Canadian Journal of Remote Sensing, 2009, 35 (sup 1): 126-141
- [29] Jónssøn J. Phase transformation and surface chemistry of secondary iron minerals formed from acid mine drainage [D]. Swedish: Ume University, 2003
- [30] Bigham J M, Schwertmann U, Pfaff G. Influence of pH on mineral speciation in a bioreactor simulating acid mine drainage [J]. Applied Geochemistry, 1996, 11 (6): 845-849
- [31] Kopačková V. Using multiple spectral feature analysis for quantitative pH mapping in a mining environment [J]. International Journal of Applied Earth Observation and Geoinformation, 2014, 28(1): 28-42
- [32] 甘甫平, 刘圣伟, 周强. 德兴铜矿矿山污染高光谱遥感直接识别研究 [J]. 地球科学-中国地质大学学报, 2004, 29(1): 119-126
GAN Fuping, LIU Shengwei, ZHOU Qiang. Identification of mining pollution using hyperion data at Dexing copper

- mine in Jiangxi province, China [J]. Earth Science-Journal of China University of Geosciences, 2004, 29 (1) :119-126
- [33] Choe E, van der Meer F, van Ruitenbeek F, et al. Mapping of heavy metal pollution in stream sediments using combined geochemistry, field spectroscopy, and hyperspectral remote sensing: A case study of the Rodalquilar mining area, SE Spain[J].Remote Sensing of Environment, 2008, 112(7) :3222-3233
- [34] Kemper T, Sommer S. Estimate of heavy metal contamination in soils after a mining accident using reflectance spectroscopy [J]. Environmental Science and Technology, 2002, 36(12) :2742-2747
- [35] 刘圣伟,甘甫平,王润生.用卫星高光谱数据提取德兴铜矿区植被污染信息[J].国土资源遥感, 2004, 16 (1) :6-10
LIU Shengwei, GAN Fuping, WANG Runsheng. The application of hyperion data to extracting contamination information of vegetation in the dexing copper mine, jiangxi province, China [J]. Remote Sensing for Land & Re-
- sources, 2004, 16(1) :6-10
- [36] Noomen M F. Hyperspectral reflectance of vegetation affected by underground hydrocarbon gas seepage[D].Enschede: International Institute for Geo-information Science & Earth Observation, 2007:145
- [37] 李万伦,甘甫平.矿山环境高光谱遥感监测研究进展[J].国土资源遥感, 2016, 28(2) :1-7
LI Wanlun, GAN Fuping. Progress in hyperspectral research and monitoring in mine environment[J].Remote Sensing For Land & Resources, 2016, 28(2) :1-7
- [38] 修连存,郑忠忠,殷靓,等.岩芯扫描仪光谱数据质量评估方法研究[J].光谱学与光谱分析, 2015, 35(8) :2352-2356
XIU Liancun, ZHENG Zhizhong, YIN Liang, et al. Research on assessment methods of spectrum data quality of core scan [J]. Spectroscopy and Spectral Analysis, 2015, 35(8) :2352-2356
- [39] Hunt G R. Spectroscopic properties of rock and minerals [M] // Carmichael R S. Handbook of Physical Properties of Rocks. Boca Raton: CRC Press, 1982:295-385

Research progress of spectrometry geological remote sensing

GAN Fuping^{1,2} DONG Xinfeng^{1,2} YAN Bokun^{1,2} LIANG Shuneng^{1,2}

1 China Aero Geophysical Survey & Remote Sensing Center for Land and Resources, Beijing 100083

2 Key Laboratory of Aero Geophysics and Remote Sensing Geology of China Ministry of Land and Resources, Beijing 100083

Abstract Geological remote sensing is one of the most important application fields that can reflect and exploit the characteristics and advantages of spectral remote sensing technology. In this paper, the latest research progress of spectrometry geological remote sensing, including spectral simulation and characteristics analysis for minerals and rocks, technical parameter optimization design of spectrometer, radiometric calibration and correction, derivation of surface spectra, information extraction, information product validation and geological application are summarized. On the basis of the above work, the progress, problems and development of the spectrometry geological remote sensing are discussed.

Key words geological remote sensing; ore-prospecting; spectra simulation; information extraction

文章编号:1009-2722(2018)03-0008-07

海洋航空物探数据库建设进展

王林飞,薛典军,李芳,何辉,冯磊,周伟

(中国国土资源航空物探遥感中心,北京 100083)

摘要:本着“不搞重复建设,海陆统筹”的思想设计了航空重力数据库表结构,与航磁总场、航磁梯度、航电、航空伽玛能谱一起建成了统一的航空物探数据库,实现“海陆一张图”的航空物探勘查全过程数据的管理。基于 GeoProbe 平台,采用插件技术和 WebGIS 技术研发数据服务软件,与完善后的数据库数据采集软件、航空物探遥感资料目录服务系统,构成一体化的航空物探数据管理服务体系。采取规范的数据整理流程和严格的数据质量检查措施,入库更新了渤海、黄海等约 3.5 万 km² 的海洋航空重力数据,形成覆盖渤海、黄海、东海、南海南部及海岸带约 497 万 km² 的海洋航空物探数据库,可提供全海域一张图的系列服务产品,从而为基础调查项目的工作部署、数据处理及成果解释、报告编写等工作提供基础资料及成果信息共享和服务。

关键词:航空物探;数据库建设;数据服务;数据共享

中图分类号:G250.74

文献标识码:A

DOI:10.16028/j.1009-2722.2018.03002

日益加强的海洋航空物探调查工作需要强有力的信息技术支持。海洋航空物探调查工作相较陆地虽然起步较晚,但由于国家和社会经济等各方面的旺盛需求,近年来发展迅速。2008 年 7 月 29 日,国务院批准了《海洋地质保障工程总体方案》,其中“海洋基础地质调查工程”中的“海洋航空物探遥感调查与应用”项目积累了大量价值宝贵的海洋航空物探调查与研究数据,这就要求要采用合理的技术来管理和利用这些数据。数据库建设既是上一轮海洋地质调查工作的最后环节,数据共享和服务也是下一轮海洋地质调查研究的开始。

收稿日期:2018-01-08

基金项目:中国地质调查局二级项目(DD20160141);国家重点研发计划“典型覆盖区航空地球物理技术示范与处理解释软件平台开发”所属课题“综合航空地球物理数据处理、解释和管理软件平台研发”(2017YFC0602204)

作者简介:王林飞(1977—),女,博士,高级工程师,主要从事航空物探方法技术研究、软件研发与系统集成和航空物探资料信息化等工作。E-mail:wlf4103@126.com

在海洋航空物探信息服务系统建设时,为了充分利用现有资源,避免重复开发而带来人力、物力、财力的浪费,为贯彻“海陆统筹”的思想,在原航空物探数据库基础上^[1,2],不断补充和完善数据库内容,采用先进的计算机技术和 WebGIS 技术实现海洋航空物探调查及成果数据的科学化、信息化管理和存储^[3],并在此基础上实现“海陆一张图”的信息整合与共享。

1 建立航空物探数据库建设技术标准体系

航空重力勘查是以机载(航空)测量平台,利用航空重力仪、定位仪等组成的航空标量重力测量系统在测量区域开展航空重力测量,获取航空重力场数据和辅助测量数据(如地理坐标数据、高度数据等),并对其进行处理、成图,进行地质解释和矿产资源远景区评价,解决关心的地质问题^[4]。笔者在调研和分析航空重力业务流程和数据流程的基础上,对航空重力数据进行分类,基于 Geoda-

atabase 数据模型, 运用 Case 工具和 UML 构建航空物探数据模型的方法, 经过概念设计、逻辑设计和物理设计^[5], 建立航空重力数据库结构, 使其能

存储不同尺度、海量、有序的航空重力基础数据(图 1)、解释评价数据、图件及文字报告等, 实现航空重力勘查全过程数据的管理。

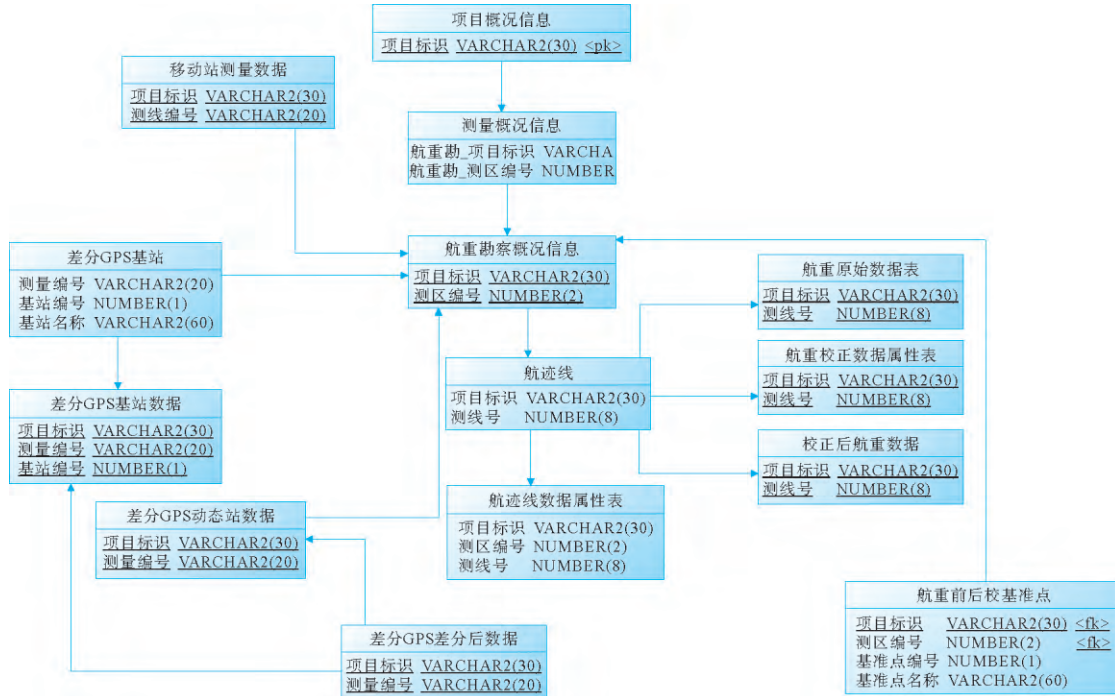


图 1 航空重力基础数据实体关系图

Fig. 1 A flow chart of Airborne gravity basic data

建立的航空重力数据库与航磁总场、航磁梯度、航电、航空伽玛能谱一起构成了统一的航空物探数据库, 其涵盖了航空物探勘查、数据预处理和基本处理、数据解释评价、报告编写以及数据资料管理等过程中的全部有用数据。这些数据涉及到地球物理学、地球物理勘查、区域地质调查、构造地质学、岩石学、海洋地质学、石油及天然气地质学、数学地质、测绘学、电子学等几十个学科。为了使数据库管理的信息标准化, 使用了国家标准“地质矿产术语分类代码”中上百个专业标准; 对国家标准中没有涉及到的一些航空物探特有的信息, 制定了 4 个信息化标准, 建立了航空物探数据库建设所需的技术标准体系, 包括:《航空物探项目管理和资料管理分类代码标准》《航空物探勘查分类代码标准》《航空物探数据要素类和对象类划分标准》《航空物探信息系统元数据标准》《航空物探信息系统数据库数据结构设计》《航空物探信息系统数据库数据检查规则》《航空物探信息系统数

据字典》及《航空物探数据整理与入库工作指南》, 有力地推进了航空物探数据库建设和信息系统开发, 保证了数据质量, 为信息共享与社会化服务奠定了基础。

2 建设海洋航空物探数据库实体

数据库建设的重要工作内容之一就是数据的收集、整理与入库。数据库是航空物探信息系统的基石, 数据质量是数据库的生命。只有拥有正确数据的信息系统, 才能提供良好的服务。因此, 数据库的数据质量控制不仅仅要严把入口关(数据入库), 还必须严把数据源头关(数据整理)。采取规范的数据整理流程, 制定严格数据质量检查措施^[6], 是控制航空物探数据整理的质量, 提高数据库的数据质量的有效方法, 图 2 是目前不同类型的海洋航空物探数据整理、质量检查及入库的大致步骤。

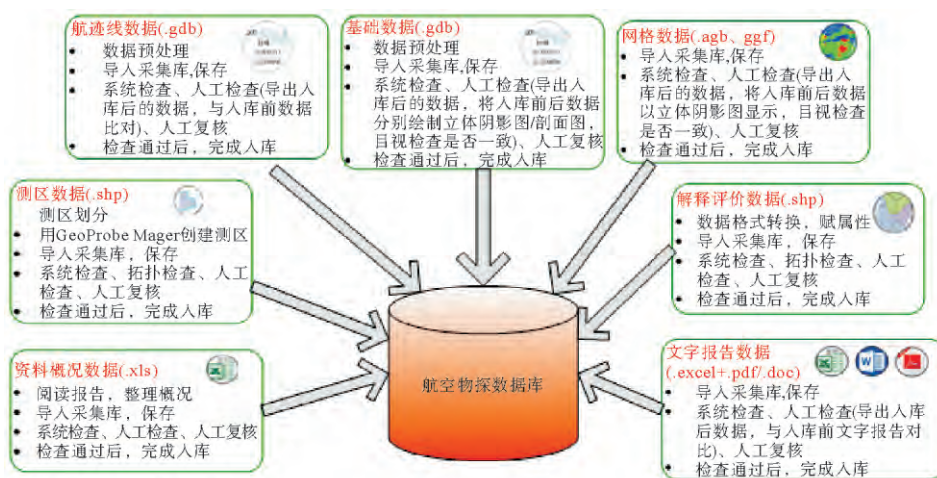


图 2 海洋航空物探数据整理、入库步骤示意图

Fig. 2 Process and storage of marine aerogeophysical data

本着“海陆统筹”的思想,在部署的海洋航空物探信息服务系统上,依据航空物探数据库建设相关标准和技术要求,采用终端机远程登陆服务器,实施数据整理和入库工作。目前,已完成渤海、黄海、东海、南海南部及海岸带约 497 万 km² 的海洋航空物探数据库数据的积累和更新,共 68 个测区,272 万测线千米的航空物探概况、空中收录数据、测区概况数据、重力场数据及成果解释和文字报告等全过程数据,总计约 500 GB,可形成全海域一张图的系列服务产品,图 3 为中国海域航空物探实际材料图。

3 建立一体化的海洋航空物探信息服务系统

根据航空物探的业务需求、数据安全性、易开发、易维护等要求,建立了海洋航空物探信息服务系统(图 4),主要包括面向外部用户的航空物探遥感数据资料查询系统(DCSS),面向内部用户的航空物探基础调查及成果数据的采集软件 AGRS DataCollect 和数据服务软件 GeoProbe DataServer 以及航空物探专业数据处理解释软件 Geo-Probe Mager,从而建立了从“数据处理解释”→“数据采集入库”→“数据服务”→“资料查询”的一体化流程。

3.1 航空物探遥感数据资料查询系统

改进完善B/S架构的航空物探遥感资料查

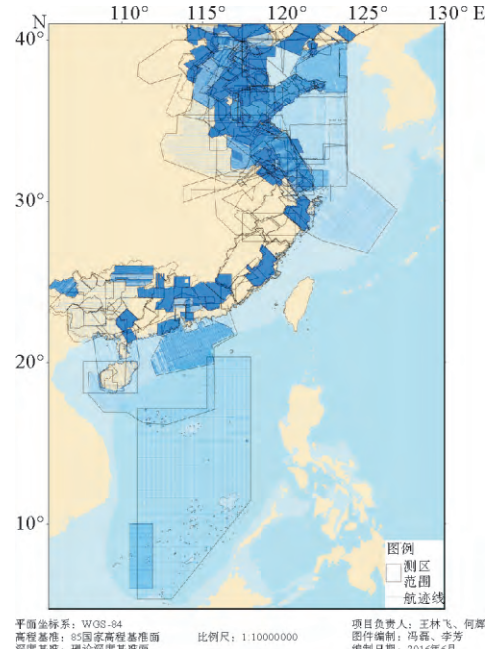


图 3 中国海域航空物探实际材料图

Fig. 3 The aerogeophysical information map of China sea area

询系统(DCSS)(网址:<http://dcss.agrs.cn/>),调整系统界面、优化查询检索功能;并通过数据建模、抽取、展示的方式实现海洋航空物探数据库和资料查询系统的数据衔接,建立数据库系统之间的数据表、数据项的映射关系,进而在 Web 中发布服务。该系统实现了从航空物探勘查科研资料到地形图资料、遥感影像数据、地质图件等 30 余种资料的基于一张图的综合性查询检索、订单服

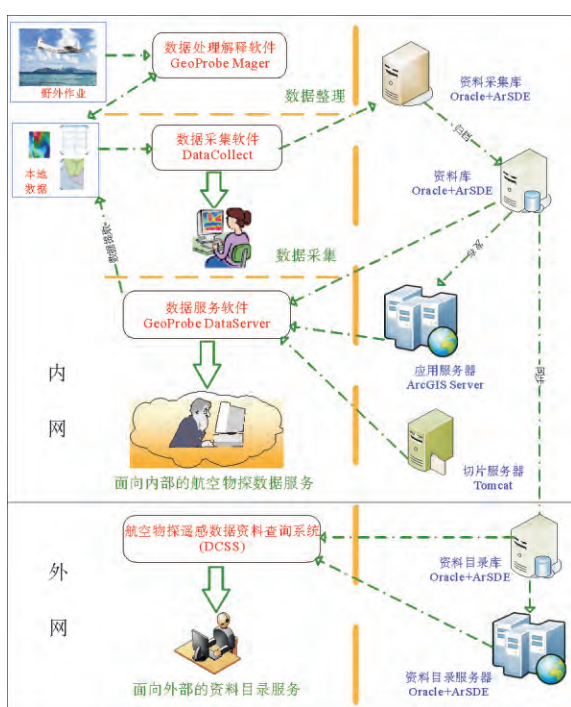


图4 海洋航空物探信息服务系统服务流程

Fig. 4 The service flow chart of Marine aerogeophysical information service system

务功能,可为航遥中心内部用户和部、局、社会用户提供航空物探遥感勘查项目成果元数据、专题产品元数据和基础资料元数据信息的网络查询服务,为航空物探遥感调查成果社会化服务提供了技术支撑和保障(图5)。

3.2 航空物探数据库数据采集软件

在Visual Studio.net 2013开发平台下,采用ArcEnginge10.1组件,升级完善数据库数据采集软件(Agrs DataCollect),可为资料管理人员提供数据录入—导入数据库,入库数据正确性检查,数据查询,数据制图等功能,并且与GeoProbe Mager软件数据处理结果对接,可实现数据的批量导入,从而提高了数据入库效率,保证了入库数据的质量。

数据采集软件采用入库数据正确性检查的规则化方法,解决了不同年代资料信息不齐全的数据入库质量检查问题^[1];在完成数据库结构设计之后,针对每张数据库表中每个字段制定了入库数据正确性的检查规则,建立动态检查规则表,针对不同的检查规则编写检查函数,从数据库中获

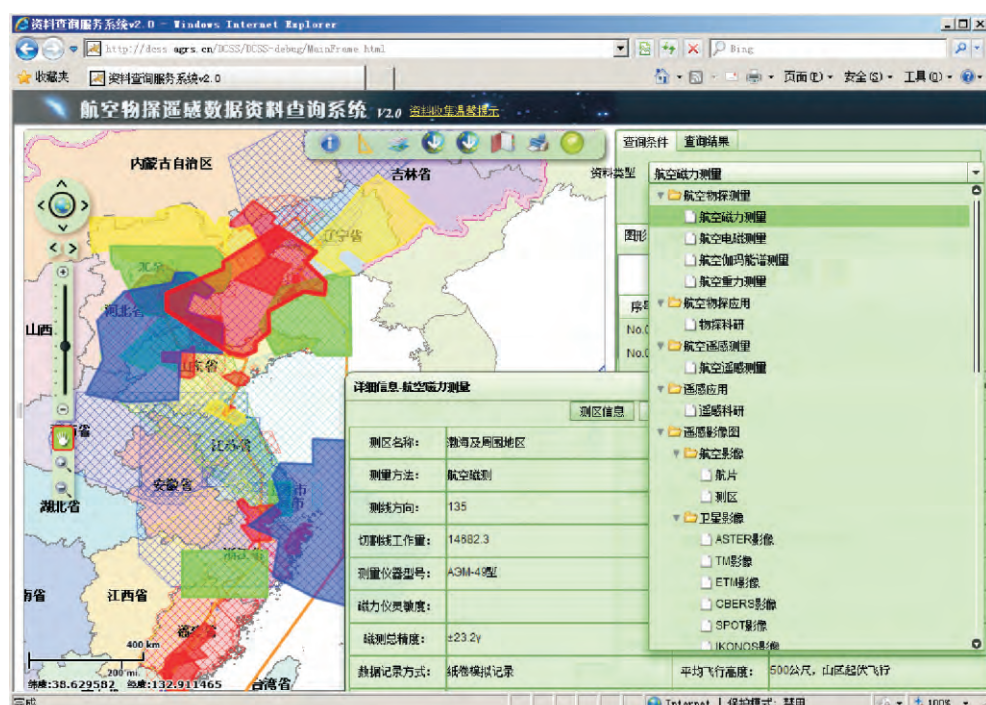


图5 航空物探遥感资料查询系统主界面

Fig. 5 The main interface of Aerogeophysical remote sensing data query system

取被检查表数据库字段的检查规则,对入库数据进行检查。这样比直接对逐个数据库表字段编写检查代码的方法,减少了软件代码开发工作量,且可以根据实际情况直接修改检查规则表,确定数据库字段数据的检查方法,不需要修改软件代码,提高了软件的灵活性和适用性。

3.3 海洋航空物探数据服务软件

研究道格拉斯-普克抽稀算法、地图优化配置和符号化渲染技术等^[3],基于 ArcGIS Server 企业级软件平台以 WFS 等数据流发布航空物探空

间数据;研究基于四叉树的瓦片数据层叠技术,以 WMTS 瓦片服务方式发布图件数据^[7,8]。而后采用 WebGIS 体系结构研发数据服务软件(Geo-Probe DataServer)(图 6,7),即在服务端使用 ArcObjects 来扩展 ArcGIS Server 的基础服务;在客户端基于 GeoProbe 平台采用插件技术^[9,10],调用服务器端的基础服务和扩展服务,实现数据浏览、数据查询等功能插件。GeoProbe 客户端与数据服务端之间的信息传递采用 SOAP(Simple Object Access Protocol)协议^[11],其交互流程大致如下:

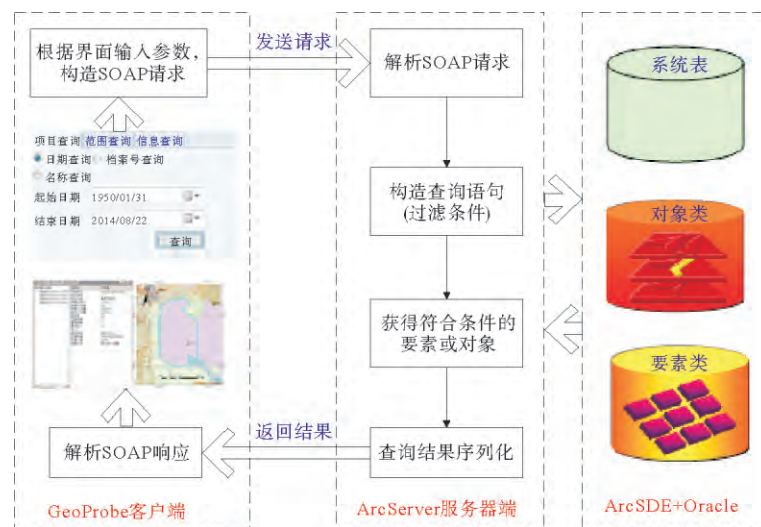


图 6 数据服务软件服务器端与客户端交互流程示意图

Fig. 6 Data service software for interaction between server-side and client

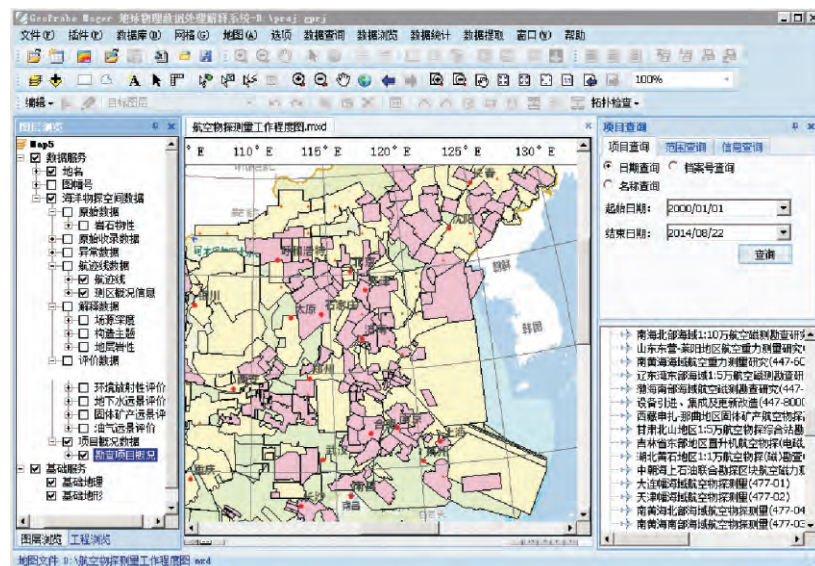


图 7 海洋航空物探数据服务软件主界面

Fig. 7 The main interface of Marine aerogeophysical data service software

(1)GeoProbe 客户端根据功能插件界面输入参数,构造 XML 格式的 SOAP 请求,连接服务器并发送请求。

(2)服务器端接收到请求消息后,调用基础服务和扩展服务功能模块进行业务逻辑处理,即通过解析 SOAP 请求,构造 SQL 语句和空间查询语句,与航空物探数据库交互;然后将查询结果序列化后,以 SOAP 响应消息的形式返回给客户端。

(3)GeoProbe 客户端接收服务端返回的响应消息,并将此 SOAP 响应解析后,在 GeoProbe 平台进行展示。

WebGIS 技术可充分利用所有能够获取的网络资源,将比较复杂的处理工作分配给服务器,而客户端只完成一些相对简单的操作。这种数据的处理模式能够充分发挥服务器及客户端的能力,

提高数据浏览、检索速度。

4 海洋航空物探信息服务系统应用与服务

应用海洋航空物探信息服务系统中的数据库数据采集软件(AGRS DataCollect)累计完成 495 个项目取得的航空物探项目概况数据、空中收录数据、测区概况数据、航空物探基础数据及成果解释和文字报告数据等的质量检查和入库工作。如,通过采集软件可将 GeoProbe Mager 专业软件生成的测区数据(.shp 数据),导入数据库,其中涉及数据唯一性检查、数据类型检查等。如果检查不通过,采集软件给出错误提示信息。采集人员根据错误日志信息(图 8),可纠正数据中存在的错误,再重新导入。

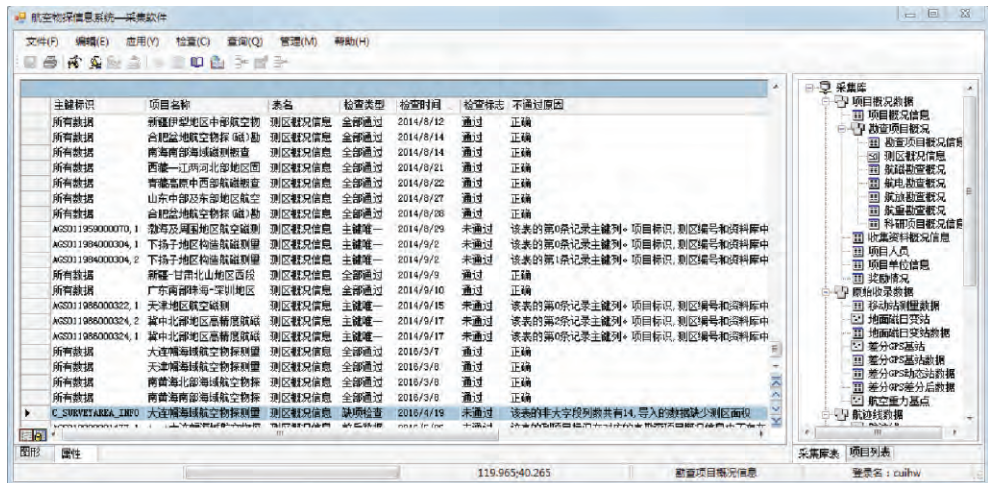


图 8 测区概况数据导入的错误日志信息

Fig. 8 Errors of imported survey area data

航空物探信息服务系统中的数据服务软件 GeoProbe DataServer 为用户提供了快速、便捷的资料查阅方式,包括项目资料快速查询、测区(资料)查询、数据定制浏览及全文检索等。通过上述功能,用户可快速生成整装勘查区、重点成矿区带、中国海域航空物探工作程度图等,为“重要油气盆地和成矿区带航空物探与遥感调查”“海洋基础地质调查”工程等提供航空物探测区工作部署依据;可快速了解测区内的航空物探工作程度及相关地球物理、地质及地理交通位置等情况,为测区的工作开展提供方便;可浏览以往项目在该测

区及周边划分的断裂、圈定的异常、油气远景评价及构造分区等,并可进行可视化叠加分析,为成果解释提供参考;可检索生产、成果报告等,为成果报告的编写提供参考资料;亦可结合其他项目的网格数据开展区域编图等研究。

研发的资料查询服务系统承担着提供社会化服务的角色,在系统上线期间(2012—2015 年),共计向国内 99 家单位(20 余家地调局直属单位以及 70 余家其他地勘单位)发送资料 155 次,其中文字资料 219 份,图件资料 1 921 份,电子介质资料 117 份。

5 结论

项目组本着“边研发、边应用、边完善”的原则，建设海洋航空物探数据库，使其能够存储和管理航磁总场、航磁梯度、航电、航空伽玛能谱、航重相关的原始数据、解释评价数据及成果图件、报告等。研发的海洋航空物探信息服务系统服务于“海洋基础公益性地质调查”计划中的“海洋基础地质调查工程”和“数字海洋地质保障工程”及“基础性公益性地质矿产调查”中的“重要油气盆地和成矿区带航空物探与遥感调查工程”等，为相关项目的工作部署、数据处理、数据编图及成果解释、报告编写等工作提供基础资料、成果信息共享和服务。

参考文献：

- [1] 薛典军,熊盛青,王林飞,等.航空物探信息系统建设[M].北京:地质出版社,2013.
- [2] 王林飞,薛典军,何辉,等.基于 Oracle 的航空物探测量数据存储方案[J].物探与化探,2007,31(6):581-584.
- [3] 王林飞,薛典军,李芳,等.航空物探测量数据共享技术研究与应用[J].物探与化探,2015,39(增刊):152-156.
- [4] 熊盛青,周锡华,郭志宏,等.航空重力勘探理论方法及应用[M].北京:地质出版社,2010.
- [5] 闫红雨,付宗棠,王林飞,等.基于 Case 工具和 UML 的航空物探数据模型的构建[J].物探与化探,2007,31(6):585-587.
- [6] 何辉,王林飞,闫红雨,等.航空物探数据库建设中数据质量控制方法[J].物探与化探,2007,31(6):588-590.
- [7] 张俊丽,李艳明,李欣.WebGIS 地图图片缓存技术研究[J].微计算机信息,2009,25(28):141-143.
- [8] 商秀玉.WebGIS 海量瓦片数据管理引擎的设计与实现[D].金华:浙江师范大学,2012.
- [9] 王林飞,薛典军,何辉,等.插件技术在 GeoProbe 地球物理软件平台中的应用[J].物探与化探,2013,37(3):547-551.
- [10] 王林飞.插件式地球物理软件开发平台(GeoProbe)设计、实现与应用[D].北京:中国地质大学,2013.
- [11] 邓世军,孟令硅,吴沉寒,等.基于 SOAP 的海量空间数据服务[J].地理空间信息,2005,3(5):31-34.

A MARINE AEROMAGNETIC DATABASE FOR EFFICIENT DATA MANAGEMENT

WANG Linfei, XUE Dianjun, LI Fang, HE Hui, FENG Lei, ZHOU Wei

(China Aero Geophysical Survey & Remote Sensing Center for Land and Resources, Beijing 100083, China)

Abstract: Following the principle of “integrated management of the sea and land”, we designed in this paper an airborne gravity database table structure to make a unified airborne geophysical database, which includes airborne magnetic data, airborne magnetic gradient data, airborne electromagnetic data and airborne gamma energy spectrum data. On the GeoProbe platform, we developed a software for data services by using plug-in technology and WebGIS technology. Then we integrated the data service software, the data acquisition software and the airborne geophysical remote sensing data directory service system, and finally established an incorporate airborne geophysical data management service system. Adopting standardized data sorting process and strict data quality inspection measures, we put the airborne gravity data from the Bohai sea, Yellow sea and other sea areas into the database, about 3.5 square kilometers of ocean airborne gravity data was stored in the database. As the result, a marine geophysical database covering an area of about 4.97 million square kilometers of the Bohai sea, the Yellow Sea, the East China Sea, and the South China Sea has been constructed. The database may provide a series of service products of the whole sea area for users.

Key words: airborne geophysical prospecting; database construction; database services; data sharing

高光谱遥感地质矿产工程化应用进展及展望

董新丰^{1,2}, 闫柏琨^{1,2}, 甘甫平^{1,2*}, 李娜^{1,2}, 于峻川^{1,2}, 刘榕源^{1,2}

(1. 中国国土资源航空物探遥感中心, 北京 100083)

(2. 自然资源部航空地球物理与遥感地质重点实验室, 北京 100083)

摘要 遥感技术作用于地质调查工作中的一种重要技术手段, 发挥着不可代替的作用, 随着遥感技术的发展, 高光谱遥感出现使得遥感在地质矿产领域的应用发生了质的变化。经过近十年的探索和实践, 已初步实现了高光谱遥感在地质矿产上的工程化应用。随着国产高光谱卫星的发射, 必将进一步推动其在地质矿产上的应用。本文从高光谱数据处理、信息提取、信息分析、找矿预测等方面对高光谱遥感地质矿产工程化应用进展进行了阐述。

关键词 高光谱遥感 遥感地质 矿物填图 找矿预测

0 引言

遥感以其独特的技术优势在地质矿产调查中发挥重要作用, 前人利用多光谱遥感技术开展岩矿信息提取并进行找矿预测取得了较丰硕的成果^[1-5]。多光谱遥感数据主要是对铁染、铝羟基、镁羟基、碳酸盐岩、硅化等岩矿信息进行提取, 而这些信息大多为造岩矿物或岩石地层组成矿物, 同时由于其光谱波段少, 致使提取的岩矿信息的准确性相对较差, 特别是铁染信息^[6], 这严重制约了其应用效果。随着遥感技术的发展, 高光谱遥感的出现使其对岩矿信息识别有了质的提升, 其已实现矿物信息的精细提取, 且准确性高达 90%以上^[7], 这些矿物信息为找矿预测提供了重要的参考资料^[8]。但是前期受高光谱数据限制原因, 高光谱遥感在地质矿产上的应用进展相对缓慢, 但是在成像光谱技术方法研究上取得了突飞猛进的发展, 主要集中在矿物光谱特征分析、高光谱数据预处理、信息提取和矿床尺度的示范应用等方面^[9-11], 这为其工程化应用奠定了坚实基础。在近十年内, 随着机载成像光谱仪的引进、消化、吸收, 我国在高光谱遥感地质矿产上的应用取得了显著进展。

1 高光谱遥感地质矿产工程化应用进展

1.1 高光谱遥感数据及预处理

目前, 国内所使用的高光谱遥感数据由机载成像光谱仪 HyMap-C 和 CASI_SASI 获取,

* 基金项目: 中国地质调查项目(DD20160068)、国防科工局高分专项(04-Y20A35-9001-15/17)

作者: 董新丰, 男, 1986 年出生, 2012 年获中国地质大学(北京)矿产普查与勘探硕士学位, 工程师, 目研究方向为高光谱遥感地学应用研究。E-mail: dongxinfeng229@163.com。

通讯作者: 甘甫平, 男, 1971 年出生, 毕业于中国地质大学(北京)地图制图学与地理信息工程专业。研究员, 主要从事国产卫星国土资源应用综合论证、高光谱遥感技术方法研究和地学应用。E-mail: fpgan@aliyun.com。

Hymap-C 和 CASI_SASI 光谱范围为 0.4-2.5 μm , 光谱分辨率为 10-20nm。可根据调查工作程度需求, 控制飞行高度获取相应空间分辨率数据。为满足工程化应用需求, 结合多年的应用实践, 针对数据获取过程中的涉及的仪器定标、数据获取飞行方案设计、飞行测量、数据质量检查等方面已建立了一套技术规程。

大气校正与光谱重建和多航带 BRDF 校正是高光谱数据预处理的技术难点, 也是直接影响其工程化应用质量和效率。

1.1.1 大气校正与光谱重建

大气校正与光谱重建是地物识别和定量分析不可缺少的技术环节, 只有经过辐射标定、辐射畸变校正和大气校正, 将记录的图像值转换为地面的反射率值, 重建像元地面光谱, 才能根据光谱特征识别地物, 进而反演地物成分。目前, 辐射校正和光谱重建方法主要有三大类: 1) 基于图像统计特征的方法; 2) 基于地面同步实测光谱的地空回归方法; 3) 基于大气辐射传输模型的方法。其中基于图像统计特征的方法计算简便, 不需要额外参数, 缺点是受地域影响较大, 且容易对光谱形成平化效应或出现人为的光谱假象; 基于地面同步实测光谱的地空回归方法需要在数据获取时进行地面同步或准同步波谱测试, 该方法对定标点的依赖性较强, 因而对定标点要求苛刻, 一般选取比较困难。而且, 在不同地形地貌区, 如山脊和山谷, 不同的景观区, 如村庄、农田和湖泊, 虽然相距不远, 但大气成分如水气含量很可能会有明显差异, 地空回归很难照顾到这些局部的变化; 基于大气辐射传输模型的方法逐渐成为光学遥感大气校正与光谱重建的主流方法, 精度较高, 且不需进行同步测量, 在工程业务化应用主要采用就是该方法。

基于大气辐射传输模型方法可校正 H₂O、CO₂、O₂、O₃、CO、CH₄ 等气体的吸收, 气溶胶和分子的散射作用。其中, 水蒸气含量和气溶胶对图像的影响最大。对于高光谱数据, 可利用 820、940、1135nm 附近的大气水汽吸收谱带进行大气水汽分布反演, 进而最大程度的消除大气影响^[12]。

1.1.2 多航带 BRDF 校正及无缝拼接

由于飞行时间、飞行方向以及地面二向性反射(BRDF)的影响, 同一航带的不同部位、相邻航带之间的亮度都会有较大差异, 获得高光谱影像会出现明显的“条带状”异常, 且亮度的变暗一方面降低了目标与背景的对比度, 从而使矿物的检出率下降; 另一方面使图像的信噪比下降, 影响了矿物的识别能力。这对后期矿物信息提取影响较大, 直接影响了矿物信息识别的检出限和正确率, 特别是矿物的精细化识别。地表二向性反射校正与无缝拼图的目的是抑制或消除地表二向性反射特性引起的航带间光谱差异, 降低矿物识别的检出限, 增强高

光谱矿物弱信息提取和精细信息识别能力，提高信息提取效率。矿物弱信息识别和精细化区分能力决定着高光谱遥感在地质矿产应用上的广度和深度。针对地表二向性反射校正与无缝拼图这一技术难点，开展了多航带裸露地表 BRDF 校正方法研究（图 1），已成功推广到工程化应用中。

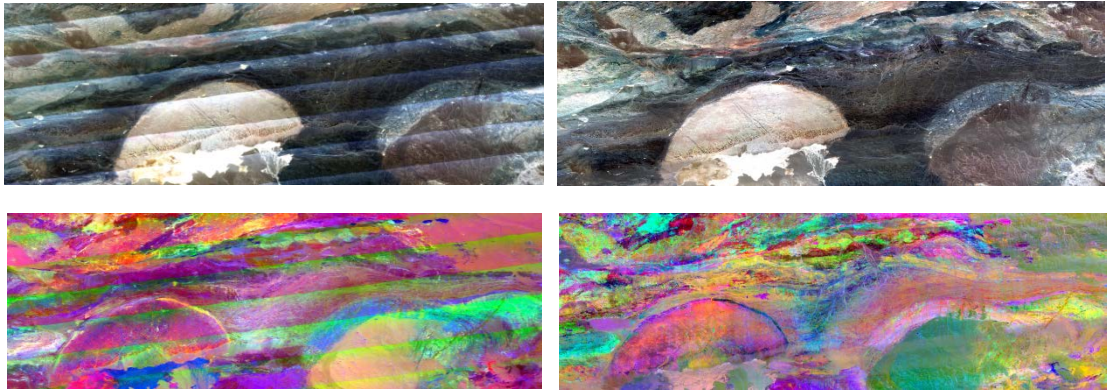


图 1 地表二向性反射 (BRDF) 校正与无缝拼图

Fig.1 Correction of Bidirectional Reflectance Distribution Function and seamless Mosaic

（左上：未经 BRDF 校正的数据；左下：未经 BRDF 校正的 MNF 变换结果；右上：经 BRDF 校正的数据；右下：经 BRDF 校正的 MNF 变换结果）

1.2 高光谱遥感矿物信息提取

归纳国内外发展的矿物信息提取方法有两大类：光谱相似性和光谱特征参量。光谱相似性就是将影像像元光谱与参考光谱进行比较，计算两者的相似度，以相似测度来完成矿物信息识别。传统的光谱相似性方法有光谱角^[13]、距离法（欧式、马氏距离）^[14]、光谱信息散度^[15,16]、匹配滤波、混合调制匹配滤波等方法。实践应用中发现，这些方法应用相对简单，但是对具有光谱特征相似和次级吸收特征差异不敏感，造成矿物识别能力相对较差、信息检出率低等缺点。光谱特征参量信息提取是以诊断性光谱吸收谱带的特征参量为基础的局部光谱识别方法，这些特征参量有谱带的波长位置 (P)、波段深度(H)、宽度(W)、斜率(K)、面积(A)及对称度(S)^[17]等等。代表性的方法有光谱特征拟合 (SFF, Spectral Feature Fiting)、光谱吸收指数 (SAI, Spectral Absorption Index) 和吸收谱带定位分析(AABP, Analysis of Absorption Band Positioning) 等。基于光谱特征参量法相对光谱匹配法，增强了对地物的区分能力，但在实际应用中，其极易受光谱信噪比、矿物混影响^[18]。

在应用实践中，提出了一种综合匹配度和特征参量高光谱矿物信息提取方法。该方法的工作思路是先利用光谱相似性方法进行矿物大类或矿物种类识别，在此基础上再利用特征参量方法对矿物亚类进行区分。该方法的前提是光谱相似性结果一定准确可靠，为此，开发出了一种基于光谱特征增强的匹配度算法^[19]，该匹配度算法较传统光谱相似性方法具有识别

矿物信息的检出限更低，正确率更高特点。甘甫平等^[20]根据矿物诊断性吸收谱带特征、多谱带组合特征的相似性和稳定性以及不同具体矿物谱带特征的变异性，初步建立了“矿物大类-族-种-亚种”的矿物识别分层谱系。根据该矿物识别分层谱系，结合综合匹配度和特征参数信息提取方法，在工程化应用中经实践验证，该方法矿物信息提取结果具有检出率低、正确率高特点（图2），正确率高达90%以上^[7]。

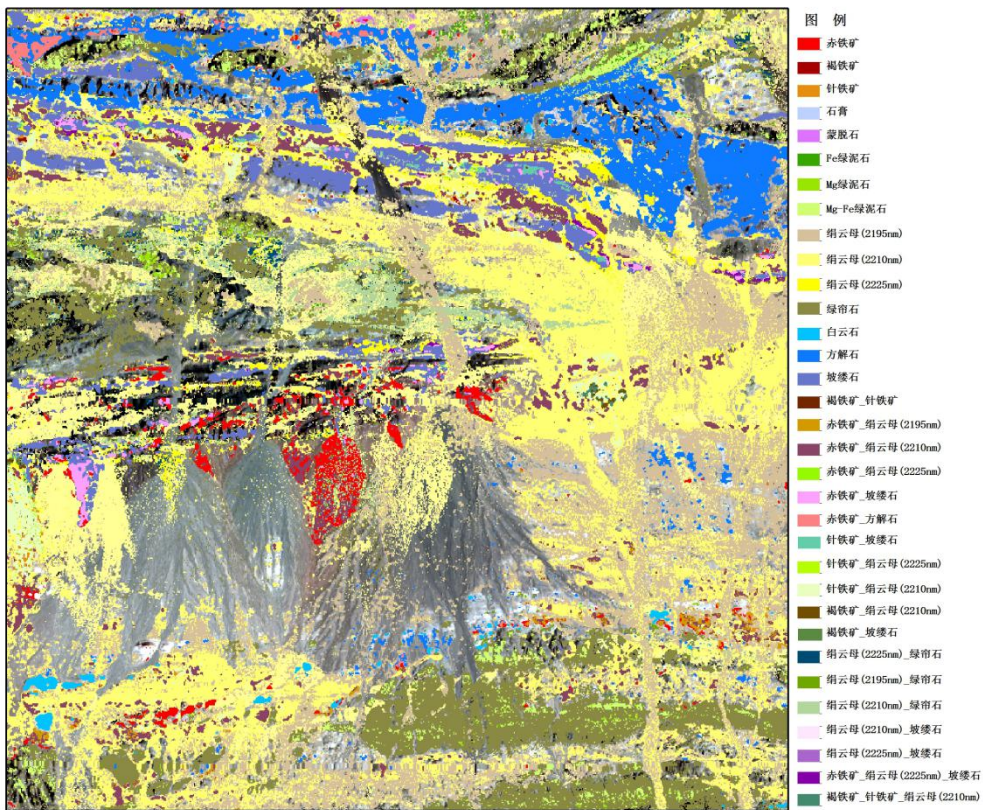


图2 高光谱遥感矿物分布图
Fig.2 Minerals distribution from Hymap hyperspectral data

1.3 高光谱遥感矿物信息地质含义分析

通过高光谱遥感可识别矿物信息种类已多达三十余种^[7]，但是在自然界中多数矿物信息往往有多种成因，包括区域变质、蚀变、风化等等，同样高光谱遥感可提取的矿物多数也具有多种地质成因的特点。因此在利用高光谱矿物信息开展地质矿产调查时，首先要对其地质含义进行分析。不同成因的矿物其产出形态、特征及产出地质背景均有所不同，比如说区域变质作用产生的绢云母化，其与地质背景关系密切，多呈带状、面状与变质地质体产出一致。

通过高光谱遥感提取的矿物很多是矿床中重要的蚀变矿物，如褐铁矿、绢云母、绿泥石、明矾石、高岭石、地开石、蛇纹石、透闪石等等；还有些矿物既可以是矿床中的蚀变矿物，也可是矿床的赋矿岩石信息，比如碳酸盐岩矿物（方解石、白云石等），其既可在成矿过程中形成或发生重结晶，也可作为铅锌、金、锑、汞等矿床的赋矿围岩；另外，还有些矿物信

息可直接指示矿(化)体的存在,比如赤铁矿、菱铁矿等,当这些矿物信息具有一定范围时,多为含铁矿(化)体造成。利用高光谱矿物信息开展矿产资源调查正是根据它们的上述属性,并结合地质背景开展的。因此,高光谱区域性找矿预测的主要理论依据就是充分利用那些能够指示找矿或示矿的围岩蚀变矿物、赋矿地质环境指示性矿物、直接示矿矿物以及矿床在后期风化、氧化形成的指示性矿物。在分析这些矿物时,必须要结合其产出的地质背景及成矿环境,否则这些矿物信息将失去‘生命力’。

另外,随着传感器和信息提取技术的发展,利用高光谱遥感不仅可实现矿物信息的识别,其也可对类质同像或不同组成成分的矿物信息进行区分,这极大地提高了高光谱遥感在地质矿产领域的应用关广度和深度。不同的矿物种类、组成、类质同像替换信息可对其形成时的温度、压力、酸碱度等地质环境条件进行推断分析,尤其在热液成矿系统中,不同的蚀变矿物组合对应着一定的温压条件和 Ph 值范围。[Frank et al](#)^[21]利用不同矿物空间组合关系、绢云母成分分布特征等信息对热液运移路径和成矿机制进行了约束。目前,对这些精细矿物信息的地质环境条件指示意义应用研究还不够深度,开展相应研究工作不多^[22],还有待进一步研究。

1.4 高光谱遥感找矿预测应用

前期受高光谱数据限制,多是利用卫星高光谱数据对矿床尺度开展找矿预测的,或利用机载高光谱数据对某一特定成因类型矿产开展找矿预测的^[23-25]。而利用机载高光谱数据开展区域性的、多目标找矿预测是高光谱遥感工程化应用面临的一大挑战。

高光谱遥感不仅可提供大量的矿物信息,同时还可利用其光谱信息来区分区域内不同地质体、同岩体不同期次界限等,这些信息同样在地质找矿预测中具有重要参考价值。比如当预测某种产于特定地质单元(体)中的矿床类型时,寻找和掌握该地质单元(体)分布范围、展布特征是非常重要的。限于篇幅原因,在这里主要阐述如何利用高光谱遥感提取的矿物信息开展区域性找矿预测。

在实践应用中,利用高光谱遥感开展找矿预测经历相似类比找矿法、特定矿物目标找矿法、以及目前的“成矿地质背景+矿床成矿模式+高光谱矿物信息”三位一体找矿方法。随着实践应用的增加,高光谱遥感矿物信息与成矿地质理论结合越来越紧密,找矿预测效果越来越显著。

1.4.1 高光谱遥感相似类比找矿预测法

高光谱遥感相似类比找矿预测法与地质找矿方法中的相似类比法原理一致。就是根据已知矿(化)区段的高光谱矿物分布和组合特征,在其周边及外围相同地质背景地段寻找具有

相似的矿物组合。如图 3 所示,根据已知矿区内地质分析认为,区内褐铁矿和绢云母的组合对矿(化)体具有很强的指示作用,据此在该已知矿区南部约 1.5km 处,发现具有相似的褐铁矿和绢云母矿物组合,且均受近东西向断裂控制,呈条带状产出。经野外实地验证,发现多条石英脉,经采样分析单个样品最高的达 42.81g/t。

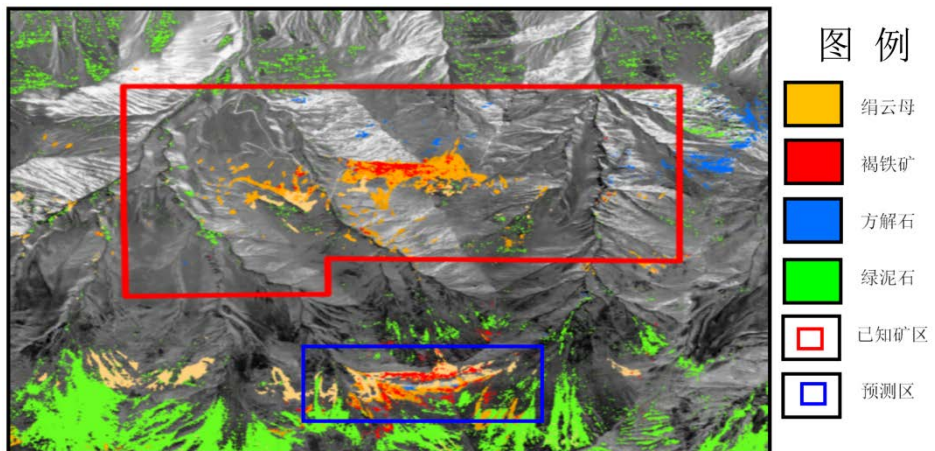


图 3 高光谱遥感找矿预测示意图

Fig.3 Sketch map of ore prospecting prediction by Hyperspectral Remote Sensing

1.4.2 高光谱遥感特定矿物目标找矿预测法

特定矿物目标找矿预测法具有很强的针对性,其是在已知调查区内某种矿物或某些矿物对寻找特定矿床类型具有直接找矿指示意义。比如在祁连山西北端镜铁山地区,经过分析发现该区域内沉积变质型铁矿很是发育,且含铁矿物主要为赤铁矿、磁铁矿和菱铁矿。而赤铁矿和菱铁矿具有其独特的光谱特征,利用高光谱遥感可快速对其进行识别和提取。从图 4 可见,镜铁山黑沟矿段的已知铁矿体(左图中红线圈定范围)与提取的赤铁矿分布一致。根据在该地区提取的赤铁矿和菱铁矿信息,在该地区发现多处铁矿(化)点。

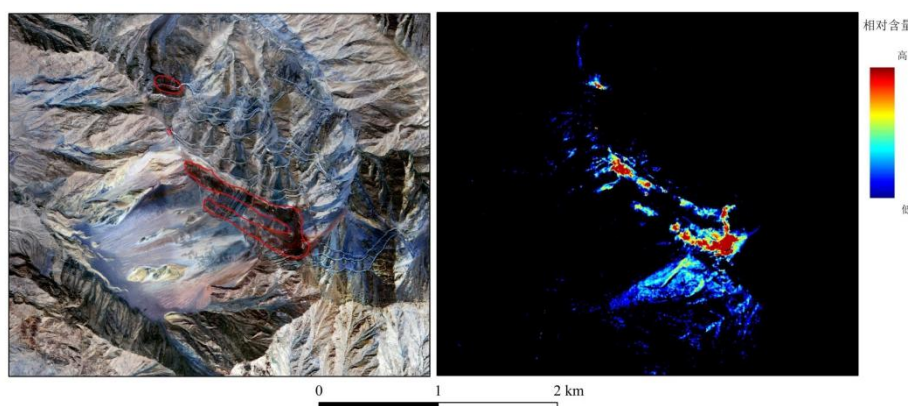


图 4 镜铁山黑沟铁矿区影像图(左)和赤铁矿含量分布图(右)

Fig. 4 Image map of Heigou mining area of jingtieshan iron deposit (left); Hematite abundance map(right)

1.4.3 高光谱三位一体找矿预测方法

随着高光谱遥感找矿预测实践的不断深入,高光谱遥感矿物信息与成矿地质理论结合的越来越紧密,初步提出了“成矿地质背景-矿床成矿模式-高光谱矿物”三位一体的高光谱遥感找矿预测模型。该模型直观地显示出了调查区成矿地质背景、主要矿床类型及其产出的地质环境、各矿床类型的成矿模式及其蚀变矿物空间组合特征(图5)。根据该模型,结合区内高光谱矿物信息及其产出的地质背景,可快速、有针对性地圈定预测区段。以往根据高光谱遥感找矿预测多是根据矿床的经典蚀变组合模型来开展的,但是实际应用中很难在地表发现其完整的蚀变组合情况。而该找矿预测模型可根据不同矿床的蚀变组合空间分布特征,结合其产出地质背景,即使只有蚀变外带发育,也会将其圈定出来。该找矿预测模型在实践应用得到很好的验证。

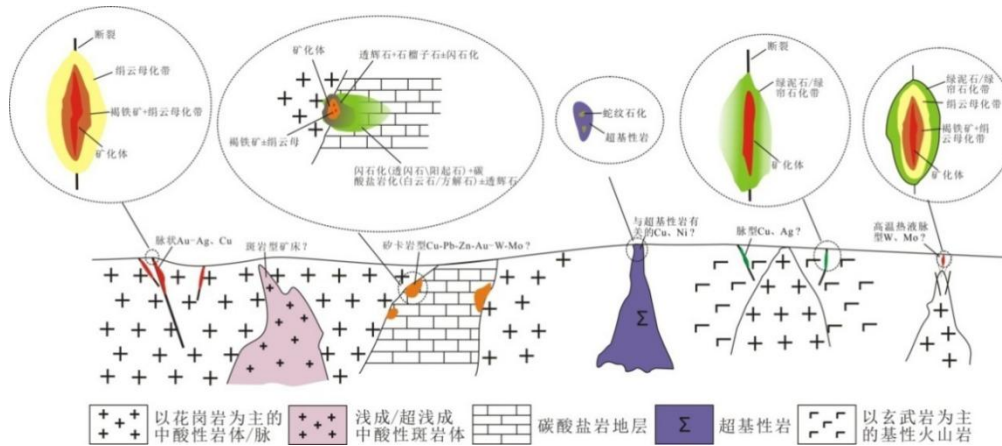


图5 甘肃柳园地区高光谱遥感找矿预测模式图

Fig.5 Hyperspectral remote sensing prediction model

1.5 高光谱遥感地质矿产专题产品

在实践应用中,根据高光谱遥感的技术特点,结合地质矿产调查的应用需求,总结了一套高光谱遥感地质调查产品体系,分为基础信息产品与综合分析信息产品2大类。基础信息产品包括影像图、矿物种类分布图、矿物丰度分布图、矿物成分信息分布图;综合分析信息产品包括蚀变异常分布图、高光谱遥感找矿预测图。蚀变异常分布图是在综合分析其产出地质背景、分布形态、与岩体、构造等地质体的空间关系以及其丰度信息等要素后,圈定出可能具有找矿或示矿作用的矿物信息,用曲线将其范围圈定出来。高光谱遥感找矿预测图在蚀变异常分布图的基础上,进一步分析各异常组合特征,并根据高光谱遥感找矿预测模型圈定具有进一步找矿或成矿潜力的区段。

2 高光谱遥感地质矿产应用展望

随着国产高光谱卫星的发射,以及传感器、数据处理、信息提取等技术的发展,高光谱遥感将在地质矿产领域取得进一步的发展,发挥更大的作用。

随着国产高光谱卫星的发射,高光谱数据源将会不断地增加,这将进一步推进高光谱遥感地质矿产工程化应用。未来,卫星高光谱遥感将在国内外重要成矿区带开展中比例尺地质

矿产调查，提供区域性矿物分布图、矿物丰度图、蚀变异常区带分布图、高光谱遥感找矿远景预测图。机载高光谱遥感将在重要成矿区带的重点地段或国家级整装勘查区开展大比例尺地质矿产调查，提供区内矿物分布图、矿物丰度图、蚀变异常分布图、高光谱遥感找矿预测图。

高光谱遥感数据预处理及精细矿物提取技术有待进一步提升。高海拔、高湿度地区的大气校正和多时相、多航带（多景）BRDF校正和无缝拼接将是未来高光谱遥感工程化应用中需要解决的技术难点。高光谱遥感的精细化信息提取直接决定着其应用广度和深度，精细化信息提取不仅包括精细矿物识别，同时包含矿物信息的定量化反演。另外矿物的中热红外谱段光谱分析和信息提取有待进一步加强。

高光谱遥感不仅在找矿预测中发挥重要作用，也将会在矿床成因机制研究、基础地质问题研究等方面提供重要信息。未来随着高光谱遥感在地质矿产领域的应用研究不断推广和深入，其提供的高光谱信息将会更多、更精细，专题性产品也会随之增加。这需要进一步加强高光谱遥感与地质理论的有机融合。开展天空地一体化协同应用研究，从宏观、局部到微观三个层次，加强高光谱遥感在区域地质背景、成矿地质环境、矿产资源预测评价、矿床成因机制等方面的应用研究。

参考文献

- [1] Crosta A. and Moore J. Enhancement of Landsat Thematic Mapper imagery for residual soil mapping in SW Minas Gerais State, Brazil: a prospecting case history in Greenstone belt terrain [A]. In: Proceeding of the 7th ERIM Thematic Conference: Remote sensing for exploration geology [C], 1989, 1173-1187.
- [2] Loughlin W.P. Principal Component Analysis for alteration mapping [J]. Photogrammetric Engineering and Remote Sensing, 1991, 57: 1163-1169.
- [3] Tangestani m.H and Moore F. Comparison of three Principal component analysis techniques to Porphyry copper alteration mapping: A case study, Meiduk area, Kerman, Iran [J]. Canadian Journal of Remote ensing, 2001, 27: 176-181.
- [4] Carranza E.J.M. and Hale M. Mineral imaging with thermatic mapper data or hydrothermal Alteration mapping in heavily vegetation terrain [J]. Intenational Journal of Remote Sensing, 2002, 23(22): 4827-4852.
- [5] Crowley J.K., Hubbard, B.E., Mars, J.C. Hydrothermal alteration on the cascade stratovolcanoes: A remote sensing survey [J]. Geological Society of America Abstracts with Programs, 2003, 35(6):552.
- [6] Cui Jing, Yan Bo-kun, Tian Feng, Liu De-chang, Wang Run-sheng, Yang Su-ming, Shen Wei. Regional-scale minerals mapping using ASTER VNIR/SWIR data and validation of reflectance and mineral map products using airborne hyperspectral CASI/SASI data[J]. Int. J. Appl. Earth Observ. Geoinform. 2014, 33, 127-141.
- [7] Yan Bo-kun, Dong Xin-feng, Wang Zhe, Yang Su-ming, Yu Jun-chuan, Li Na, Gan Fu-ping. Mineral information extraction technology by airborne hyperspectral remote sensing and its application progress: An example of mineralization belts of western China[J]. Geological Survey of China(闫柏琨, 董新丰, 王喆, 杨苏明, 于峻川, 李娜, 甘甫平. 航空高光谱遥感矿物信息提取技术及其应用进展——以中国西部成矿带调查为例. 中国地质调查), 2016, 3(4) : 55-62 (in Chinese with English abstract)

- [8] Dong Xin-feng, Yan Bo-kun, Cui Jing, Yang Su-ming, Wang Run-sheng, Yu Jun-chuan. Airborne hyperspectral remote sensing mineral information extraction and its application in geological prospecting[J]. Mineral Deposits(董新丰, 闫柏琨, 崔静, 杨苏明, 王润生, 于峻川. 航空高光谱遥感岩矿信息提取及在地质找矿中的应用. 矿床地质, 33(增刊)), 2014, 33(Suppl): 671-672 (in Chinese) .
- [9] Rockwell B.W., Cunningham C.G., Breit G.N., Rye R.O. Spectroscopic Mapping of the White Horse Alunite Deposit, Marysvale Volcanic Field, Utah: Evidence of a Magmatic Component. Economic Geology, 2006, 101, 1377-1395.
- [10] van der Meer F.D. Indicator kriging applied to absorption band analysis in hyperspectral imagery: A case study from the Rodalquilar epithermal gold mining area, SE Spain. International Journal of Applied Earth Observa, 2006, 8, 61-72.
- [11] Zadeh M.H., Tangestani M.H., Roldan F.V., Yusta I. Sub-pixel mineral mapping of a porphyry copper belt using EO-1 Hyperion data. Advances in Space Research. 2014, 53, 440-451.
- [12] Gao, B.C., Montes, M.J., Davis, C.O., Goetz, A.F.H. Atmospheric correction algorithms for hyperspectral remote sensing data of land and ocean[J]. Remote Sens. Environ, 2009, 113,S17-S24.
- [13] Yuhas R.H, Geotz F.H.A, Boardman J.W. Descriimination among semi-arid landscape endmembers using the Spectral Angle Mapper (SAM) algorithm [A]. Summaries of the Third Annual JPL Airborne Geoscience Workshop[C]. Pasadena, CA: JPL Publication, 1992, 147-149.
- [14] Fenstermaker L.K, Miller J.R. Identification of fluvially redistribute mill tailings using high spectral resolution aircraft data[J]. Photogrammetric Engineering & Remote Sensing, 1994, 60(8): 989 -995.
- [15] Chang C.L. An information-theoretic approach to spectral variability, similarity, and discrimination for hyperspectral image[J]. IEEE Trans. Information Theory, 2000, 46(5): 1927 -1932.
- [16] Freek Van der Meer. The effectiveness of spectral similarity measures for the analysis of hyperspectral imagery [J]. International Journal Applied Earth Observation and Geoinformation, 2006, 8(1) : 3 -17.
- [17] Clark R.N, King T.V.V, Klejwa M, et al. High Spectral Resolution Reflectance Spectroscopy of Minerals[J]. Journal of Geophysical Research, 1990, 95: 12653 -12680.
- [18] WANG Run-sheng,YANG Su-ming,YAN Bo-kun.A review of mineral spectral identification methods and models with imaging spectrometer[J].Remote Sensing for Land & Resources(王润生, 杨苏明, 闫柏琨. 成像光谱矿物识别方法与识别模型评述. 国土资源遥感), 2007,19(1):1.9. (in Chinese with English abstract)
- [19] GAN fu-ping, YAN Bo-kun, DONG Xin-feng, LIANG Shu-neng.Research progress of spectrometry geological remote sensing[J].Journal of Nanjing University of Information Science and Technology(Natural Science Edition)(甘甫平, 董新丰, 闫柏琨, 等. 光谱地质遥感研究进展[J]. 南京信息工程大学学报(自然科学版)), 2018, 10(1):44-62. (in Chinese with English abstract)
- [20] GAN fu-ping,WANG run-sheng,MA ai-nai.spectral iden-tification tree (sit) for mineral extraction based on spectral characteristics of minerals [j]. earth science frontiers(甘甫平, 王润生, 马蔼乃. 2003. 基于特征谱带的高光谱遥感矿物谱系识别[J]. 地学前缘), 2003,10(2): 445 -454. (in Chinese with English abstract)
- [21] Frank J.A. van Ruitenbeek et. al. Characterization of the hydrothermal systems associated with Archean VMS-mineralization at Panorama, Western Australia, using hyperspectral, geochemical and eothermometric data.Ore geol. Rev., 2012, 45:33-46.
- [22] YE Fa-wang,MENG Shu, ZHANG Chuan, XU Qing-jun, LIU Hong-cheng, WU Ding. Minerageny stdy of High-Al, Medium-Al, Low-Al sericitcs identified by airborne hyperspectral remote sensing technology[J]. Acta Geologica Sinica(叶发旺, 孟树, 张川, 徐清俊, 刘洪成, 武鼎. 航空高光谱识别的高、中、低铝绢云母矿物成因学研究. 地质学报), 2018, 92(2): 395-412. (in Chinese with English abstract)
- [23] Bierwirth P. Hyperspectral Mapping of Mineral Assemblages Associated with Gold Mineralization in the Central Pilbara, Western Australia. Economic Geology. 2002, 97 (4) :819-826.

- [24] Bishop C.A., Liu J., Mason P.J. Hyperspectral remote sensing for mineral exploration in Pulang, Yunnan Province, China. International Journal of Remote Sensing. 2011, 32, 2409-2426.
- [25] Cui, J., Yan, B.K., Dong, X.F., Zhang, S.M., Zhang, J.F., Tian, F., Wang, R.S. Temperature and emissivity separation and mineral mapping based on airborne TASI hyperspectral thermal infrared data. Int. J. Appl. Earth Observ. Geoinform, 2015. 40, 19-28

Progress and prospectives on engineering application of hyperspectral remote sensing for geology and mineral resources

DONG Xinfeng^{1,2}, YAN Bokun^{1,2}, GAN Fuping^{1,2*}, LI Na^{1,2}, YU Junchuan^{1,2}, LIU Rongyuan^{1,2}

(1. China Aero Geophysical Survey & Remote Sensing Center for Land and Resources, Beijing 100083, China)

(2. Key Laboratory of Aero Geophysics and Remote Sensing Geology of China Ministry of Natural Resources,
Beijing 100083, China)

Abstract: Remote sensing technology plays an important role in geological survey and plays an irreplaceable role. With the development of remote sensing technology, the appearance of hyperspectral remote sensing makes the application of remote sensing in geological and mineral fields have undergone a qualitative change. After nearly ten years of exploration and practice, the engineering application of hyperspectral remote sensing in geology and mineral resources has been preliminarily realized. With the launch of domestic hyperspectral satellites, it will further promote its application in geology and mineral resources. In this paper, the progress of engineering application of hyperspectral remote sensing in geology and mineral resources is summarized from the aspects of hyperspectral data processing, information extraction, information analysis, prospecting and prediction.

Key word: hyperspectral remote sensing; Remote sensing geology; mineral mapping;
ore-prospecting

国际军事地球科学会议发展脉络及特点^{*}

孟庆奎 高维 王晨阳

(中国国土资源航空物探遥感中心, 北京 100083)

摘要 自1994年至2017年, 美国地质学会主导的国际军事地球科学会议历经12届, 每届间隔约2年, 召开地点以美国本土为主, 参会代表主要为军地双方从事与军事地球科学相关的工作者或关注军事地球科学事业发展的科学家, 大会主题围绕两个方面展开, 一是军事地球科学在战争中的作用, 二是战争对军事地球科学的影响。美国地质学会在推动军事地球科学发展和宣传军事地球科学研究成果方面贡献突出, 是世界各国了解和学习美国军事地球科学的一条重要渠道。

关键词 军事地球科学 国际会议 发展脉络 发展特点

Development and Characteristics of the International Conference on Military Geoscience

MENG Qingkui GAO Wei WANG Chenyang

(China Aero Geophysical Survey and Remote Sensing Center for Land and Resources, Beijing 100083)

Abstract From 1994 to 2017, the Geological Society of America had organized 12 sessions of the international military geoscience conference, interval of about 2 years between two sessions, and mainly held in the United States. Participants were mainly the military workers related geoscience or the scientists pay attention to the development of military geoscience. The theme of the conference around two aspects, the one was the application of the military geoscience in the war, the other was the impact of the war on the military geoscience. The Geological Society of America had made outstanding contributions to promoting the development of military geoscience and publicizing the achievements of military geosciences. It was an important channel for all countries in the world to understand and learn the US military geosciences.

Key Words military geoscience international conference development characteristics

1 历届国际军事地球科学会议

美国地质学会1994年首次在西雅图组织召开“国际军事地球科学会议”(International Conference on Military Geosciences, 以下简称ICMG), 其后系列会议的地点分别为伦敦(召集人: Rose and Nathanail 时间: 1996, 下同)、多伦多(Ehlen and Harmon 1998)、格林尼治(Doyle and Bennett 2000)、西点军校(Caldwell et al. 2003)、诺丁汉(Nathanail et al.)、维也纳(Häusler and Mang)、休斯顿(Harmon 2008)、拉斯维加斯(Eric V. McDo-

* 基金项目: 中国地质调查局地质调查项目(121201003000172701)。

nald 2011)、华盛顿 (Jose Centeno Mark Lyles 2013)、印第安纳波利斯 (2015) 和南非 (2017) 共 12 届，会议的主题和论文集公开发表时间详见表 1，值得注意的是论文集的公开发表一般都会有 2~6 年的推迟。据统计，这十二届会议收录军事地球科学相关的论文近 300 篇，具有重要的学术参考及实际应用价值。

表 1 历届国际军事地球科学会议

序号	时间	地点	召集人	主题	论文集公开出版时间
1	1994	西雅图	Underwood Guth	战争与和平年代军事地球科学	1998
2	1996	伦敦 华威大学	Rose Nathanail	地质与战争	2000
3	1998	多伦多	Ehlen Harmon	战争对环境的影响	2001
4	2000	格林尼治	Doyle Bennett	军事历史战场地形研究	2002
5	2003	西点军校	Caldwell	军事地理与地质研究	2005
6	*	诺丁汉	Nathanail	*	2008
7	*	维也纳	Häusler Mang	*	2011
8	2008	休斯顿	Harmon	21 世纪军事地球科学	2014
9	2011	拉斯维加斯	Eric V. McDonald Thomas F. Bullard	军事地球科学与沙漠战争	2016
10	2013	华盛顿	Jose Centeno Mark Lyles	医学地质学的军事应用	*
11	2015	印第安纳波利斯	*	军事地球科学展望	*
12	2017	南非	*	军事地球科学领域、研究和影响	*

注：“*”表示未检索到相关信息。

2 国际军事地球科学会议特点

2.1 涉及机构多参与人员广泛

据 1998 年美国公开出版的《战争与和平年代军事地球科学》论文集统计，涉及军事地球科学的人员主要来自大学（南密西西比大学、堪萨斯州立大学、美国海军学院、西阿拉巴马州立大学、密苏里大学、康奈尔大学）、美国地质调查局（917 国家中心、军事地球科学处）、国家实验室（桑迪亚国家实验室）、美国军队（美国陆军工程中心、美国

陆军地形工程中心、美国陆军工程兵团岩土与环境部队)以及其他一些未给出具体名称的单位(其地址为1911 Crestview Drive、817 Berwyn Drive、17215 Northeast 8th Street)。由此可见,美国相关军方和地方单位高度重视军事地质工作,涉及的部门多、领域广,详见表2。

表2 涉及军事地球科学的人员分布

序号	作者	单位	城市
1	David M. Patrick C. P. Cameron	美国南密西西比大学地质系	哈蒂斯堡市
2	James R. Underwood	堪萨斯州地质系	萨堪撕拉州 曼哈顿市
3	Peter L. Guth	美国海军学院海洋系	马里兰州 安纳波利斯市
4	George A. Kiersch	康奈尔大学	亚利桑那州 图森市
5	Michael S. Rosenbaum	伦敦帝国理工学院	伦敦
6	Walter E. Pittman	西阿拉巴马州立大学 社会科学学院	阿拉巴马州 利文斯顿
7	Edward P. F. Rose	皇家霍洛威大学 伦敦大学地质系	伦敦
8	Claude Pareyn	卡昂大学	法国卡昂
9	Gilbert Corwin	美国地质调查局 军事地球科学处	
10	Maurice J. Terman William Leith John Rodney Matzko Donald J. Percious	国际项目首席地质学家办公室 美国地质调查局 917国家中心	弗吉尼亚州 雷斯顿
11	James T. Neal	桑迪亚国家实验室	新墨西哥州 阿尔布开克市
12	William K. Wedge	密苏里自然资源部 地质和土地调查处	密苏里州 罗拉市
13	Michael S. Rosenbaum	诺丁汉特伦特大学 建筑与环境系	英国 诺丁汉市
14	M. Merrill Stevens	美国陆军工程中心	密苏里州 伦纳德伍德堡市

续表

序号	作者	单位	城市
15	Jack N. Rinker Robert B. Knowles Judy Ehlen John C. Jens	美国陆军地形工程中心	弗吉尼亚州 亚历山大市
16	Thomas E. Eastler	缅因大学 自然科学系	缅因州 法明顿市
17	Paul R. Fisher	817 Berwyn Drive	北卡莱罗纳州 威尔明顿市
18	Daniel B. Krinsley	2475 Virginia Avenue, N. W.	弗吉尼亚州 华盛顿特区
19	Louis DeGoest	17215 Northeast 8th Street	华盛顿 贝尔维尤
20	James T. Neal	1911 Crestview Drive	亚利桑那州 普雷斯科特
21	C. Paul Nathanail	英国诺丁汉特伦特大学	英国 诺丁汉
22	John N. Baehr	美国陆军工程兵团 岩土与环境部队	亚拉巴马州 莫比尔
23	Allen W. Hatheway	密苏里大学 地质与石油工程系	密苏里州 罗拉市

2.2 会议内容研究主题发生变化

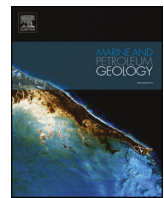
国际军事地球科学会议基本是每两年举行一次，然而之前并没有具体的会议名称，直到2009年才统一命名为ICMG。与历史军事地球科学相比，现代军事地球科学同样包括对传统的地质学和地理学研究，同时还包括对水文地质、考古及历史学等交叉学科的研究。从1994年西雅图ICGM到2017年南非ICGM，大致可分为两个主题。第一个主题是研究地质学和地理学如何影响历史战争及21世纪现代化战争。第二个主题是研究战争对地球的影响，特别是对近地表过程和历史景观、军事设施的管理和可持续发展、军事人员安全和环境卫生、文化资源的有效管理等。在第二个主题中越来越多的呈现出遥感技术、数字高程模型及数值模拟技术在军事活动中的应用。现代对自然、环境和文化资源的日益重视反映了全球对环境的观点和态度的转变，这些观点和态度不仅限于战场，而且还延伸到维持和平、反叛乱和灾难恢复等方面。近几年有关环境和文化的会议不仅展示了与战区有关的地质与地形研究，同时也体现了军事活动区和训练区的环境可持续发展。可见军事地球科学逐渐向环境可持续发展侧重。

2.3 军事地球科学应用历史悠久发挥作用大

历史及现代军事地球科学均具备重要性的应用价值。过去、现在和将来的军事活动总是与内容广泛的地球科学紧密结合起来。从最原始的使用石头当作武器到在攻防战略上利用地形地质，战争都与地形地质有着密切的关系，现代军事行动依赖陆、海、空全空间地形情报的实时动态获取。历史上许多陆上战役的成败在很大程度上是由地形地质决定，正如美国密苏里大学地质学者艾伦 W. 夏德威（2001 年）所言：最终证明部队军事能力的是对战役场地的掌握和有利条件的充分应用，然而战役场地就是地质，就是军事地质。

参考文献

- [1] David M. Patrick, Military Geology in War and Peace [J], GSA Reviews in Engineering, Vol. XIII. Eos, Vol. 80, No. 21, May 25, 1999
- [2] Maurice J. Terman. Military Geology Unit of the U. S. Geological Survey during World War II [C]. Military Geology in War and Peace, 1998
- [3] Maurice J. Terman. Military Geology Branch of the U. S. Geological Survey from 1945 to 1972 [C]. in Military Geology in War and Peace, 1998
- [4] <https://www.dri.edu/icmgl1/abstracts-->



Research paper

Marine strata morphology of the South Yellow Sea based on high-resolution aeromagnetic and airborne gravity data

Jing Tong^{a,b,3}, Xuanjie Zhang^{b,*,1}, Wan Zhang^b, Shengqing Xiong^{a,b,**,2}^a School of Geophysics and Information Technology, China University of Geosciences, Beijing 100083, China^b China Aero Geophysical Survey and Remote Sensing Center for Land and Resources, Beijing 100083, China

ARTICLE INFO

Keywords:
 Aeromagnetics
 Airborne gravity
 South yellow sea
 Marine strata
 Magnetic basement
 Indosinian suture

ABSTRACT

The paper focuses on the nature and the distribution of Paleozoic and Mesozoic marine strata of South Yellow Sea. The depths to the magnetic basement (bottom of the marine strata) and the Indosinian suture (top of the marine strata), and hence the gross thickness of marine sediments, are calculated and interpreted for the first time using the latest high-resolution aeromagnetic and airborne gravity data in South Yellow Sea. The residual thickness of marine strata is suspected to be greatly influenced by the uplift and denudation induced by Indosinian orogeny. The preliminary subdivision of Paleozoic and Mesozoic tectonic units is conducted. The Middle Depression and Southern Depression have the high preservation of the Paleozoic and Mesozoic marine sedimentation. A NW-trending fault belt is found to exist in the western onshore-offshore transition zone, and possibly control the Cenozoic and Mesozoic sedimentation. This study contributes to the oil-gas exploration of Paleozoic and Mesozoic marine strata in South Yellow Sea.

1. Introduction

Marine areas have become increasingly important, both in terms of their resources and politics, during this century. The South Yellow Sea, a large multicycle basin consisting of a Paleozoic–Mesozoic marine basin and a Mesozoic–Cenozoic terrestrial basin (Cai, 2002; Ren et al., 2002; Lee et al., 2006; Ouyang et al., 2009; Yuan et al., 2016), is of tremendous value because of its energy resources. The basins developed over a crystalline basement of pre-Sinian (The last period of the Neoproterozoic) metamorphic rocks, and marine strata of considerable thickness and terrestrial strata have been deposited subsequently (Zhang et al., 2014; Yao et al., 2005). The features of the terrestrial sedimentary basin of the South Yellow Sea are well-known after more than 50 years of regional oil and gas exploration. However, research on its Paleozoic–Mesozoic marine strata developed slowly prior to the availability of effective seismic reflection (Deng and Ou, 1995; Lin and Yao, 2009; Sun et al., 2014). Although previous studies have demonstrated the value of seismic reflection data as the main tool for the exploration of marine strata, sophisticated seismic data analysis (Lin and Yao, 2009; Qi et al., 2013, 2015; Zhang et al., 2014; Chen et al., 2016; Liu et al., 2016; Yuan et al., 2016) has failed to determine the

thickness distribution of the marine strata of the South Yellow Sea as a result of the low reflectivity of deep Paleozoic strata. Gravimetric and magnetic data have also been used to study the sedimentary basin (Wang and An., 2000; Dai et al., 2002; Liang et al., 2003; Zhang et al., 2007; Li et al., 2014a,b; Luo et al., 2014; Xing et al., 2014), but considerable discrepancies remain in the definition of marine strata morphology of the South Yellow Sea because of the limited precision of the geophysical data and its subsequent integration.

The current paper focuses on the calculation and interpretation of the depth to top and bottom of the Paleozoic and Mesozoic marine strata of the South Yellow Sea based on the latest high resolution aeromagnetic and airborne gravity data, covering latitudes 31° to 37°N and longitudes 120° to 124°E. On this basis, we determined the thickness distribution of Paleozoic–Mesozoic marine strata, conducted the corresponding geophysical and geological interpretation, and proposed a new schema for the morphology of the Paleozoic and Mesozoic marine strata.

* Corresponding author. China Aero Geophysical Survey and Remote Sensing Center for Land and Resources, Beijing 100083, China.

** Corresponding author. School of Geophysics and Information Technology, China University of Geosciences, Beijing 100083, China.

E-mail addresses: tongjing84@163.com (J. Tong), zhangxuanjie@163.com (X. Zhang), xsqagrs@126.com (S. Xiong).¹ Xuanjie Zhang, male, born in 1979, senior geophysicist and geologist, mainly engaged in marine geology and geophysics.² Shengqing Xiong, male, born in 1963, Professor, mainly engaged in geology and geophysics.³ Jing Tong, female, born in 1984, Ph.D. Mainly engaged in geophysics and petroleum geology.

<https://doi.org/10.1016/j.marpetgeo.2018.06.018>

Received 5 August 2017; Received in revised form 15 June 2018; Accepted 17 June 2018

Available online 18 June 2018

0264-8172/ © 2018 The Authors. Published by Elsevier Ltd. This is an open access article under the CC BY-NC-ND license (<http://creativecommons.org/licenses/BY-NC-ND/4.0/>).

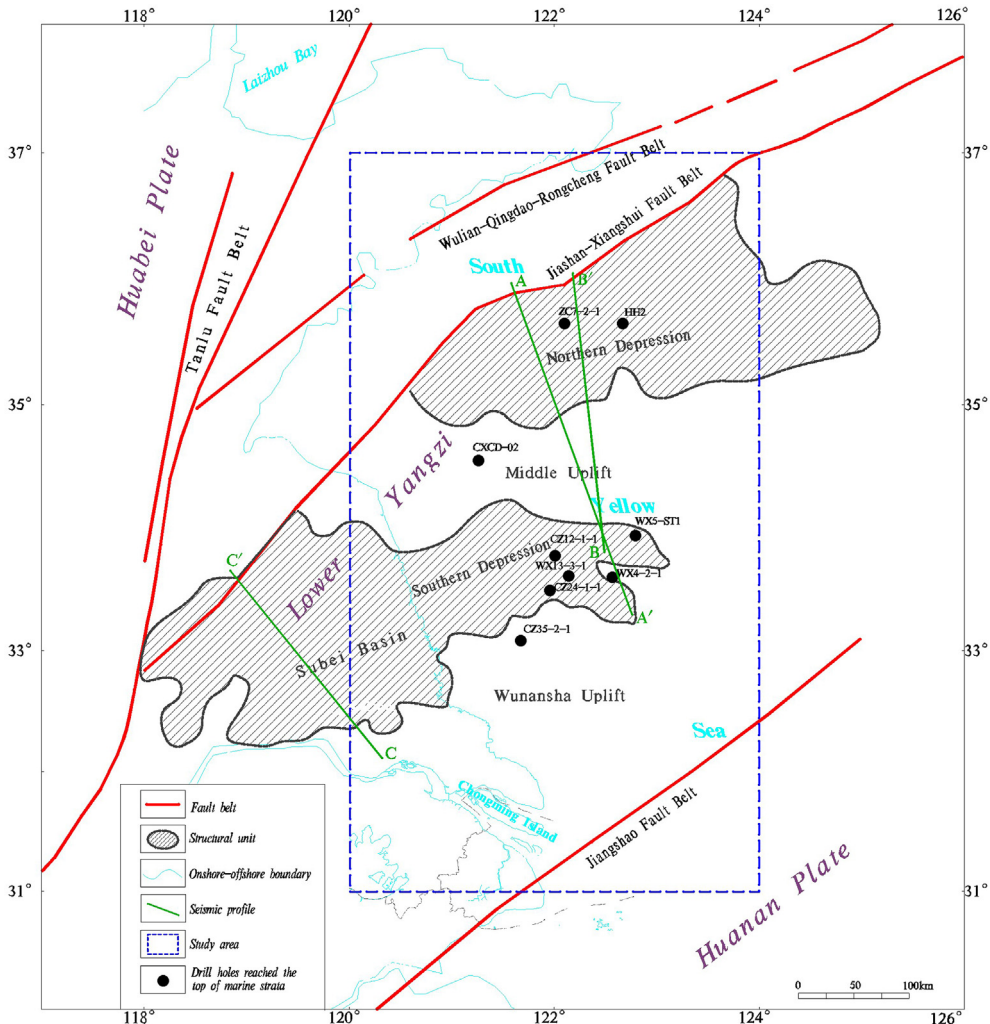


Fig. 1. Tectonic setting and structural outline of the South Yellow Sea (extended and modified from Guo et al., 1997 and Zhang et al., 2007). The blue dashed rectangle is the study area, which is also shown in Figs. 3, 7, 8, 9 and 12. (For interpretation of the references to color in this figure legend, the reader is referred to the Web version of this article.)

2. Regional setting

2.1. Geological setting

The study area in this paper covers latitudes 31° to 37°N and longitudes 118° to 124°E (Fig. 1), located in the northeastern lower Yangtze block. It is bounded by the Tanlu fault belt to the west, the Jiaoshan-Xiangshui fault belt to the north, and the Jiangshao fault belt to the south.

According to the distribution of the Mesozoic and Cretaceous terrestrial strata, the structural units of the South Yellow Sea can be subdivided tectonically from north to south into two uplifts and two depressions: namely, the Northern Depression, the Middle Uplift, the Southern Depression (adjacent to the Subei Basin), and the Wunansha Uplift (Fig. 1) (Guo et al., 1997; Zhang et al., 2007). The Paleozoic–Mesozoic marine sedimentary strata were formed during the Jinning orogeny and evolved until the Indosinian and Yanshanian orogenies, within which, the Cambrian, Ordovician, Carboniferous, Permian, and Lower Triassic marine strata developed (Yue et al., 2014; Pang et al., 2016). Several significant interfaces formed during the tectonic movements of the South Yellow Sea, including the upper interface of the pre-Sinian metamorphic rocks, caused by the Jinning orogeny (Wu et al., 2008; Hao et al., 2010; Shinn, 2015); the Caledonian suture that resulted from the tectonic events of the late Silurian to

early Devonian; and the Indosinian suture that was caused by Indosinian orogeny from the late Permian to the early Mesozoic (Grimmer et al., 2002; Yao et al., 2005; Shinn et al., 2010; Zhang et al., 2014). The crystalline basement has been shown to comprise pre-Sinian metamorphic rocks; thus, the upper interface of the pre-Sinian metamorphic basement was the base of the marine strata during the regional tectonic evolution (Zhang et al., 2007; Li et al., 2014a,b; Xing et al., 2014). The interpreted seismic profile of the South Yellow Sea clearly shows that the deformation character of the Lower Triassic and Permian strata differs from those of the Upper Triassic, Cretaceous, Jurassic, Paleogene, and Neogene, which establishes that the Indosinian suture was the top of the marine strata of the South Yellow Sea (Fig. 2) (Qi et al., 2013, 2015; Zhang et al., 2014; Liang et al., 2017).

2.2. Regional physical properties

The density and susceptibility of the strata are the basis of geophysical interpretation of magnetic and gravity data. They are key parameters in the identification of geophysical morphology. We measured more than 8000 susceptibility and density data from 350 rock sampling locations distributed in different strata in southern Shandong Peninsula and northern Jiangsu Province. Parameters from the same location, but different strata, were combined by an arithmetic mean. Physical properties that are based upon this study and published

A—A' seismic profile

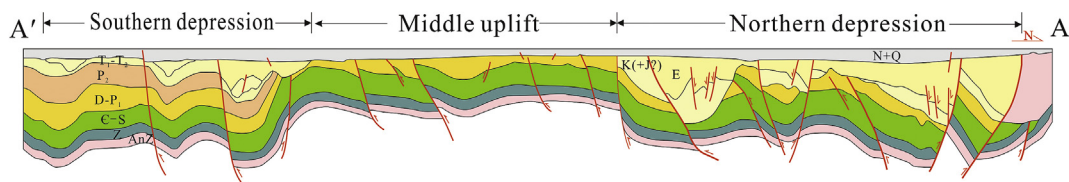


Fig. 2. Seismic stratigraphic sequence of the South Yellow Sea(modified after Liang et al., 2017). The location of this profile (AA') is shown in Fig. 1. (For interpretation of the references to color in this figure legend, the reader is referred to the Web version of this article.)

Table 1

Physical properties and distribution status of the strata in South Yellow Sea.

Stratigraphic sequence		Main lithology	Main unconformities	Density (g/cm ³)	Susceptibility (k × 10 ⁵ SI)	Distribution status of strata
Strata system						
Mesozoic—Cenozoic terrestrial strata	Neogene	Mudstone,sandstone,basalt,andesite, and clay	Yanshanian unconformity Indosinian suture	2.10	2.20	5–3753
	Paleogene	Sandstone, mudstone		2.29	10~45	Limited distributed
	Cretaceous	Mudstone, sandstone, conglomerate		2.53	2.56	0–100
	Jurassic	Conglomerate,		2.59	0–402	
Paleozoic—Mesozoic marine strata	Triassic	sandstone,shale, andesite, trachyte, tuff	Caledonian suture			
	Permian	Carbonate		2.68	2.68	5–101
	Carboniferous					Well distributed
	Devonian	Clastic		2.57		
Crystalline basement	Silurian		Jinning unconformity			
	Ordovician	Carbonate		2.68		
	Cambrian					
	Pt2–3	Lower metamorphic rocks		2.78	2.78	0–210
	Pt1—Ar	Deep metamorphic rocks				1118–4378

articles (Lin and Yao, 2009; Hou et al., 2012) are collated in Table 1.

The magnetic features of the strata can be represented by a very simple model, according to the statistics of susceptibility and the geological setting of the South Yellow Sea. It is shown that the Paleozoic–Mesozoic marine strata have either no or weak magnetization. The Mesozoic–Cenozoic terrestrial strata only develop some weak or local magnetization. In contrast, the Paleoproterozoic and Archean crystalline basement, being composed of deep metamorphic rocks, have rather stable and stronger susceptibility values, varying from 1118×10^{-5} to 4378×10^{-5} SI. They are identified as the magnetic basement of the South Yellow Sea and are inferred to be the main contributors to the change of regional magnetic anomalies. Thus, the aeromagnetic data is used to derive the depth of the top of the magnetic basement in this study.

Based on the statistics of the rock densities and the geological setting of the South Yellow Sea, there are four main density layers: namely, the well-distributed Cenozoic terrestrial strata across the whole study area, which have an average density of 2.20 g/cm³; the spatially limited Mesozoic terrestrial strata in the depression area, which have an average density of 2.56 g/cm³; well-distributed Paleozoic–Mesozoic marine strata across the study area, which have an average density of 2.68 g/cm³; and the well-distributed crystalline basement, which has an average density of 2.78 g/cm³. According to the aforementioned distribution of the main density layers, the Indosinian suture between the Mesozoic–Cenozoic terrestrial strata and the Paleozoic–Mesozoic marine strata is identified as the main density contrast. The density contrast associated with the suture demonstrates large and continuous regional undulations, with the largest density contrast values ranging from 0.12 g/cm³ (the contrast between Paleozoic–Mesozoic marine strata and Mesozoic terrestrial strata) to 0.48 g/cm³ (the contrast between Paleozoic–Mesozoic marine strata and Cenozoic terrestrial strata, where Mesozoic strata were denuded). Hence the depth of the Indosinian suture can be derived from airborne gravity data.

3. Aeromagnetic and airborne gravity data

3.1. Aeromagnetic data and field characteristics

The aeromagnetic data were measured by a helium optical-pumping magnetometer in an aeromagnetic survey with 1 km line spacing over the South Yellow Sea and its western onshore-offshore transition zone conducted by the China Aero Geophysical Survey and Remote Sensing Center for Land and Resources in 2004. The normal magnetic field correction used the IGRF 2000 model and data were processed using a method of reduction to the pole by variable inclination (Li et al., 2014a,b) to eliminate the effects of oblique magnetization.

The general aeromagnetic field characteristics of the South Yellow Sea can be regarded as a dominant circle shape, with gentle and high anomaly zones in the middle of the study area, according to the aeromagnetic data that have been reduced to the pole (Fig. 2), and is surrounded by dramatically changing positive and negative magnetic anomalies to the north and south. The aeromagnetic anomalies vary from -296 nT to +1535 nT, with apparent contrast between regional and local magnetic anomalies. The Northern Depression contains the majority of the gentle positive and negative magnetic anomalies; the Middle Uplift shows a widespread gentle increase with regional positive magnetic anomalies, accompanied by correspondingly decreasing negative magnetic anomalies; the Southern Depression is dominated by widespread and gentle negative magnetic anomalies, with some surrounding positive anomalies; and the Wunansha Uplift has widespread and gentle negative regional magnetic anomalies in its northern region and distinct positive and negative local anomalies with a northeast–southwest trend in the southern region.

3.2. Airborne gravity data and field characteristics

The gravity data comes from the airborne gravimetry of the China

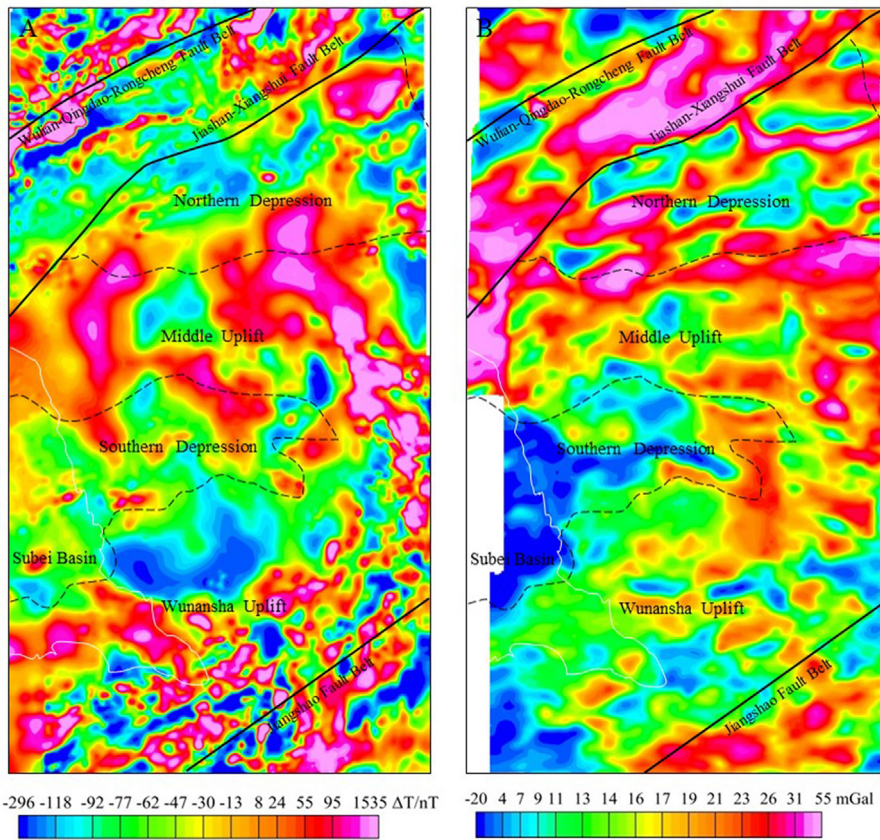


Fig. 3. (A) Color grid of the aeromagnetic data after being reduced to the pole in the study area. (B) Color grid of the airborne Bouguer gravity in the study area. (For interpretation of the references to color in this figure legend, the reader is referred to the Web version of this article.)

Aero Geophysical Survey and Remote Sensing Center for Land and Resources and was gathered using a Russian GT-1A airborne gravity meter system with a survey scale of 1:100,000 and a flight altitude ranging from 400 to 800 m. The internal accuracy of the mean square deviation of the airborne gravimetric measurement for a repeated line test is 0.6 mGal. The free-air gravity was acquired after field data preprocessing and indoor processing; then, the Bouguer gravity data was obtained by removing the terrain effects of the seabed and topography using the Terrain Correction modules of the Oasis Montaj software platform produced by Geosoft Inc. of Canada.

The study area shows widely distributed positive high anomalies with a few negative low value anomalies, which have apparent anomaly zones and belts, with gravity anomalies ranging from -20 mGal to $+55$ mGal (Fig. 3). The Northern Depression is dominated by high value anomalies with northeast – southwest or near east – west trending strip-shaped anomalies; the Middle Uplift shows negative low gravity values among high value anomalies; the Southern Depression is mainly shown as gentle and low anomalies; and the Wunansha Uplift has the majority of the high anomalies in the east, with only a few low anomalies in the west. In general, the distribution of the Bouguer gravity anomalies corresponds well with the structural framework of the “two uplift and two depression zone” model of the South Yellow Sea, although there are some instances of the airborne Bouguer gravity anomalies varying dramatically over a short distance and some high frequency anomalies existing among regional anomalies.

4. Methodology and results

4.1. Regional – residual separation

Both aeromagnetic data and airborne Bouguer gravity data are

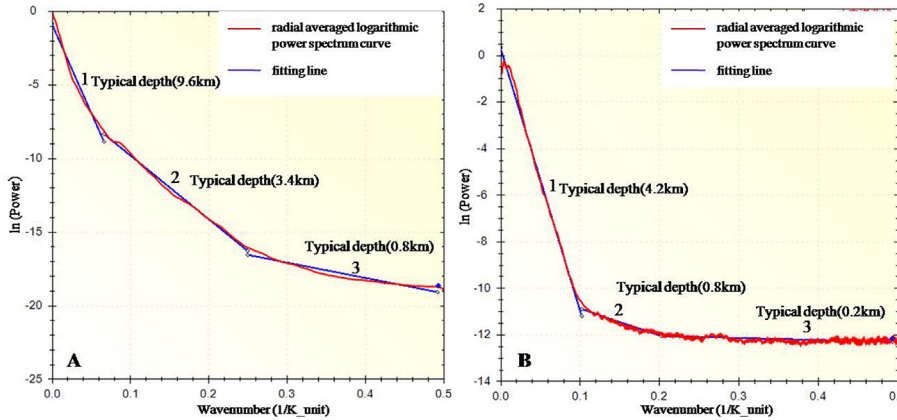
composed of regional and residual components. The regional components, caused by abnormal geological bodies with a certain large scale and wide distribution, are our target that should be isolated from the original data.

Matched filtering, based on radially averaged logarithmic power spectra, is an effective method for this data separation (Keating and Pinet, 2011; Wang et al., 2015). A good curve of the radially averaged logarithmic power spectra is the prerequisite for the application of the method, as the matched filter factor is optimized by the fine linear fitting of the curve. We selected a typical basin in the study area to apply this method as an experiment. Firstly, we calculated the averaged logarithmic power spectrum of the magnetic (AT) data with magnetic pole reduction and the first-order vertical derivative of the Bouguer gravity data separately. Secondly, we performed a fine linear fitting of the spectrum curve to optimize the filter factor, shown in Fig. 4. The frequency range of segment no. 3 in Fig. 4 is the largest of all three segments, and is selected to be the filter factor. Thirdly, the regional anomalies are separated from residual anomalies, shown in Fig. 5.

Fig. 5B and D presents the regional aeromagnetic and Bouguer gravity anomalies while Figs. 5A and C show higher frequency residual aeromagnetic and Bouguer gravity anomalies, respectively. The regional anomalies have simpler undulating characteristics with greatly reduced amplitude relative to the residual anomalies. By applying this method, the regional anomalies of the whole area are obtained.

4.2. Depth inversion

The Vacquier and tangent methods are two mature methods used to calculate the buried depth of magnetic bodies (Vacquier et al., 1951; Sparker, 1963; Xiong, 2010; Zhu, 2012; Xiong et al., 2014). Based on the theory of magnetic and gravity potential field transformation, the



Vaquier and tangent methods have also been successfully used in depth calculation of density interfaces by us since 2010 (Xiong et al., 2014). The statistical depth calculation error of a density interface ranges from 10% to 20% (Xiong et al., 2014) by the first vertical derivative of the gravity anomaly profile. We applied both the Vaquier and tangent methods to calculate the buried depth of magnetic bodies and density interface and then obtained the depths of the magnetic basement and Indosinian suture, respectively.

The decision whether to use the Vaquier or tangent method depends on the geometry of the profile of the aeromagnetic ΔT data and the first vertical derivative of the airborne gravity data. For symmetrical anomaly profiles, the tangent method is used. First, tangential lines are drawn at the peak and the two inflection points of the given anomaly curve, shown in Fig. 6A. The intersections between the side tangent lines and the peak tangent line are projected onto the X-axis, given X_2 and X_3 . The side tangent lines intersect with the X-axis at X_1 and X_4 respectively. Next, the morphological parameter of abnormal symmetric is calculated as $K_1 = (X_4 - X_1)/(X_3 - X_2)$. Thirdly, the depth factor of the buried geologic body, denoted as K_h , can be obtained in the

standard table of coefficients of the tangent method by searching for K_1 . Finally, the buried depth of the top surface is calculated by $h = (X_4 - X_3)/K_h$.

For asymmetric anomaly profiles, the Vaquier method is used to approximate the depth to the buried magnetic source. A tangent is drawn at the inflection point, shown in Fig. 6B. X_1 and X_2 are the horizontal coordinates of the overlapped end-points. Then the buried depth of top surface is calculated by $h = K^*(X_2 - X_1)$, where the coefficient K has to be chosen by experience.

The depth of the magnetic basement and the Indosinian suture in the South Yellow Sea was obtained by the following procedure. Firstly, we extracted profiles from the separated regional aeromagnetic ΔT grid data with magnetic pole reduction and the first vertical derivative of the separated regional airborne Bouguer gravity grid data. 16510 depth point-related data of magnetic bodies and 18015 depth point-related data of pseudo-magnetic bodies were obtained by using automatic inversion software with the tangent and Vaquier methods. Secondly, based upon the geological and geophysical interpretations, we compiled a depth contour map of the top of the magnetic basement and

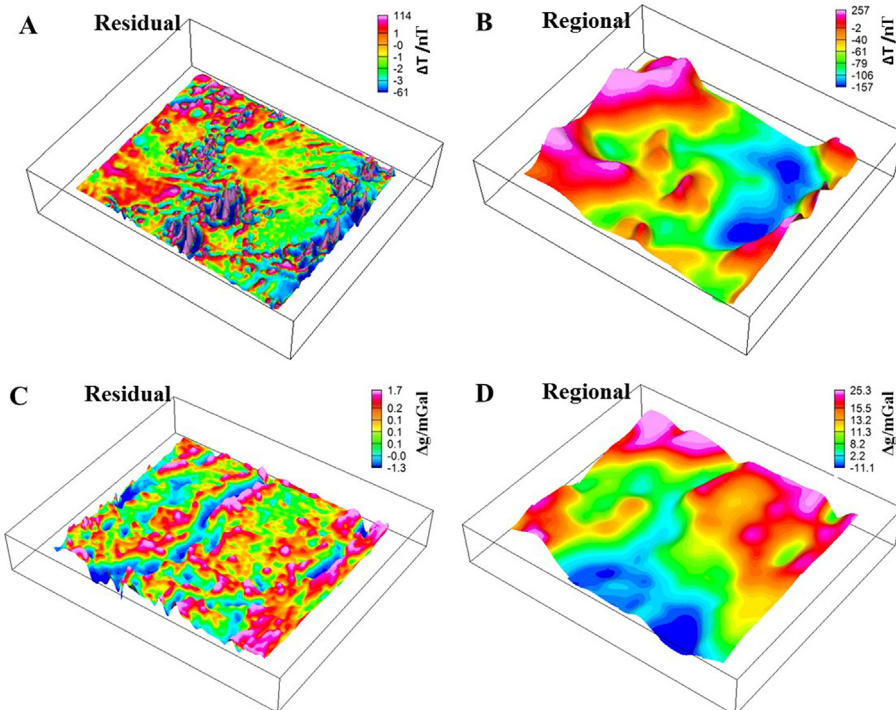


Fig. 5. (A) Separated residual aeromagnetic (ΔT) anomalies. (B) Separated regional aeromagnetic (ΔT) anomalies. (C) Separated residual Bouguer anomalies. (D) Separated regional Bouguer anomalies.

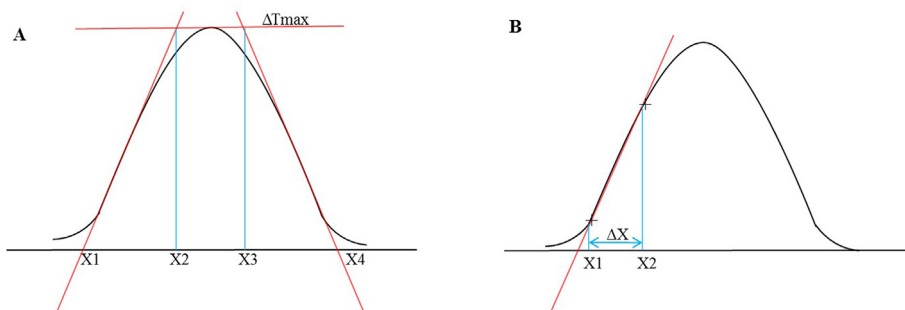


Fig. 6. (A) Sketch showing the tangent method for symmetric anomaly profile. (B) Sketch showing the Vaquier method for an asymmetric anomaly profile.

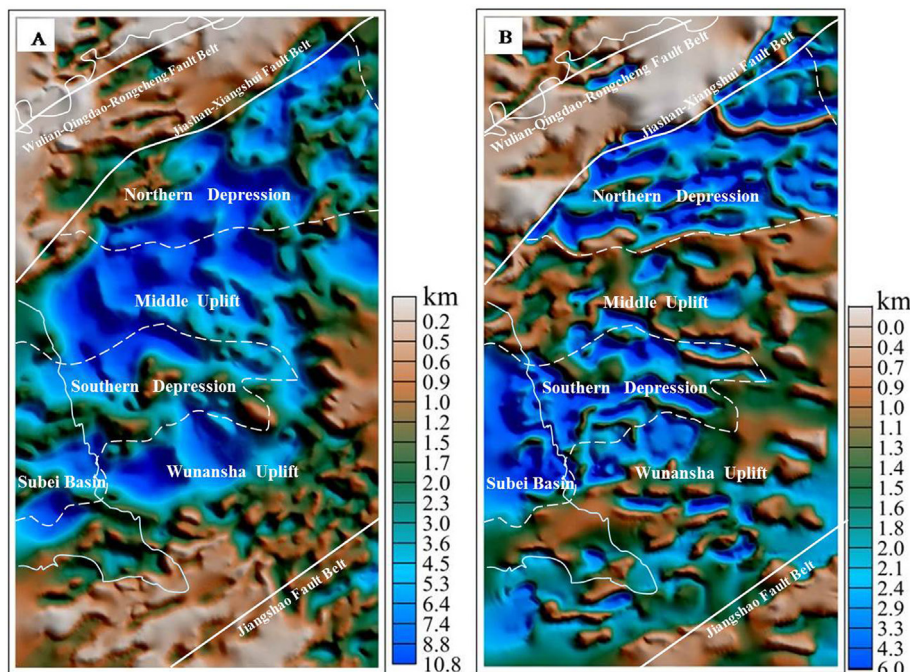


Fig. 7. (A) Color shaded grid of the depth of the top of the magnetic basement. (B) Color shaded grid of the depth of the Indosinian suture. (For interpretation of the references to color in this figure legend, the reader is referred to the Web version of this article.)

Indosinian suture by drawing the depth contours with varied spacing from 0.5 km, 1.0 km, 1.5 km, 2.0 km, 3.0 km, 5.0 km, 7.0 km and 9.0 km. Thirdly, we calculated the color shaded grid of the depth of the magnetic basement and Indosinian suture (Fig. 7) by deriving a digital terrain model from the contours.

Since it is impossible to evaluate the error in the depth calculation of the magnetic basement directly because of the lack of deep drilling data offshore the South Yellow Sea, we compared the calculated depth results close to 0 with the outcrop magnetic strata and rocks around Shandong and Jiangsu, and then we confirmed that the statistical depth calculation error of the top of the magnetic basement is within 20%. In addition, we also compared the depth results of the magnetic basement (Fig. 7A) to the depth solutions produced by the Standard Euler3D method in Oasis Montaj (Fig. 8). It was noticed that the depth locations and specific trends obtained from the Euler deconvolution generally corresponded well with our depth results, which supports the reliability of our depth result of the magnetic basement. To evaluate the precision of the depth calculation of the Indosinian suture, we derived the error by comparing the calculated results with the measured depth from eight boreholes (Table 2). These wells are all located in the study area shown in Fig. 1 and reached the top of the marine strata. The relative error of the Indosinian suture calculation ranges from 0.82% to 19.69%, with a deviation of 14–409 m. The error analysis of the two interfaces depths proved the reliability of the calculation method and its comprehensive

interpretation.

4.3. Thickness calculation

The thickness of the marine strata is required for the recognition of the morphology of Paleozoic and Mesozoic marine strata, and for the exploration of oil and gas-prone structures. Based on the stage of tectonic evolution and the regional physical properties of the South Yellow Sea, the top of the magnetic basement and the Indosinian suture can be determined as the bottom and top interfaces, respectively, of the Paleozoic and Mesozoic marine strata. The thickness of these units is simply the difference between the depth of the bottom and top interfaces, which is shown in Fig. 9. When the difference of magnetic basement and crystalline basement is taken into consideration, it needs to be stated that the calculated marine strata thickness are probably larger than the real thickness.

5. Discussions and conclusion

5.1. Magnetic basement

As illustrated in Fig. 7A, the depth of magnetic basement is greater in the central area, and shallower in the both the northern and southern areas of the South Yellow Sea. In the northern part of the study area, the

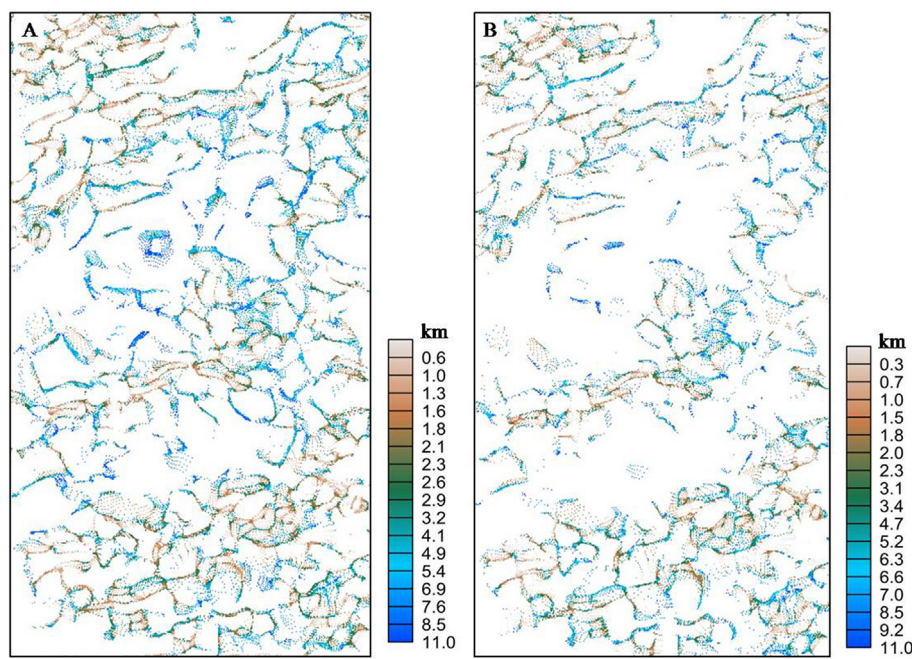


Fig. 8. (A) Euler3D deconvolution solutions of gridded aeromagnetic data using a structural index of 0.5 and window size 10. (B) Euler3D deconvolution solutions of gridded aeromagnetic data using structural index 1 and window size 10.

buried depth of the magnetic basement is generally less than 2 km to the north of the Jiashan–Xiangshui fault belt, where the depth is gradually shallower from south to north. It is inferred that the magnetic basement is composed of exposed Archean and Paleoproterozoic metamorphic rocks. In the southern Wunansha Uplift, the magnetic basement is also buried shallower with depths varying from 1 km to 1.5 km. Here, the basement is interpreted to be composed of a variety of magmatic rocks encountered in Paleo–Mesoproterozoic strata. In contrast, the magnetic basement is generally buried deeper in the middle South Yellow Sea, corresponding to around zone of high magnetic anomalies.

The central strong magnetic basement, covering an area of approximately 60,000 km², is surrounded by a lower gradient magnetic field, shown in Fig. 10A. Based on comprehensive analysis of the physical properties measured from onshore rock samples described in Section 2, we deduce that the central strong magnetic basement is formed of Archaeozoic and Proterozoic deep metamorphic rocks, which are composed of dramatically transformed pre-Sinian magmatic rocks. In general, the magnetic basement depths in Fig. 10B are large in the middle with depths varying from 4 km to 10 km. In contrast, surrounding the middle strong magnetic crystallized basement, the gentle low value anomalies are probably induced by shallow folded basement of Middle and Late Proterozoic strata. Thus, the character of the central magnetic field reflects the high stability of the stiff crystalline

basement.

5.2. Indosinian suture

The Indosinian suture is an unconformity between the Mesozoic–Cenozoic terrestrial strata and Paleozoic–Mesozoic marine strata, which is also the most significant density contrast layer in South Yellow Sea. In our study, we obtained the complete distribution of the Indosinian suture (Fig. 7B) in the South Yellow Sea and its western onshore-offshore transition zone using airborne gravity data, which has significant implications for the identification of the stages of marine sedimentary development. The depth inversion result (Fig. 7B) shows the undulating distribution of the Indosinian suture in the north–south direction. In general, the buried depth of the Indosinian suture is much greater in the northern and southern depression zones, at depths of approximately 2 km–6 km, while it is shallower in the Middle and Wunansha uplift zones, at approximately 1 km–2 km. Here, the calculated depth of the Indosinian suture based on the airborne gravity was proved to be reliable and concur with previous seismic exploration results. In addition, well CSDP-2 (Guo et al., 2017) in the Middle Uplift zone has encountered the Lower Triassic Qinglong Formation at a depth of 600 m, which also verifies the shallower burial depth of the Indosinian suture.

Furthermore, the Indosinian suture also provides an important

Table 2

Comparison of the depth (in m) of the top of the marine strata determined by drilling and calculations using the airborne gravity data.

Drilling number	Drilling location	Depth to top of marine strata		Deviation (m)	Relative error (%)
		Drilling (m)	Gravity data (m)		
ZC7-2-1	Northern Depression	1200	1410	210	17.50
CZ24-1-1	Southern Depression	3341	3396	55	1.65
WX4-2-1	Southern Depression	2708	2579	-129	-4.76
WX5-ST1	Southern Depression	1410	1620	210	14.89
CZ35-2-1	Wunansha Uplift	2077	1758	-319	-15.36
HH2	Northern Depression	1706	1720	14	0.82
WX13-3-1	Southern Depression	2805	2706	-99	-3.53
CZ12-1-1	Southern Depression	2077	2486	409	19.69

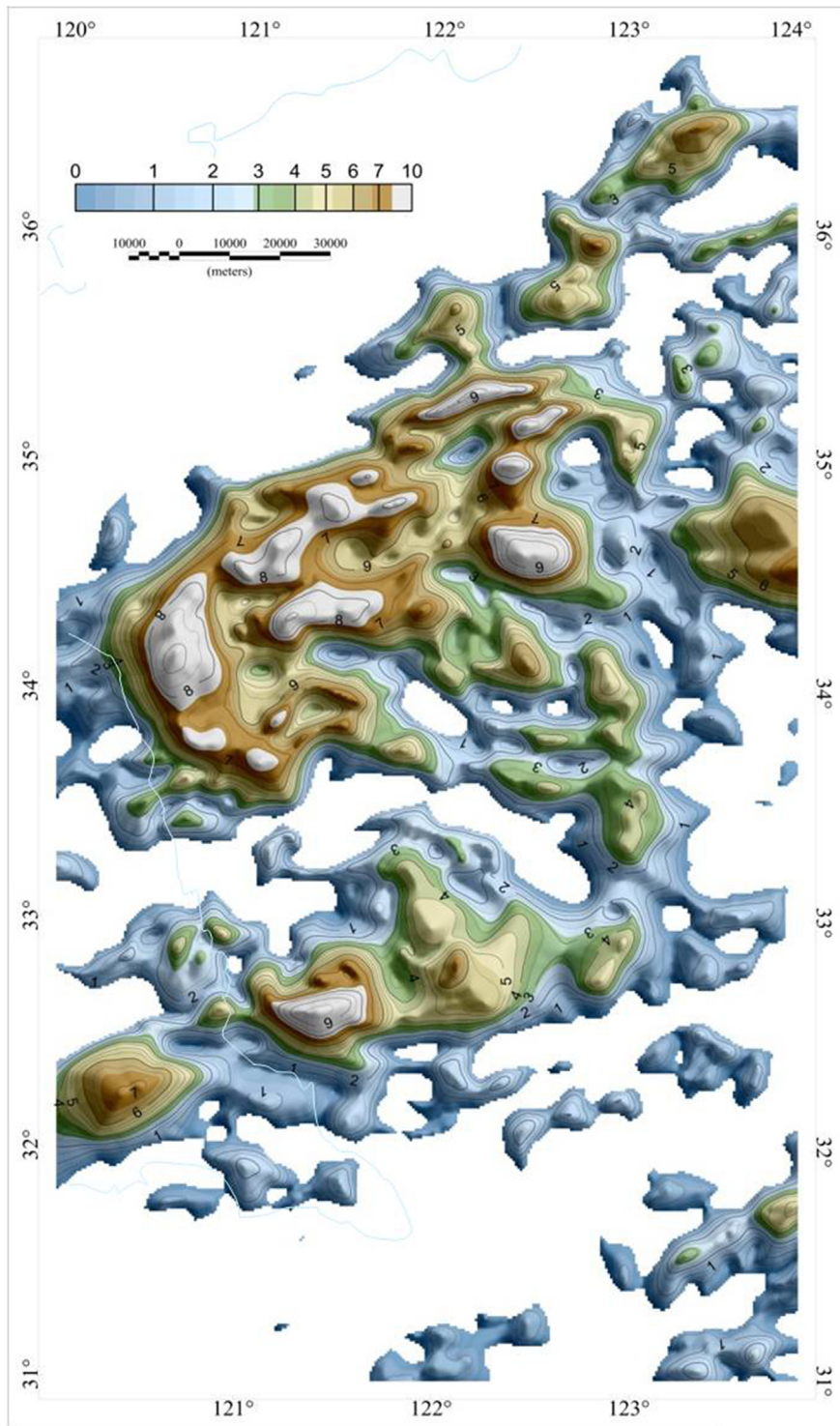


Fig. 9. Thickness distribution (in km) of the Paleozoic–Mesozoic marine strata of South Yellow Sea. (For interpretation of the references to color in this figure legend, the reader is referred to the Web version of this article.)

reference for the delineation of Cenozoic structural units. Previous research mainly depended on seismic data to determine the boundary of the Southern Depression of the South Yellow Sea. However, these previous works failed to identify the western trend of the boundary of the basin, nor to clearly illustrate structural relationship of the Southern Depression with the Subei Basin due to a lack of offshore data. Our study indicates that the high and low gravity anomalies correspond well with the Cenozoic sag and swell of the Northern and Southern depression zones, as shown in Fig. 3B. We found that a NW-trending fault

belt (Fig. 11) exists in the western onshore-offshore transition zone and controls the Cenozoic and Mesozoic sedimentation. Under the control of this NW-trending fault, the Cenozoic and Mesozoic sedimentary depression in the Subei Basin is obviously wider in the north–south direction, and the morphology of local sags are also considerably different from those offshore. In contrast, the sedimentary sags in the Southern Depression belong to a narrow strip faulted basin with a nearly east–west trend, and the sedimentary sags offshore are relatively gentle and wide, presenting a structural framework of sags and swells.

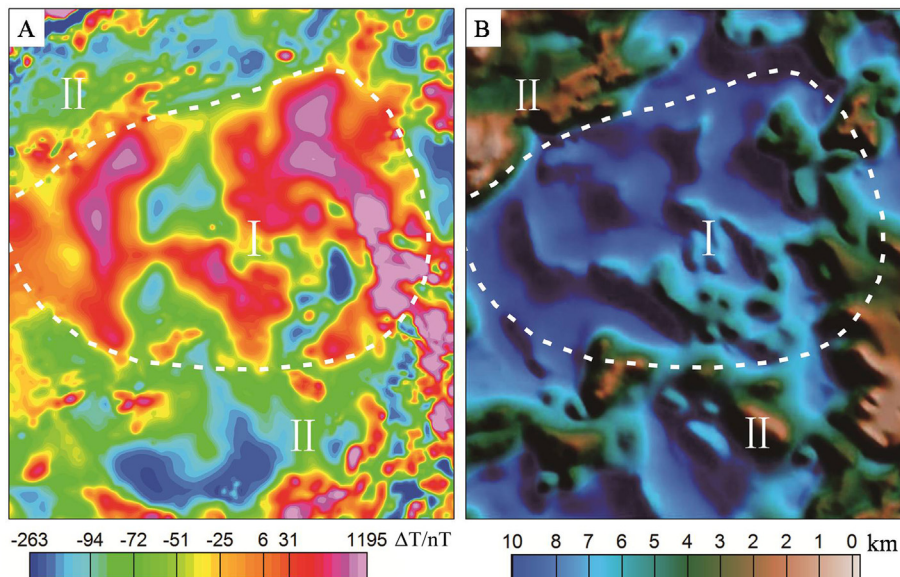


Fig. 10. (A) Color intensity plot of the middle strong magnetic basement anomaly. (B) Gridded depth of burial of the middle strong magnetic basement. I. Archaeozoic and Proterozoic deep metamorphic basement. II. Middle and Late Proterozoic folded basement. (For interpretation of the references to color in this figure legend, the reader is referred to the Web version of this article.)

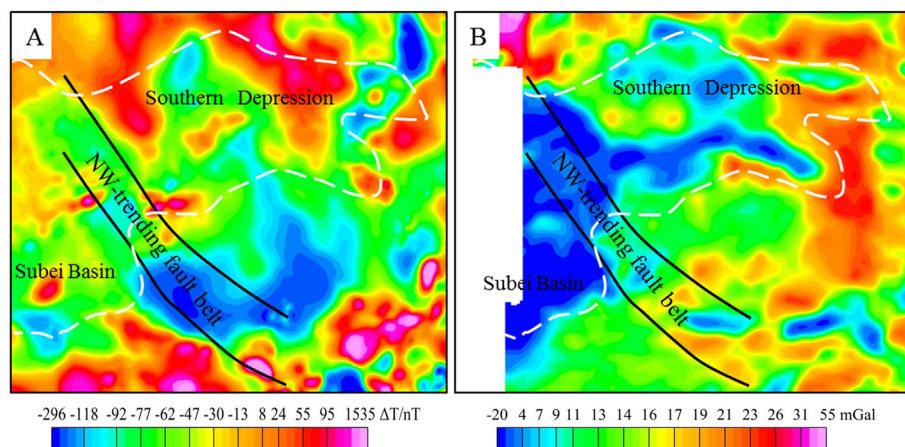


Fig. 11. The NW-trending fault belt in South Yellow Sea interpreted by the aeromagnetic and airborne gravity data. (For interpretation of the references to color in this figure legend, the reader is referred to the Web version of this article.)

These sags and swells within the Southern Depression are suddenly cut off by the NW-trending fault in the sea.

In general, the Indosinian suture is buried shallow in the Middle Uplift along an east – west trend, except in some local areas. The current structural framework of the Middle Uplift was formed as a result of the Indosinian and early Yanshanian orogenies. In addition, under the control of the regional north – south-trending stress (Wang et al., 2014), the strata of the Middle Uplift was successively uplifted and folded during the Paleozoic, suffering large-scale serious denudation during the early Yanshanian orogeny, thereby forming large-scale thrust fault-related structures and an unconformable contact between the Cenozoic – Mesozoic and Paleozoic strata.

5.3. Marine strata

The Mesozoic and Cenozoic tectonic framework of South Yellow Sea has been made and known for many years. However, it is difficult to divide the Paleozoic and Mesozoic tectonic units for shortage of seismic data. According to the distribution of the Paleozoic and Mesozoic marine strata, combining the magnetic basement depth and other known geological materials of South Yellow Sea, the preliminary subdivision of Paleozoic and Mesozoic tectonic units is conducted in this study. As shown in Fig. 12, the Paleozoic and Mesozoic tectonic

framework of the South Yellow Sea can be divided into four Grade I tectonic units from north to south: the Jiaonan Uplift area, the Subei-South Yellow Sea Depression area, the Southern Uplift area, and Wunansha Uplift area. The Subei-South Yellow Sea Depression area with large-scale northeast-southwest-trending distributions of marine strata, can be subdivided into five Grade II tectonic units: the Northern Depression, Eastern Depression, Middle Depression, Southern Uplift and Subei Depression. The Middle Depression is identified to be the main tectonic unit of marine sediments in Subei-South Yellow Sea Depression area with thickness of marine strata varying from 3 km to 10 km. The Southern Depression also has much widely distributed marine strata with maximum thickness up to 5–6 km. In contrast, the marine strata of the Northern Depression, Eastern Depression, and Subei Depression are relatively locally distributed, which is probably due to the intensive tectonic movements during Indosinian and Yanshanian orogeny. In addition, the Southern Uplift is inferred to be the Paleozoic marine sediments missing area as a result of uplifting and denudation.

Compared with the distribution of strata onshore in the lower Yangtze, the Paleozoic and Mesozoic marine strata in the South Yellow Sea are very different in terms of their thicknesses, scales, and tectonic movements. The marine strata onshore in the lower Yangtze region become thinner but still have a large residual thickness in the Rugao area. Based on the known geo-seismic data, the thrust faults and ramp

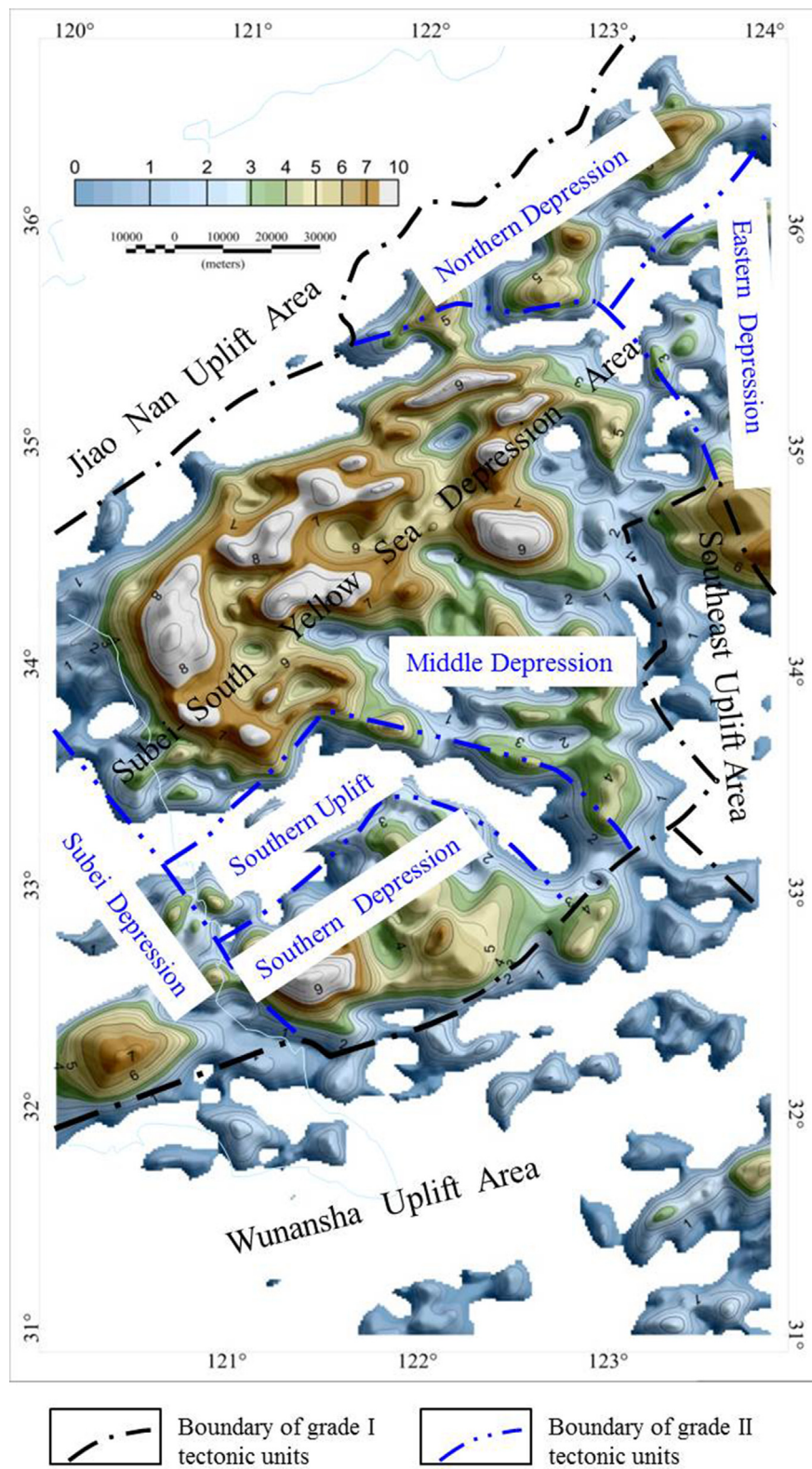


Fig. 12. The Paleozoic-Mesozoic tectonic division and marine strata distribution of South Yellow Sea. (For interpretation of the references to color in this figure legend, the reader is referred to the Web version of this article.)

structures are widely developed onshore in the lower Yangtze region, and overturns and recumbent folds are also developed. In contrast, the seismic data show much flatter and simpler folds of the Paleozoic and Mesozoic marine strata (Fig. 13). In addition, the four drilling sites that encounter the marine strata of the South Yellow Sea also verified a

more complete Triassic succession than those onshore. Only CZ12-1-1 presents a repeating and overturning phenomenon of the strata, but the three other wells showed the normal strata order. Therefore, it can be inferred that the tectonic movement of the South Yellow Sea was weaker than that in the Subei Basin, which favors the preservation of

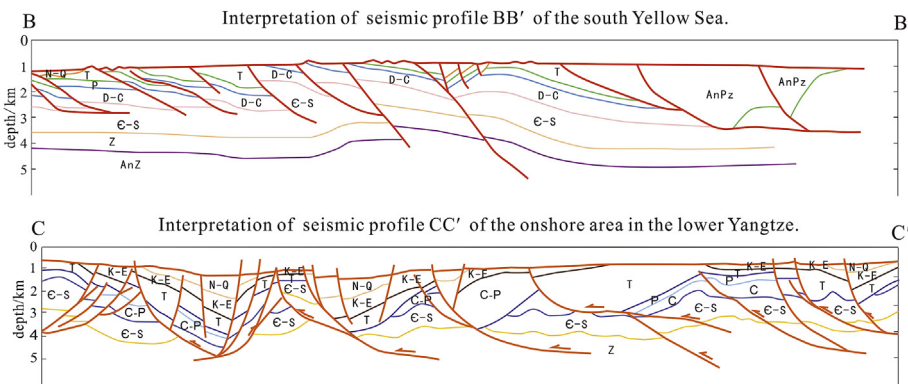


Fig. 13. Comparison of deformation characteristics of Mesozoic and Paleozoic marine strata onshore and offshore area in the lower Yangtze(modified after Xu et al., 2014). The locations of profile BB'and CC'are shown in Fig. 1.

the Paleozoic and Mesozoic marine strata.

The China Geological Survey conducted the Chinese Continental Scientific Drilling Project in the middle uplift of the South Yellow Sea to aid in fundamental geological research in 2015, identifying seven oil- or gas-bearing sections using CSDP-2 drilling, with approximately 100–280 m thickness. These sections were preserved under more than 600 m of marine strata, including the late Triassic, Permian, Carboniferous, and Devonian. The drilling proved that the marine strata of the South Yellow Sea have significant hydrocarbon potential, especially in the Middle Uplift of the South Yellow Sea. Thus, based on the results of this study, the Middle Uplift should be considered as a key oil and gas target because of its thick and stable marine sediments.

Acknowledgments

This work has been supported by the Aero Geophysical Prospecting and Application for Marine Geology Project of the China Geological Survey (Grant No. GZH200900502) and the Marine Geological Survey of the Fundamental and Public Welfare Project of the China Geological Survey (DD20160141). We are grateful to the anonymous reviewer and editor for their helpful comments and suggestions that have greatly improved our manuscript. We thank the China Aero Geophysical Survey and Remote Sensing Center for their permission to release the data.

References

- Cai, Q.Z., 2002. Regional geology and geotectonic environment of petrolierous basins in the Yellow Sea. *Mar. Geol. Lett.* 18, 8–12 (In Chinese with English abstract).
- Chen, J., Gong, J., Gang, L.I., Huijun, L.I., Yuan, Y., Zhang, Y., 2016. Great resources potential of the marine Mesozoic–Paleozoic in The South Yellow Sea basin. *Mar. Geol. Front* 32, 1–7 (In Chinese with English abstract).
- Dai, Q.F., Zhou, L.Y., Wei, H.L., 2002. Satellite gravity field and tectonic evolution of the South Yellow Sea. *Mar. Geol. Quat. Geol.* 22, 67–72 (In Chinese with English abstract).
- Deng, D., Ou, Q., 1995. Geophysical prospecting for petroleum in marine carbonate areas of the lower Yangtze region of southern China. *Geophysics* 60, 1306–1312.
- Grimmer, J.C., Jonckheere, R., Enkelmann, E., Ratschbacher, L., Hacker, B.R., Blythe, A.E., 2002. Cretaceous–Cenozoic history of the southern Tan-Lu fault zone: apatite fission-track and structural constraints from the DaBieShan (eastern China). *Tectonophysics* 359, 225–253.
- Guo, X.W., Zhu, X.Q., Mo, L., Xu, Y., Pang, Y.M., Cai, L.X., et al., 2017. Discovery of Permian-Triassic ammonoids in the central uplift of the South Yellow Sea and its geological implications. *Mar. Geol. Quat. Geol.* 37, 121–128 (In Chinese with English abstract).
- Guo, Y., Li, Y., Xu, D., Liu, X., Zhang, X., 1997. Tectonic evolution of theYellow Sea, East China Sea and continental shelf and adjacent areas. *Mar. Geol. Quat. Geol.* 17, 1–12 (In Chinese with English abstract).
- Hou, F., Tian, Z., Zhang, X., Zhang, Z., Li, S., 2012. In: Joint Inversion of Gravity Magnetic and Seismic Data of the South Yellow Sea Basin, vol.47. OGP, pp. 815–821 (In Chinese with English abstract).
- Hao, T.Y., Huang, S., Xu, Y., Li, Z., Zhang, L., Wang, J., Suh, M., Kim, K., 2010. Geophysical understandings on deep structure in yellow sea. *Chin. J. Geophys.* 53, 1315–1326.
- Keating, P., Pinet, N., 2011. Use of non-linear filtering for the regional-residual separation of potential field data. *J. Appl. Geophys.* 73, 315–322.
- Lee, G.H., Kim, B., Shin, K.S., Sunwoo, D., 2006. Geologic evolution and aspects of the petroleum geology of the northern East China Sea shelf basin. *Am. Assoc. Petrol Geol. Bull.* 90, 237–260.
- Liu, K., Liu, H., Wu, Z., Long, Y., 2016. Seismic acquisition parameters analysis for deep weak reflectors in the South Yellow Sea. *J. Ocean Univ. China* 15, 758–766.
- Li, Q., Li, Q.C., Jing, Y.H., 2014a. The varying inclination method for magnetic reduction to the pole. *Prog. Geophys.* 29, 1487–1502 (In Chinese with English abstract).
- Li, W., Liu, Y., Xu, J., 2014b. Onshore-offshore structure and hydrocarbon potential of The South Yellow Sea. *J. Asian Earth Sci.* 90, 127–136.
- Lin, Z., Yao, Y.J., 2009. Garvity-magnetic-seismic inversion and integrated interpretation of a typical section in the South Yellow Sea. *Geophys. Geochem. Explor* 33, 359–361 (In Chinese with English abstract).
- Liang, J., Zhang, P.H., Chen, J.W., Gong, J.M., Yuan, Y., 2017. Hydrocarbon preservation conditions in Mesozoic–Paleozoic marine strata in The South Yellow Sea basin. *Nat. Gas. Ind.* 37, 10–19 (In Chinese with English abstract).
- Liang, R., Pei, Y., Zhang, Y., Wei, J., Liu, Y., 2003. Gravity and magnetic field and tectonic structure character in the southern Yellow Sea. *Sci. Bull.* 48, 64–73.
- Luo, D., Zhang, X., Cai, F., Liu, Z., Zhang, Z., Hou, F., 2014. Integrated gravity-magnetic-seismic data inversion and interpretation and their application to underwater tectonics. *Mar. Geol. Quat. Geol.* 34, 135–143 (In Chinese with English abstract).
- Ouyang, K., Zhang, X., Gang, L.I., 2009. Characteristics of stratigraphic distribution in the middle uplift of the South Yellow Sea. *Mar. Geol. Quat. Geol.* 29, 59–66 (In Chinese with English abstract).
- Pang, Y., Zhang, X., Xiao, G., Wen, Z., Guo, X., Hou, F., Zhu, X., 2016. Structural and geological characteristics of The South Yellow Sea basin in the lower Yangtze block. *Geol. Rev.* 62, 604–616.
- Qi, J., Wen, Z., Zhang, X., Fang, N., Guo, X., 2013. Lithostratigraphic correlation of mesozoic and paleozoic marine strata between The South Yellow Sea and the upper Yangtze region. *Mar. Geol. Quat. Geol.* 33, 109–120 (In Chinese with English abstract).
- Qi, J., Zhang, X., Wu, Z., Qiu, X., Zhao, M., Xia, S., Guo, X., Hao, T., Zhang, Y., Fang, N., 2015. Preliminary results of the South Yellow Sea OBS 2013 onshore-offshore joint deep seismic survey. *J. Trop. Oceanogr.* 34, 76–84.
- Ren, J., Tamaki, K., Li, S., Junxia, Z., 2002. Late Mesozoic and Cenozoic rifting and its dynamic setting in Eastern China and adjacent areas. *Tectonophysics* 344, 175–205.
- Shinn, Y.J., 2015. Geological structures and controls on half-graben inversion in the western Gunsan Basin, Yellow Sea. *Mar. Petrol. Geol.* 68, 480–491.
- Shinn, Y.J., Chough, S.K., Hwang, I.G., 2010. Structural development and tectonic evolution of the gunsan basin (Cretaceous–Tertiary) in the central Yellow Sea. *Mar. Petrol. Geol.* 27, 500–514.
- Sparker, G.J., 1963. Standard curves for interpretation of magnetic anomalies over long tabular bodies. *Geophysics* 161–200 XXVIII.
- Sun, J., Wang, J., Xiao, G., Wu, Z., Li, S., 2014. Distribution pattern of marine upper structural layer and fault system on the central uplift of the South Yellow Sea basin. *Mar. Geol. Front* 30, 18–25 (In Chinese with English abstract).
- Vacquier, V., Steenland, N.C., Henderson, R.G., Zietz, I., 1951. Interpretation of Aeromagnetic Maps. *Geological Society of America Memoir* 47.
- Wang, M., Wang, L.F., He, H., 2015. The application of the matched filtering technology to the separation of gravity field sources. *Geophys. Geochem. Explor.* 39, 126–132 (In Chinese with English abstract).
- Wang, M.J., Zhang, X.H., Wu, Z.Q., Xiao, G.L., Wang, J., Wang, A.G., 2014. Tectonic evolution of southern depression in the South Yellow Sea basin and its hydrocarbon accumulation in Permian. *J. China Univ. Min. Technol.* 43, 271–278 (In Chinese with English abstract).
- Wang, Q., An, Y., 2000. The features of gravity field and deep structure in western part of the South Yellow Sea. *Sci. Bull.* 45, 759–764.
- Wu, S., Ni, X., Cai, F., 2008. Petroleum geological framework and hydrocarbon potential in the Yellow Sea. *Chin. J. Oceanol. Limnol.* 26, 23–34.
- Xing, T., Zhang, X.H., Zhang, X.Y., 2014. Magnetic basement and structure of the southern Yellow Sea. *Oceanol.Limnol.Sin.* 45, 946–953 (In Chinese with English abstract).
- Xiong, S.Q., 2010. Theory, Method and Application of the Airborne Gravity Prospecting. Geological Publishing House, Beijing (In Chinese with English abstract).

- Xiong, S.Q., Ding, Y.Y., Li, Z.K., 2014. Characteristics of China continent magnetic basement depth. *Chin. J. Geophys.* 57, 3981–3993.
- Xu, X.H., Zhou, X.J., Peng, J.N., 2014. Exploration targets in southern Yellow Sea through analysis of tectono-depositional evolution and hydrocarbon accumulation of marine basin in the Yangtze area. *Petro. Geol. Exp.* 36, 523–545 (In Chinese with English abstract).
- Yao, Y., Xia, B., Feng, Z., Wang, L., Xu, X., 2005. Tectonic evolution of The South Yellow Sea since the paleozoic. *Pet. Geol. Exp.* 27, 124–128.
- Yuan, Y., Chen, J., Zhang, Y., Wu, S., Lei, B., Zhang, P., Sun, J., Wang, J., 2016. Geotectonic features of the marine mesozoic-paleozoic on the laoshan uplift of The South Yellow Sea basin. *Mar. Geol. Front* 32, 48–53 (In Chinese with English abstract).
- Yue, B., Jing, L., Hong, L., Zhang, H., 2014. East boundary of the collision belt between Sian-Korean and Yangtze plates in eastern China and their extension in the sea. *Mar. Geol. Quat. Geol.* 34, 75–85 (In Chinese with English abstract).
- Zhang, M., Xu, D., Chen, J., 2007. Geological structure of the Yellow Sea area from regional gravity and magnetic interpretation. *Appl. Geophys.* 4, 75–83.
- Zhang, X., Yang, J., Li, G., Yang, Y., 2014. Basement structure and distribution of Mesozoic–Paleozoic marine strata in The South Yellow Sea basin. *Chin. J. Geophys.* 58, 96–107.
- Zhu, Y., 2012. Tangent and Diagram Methods for Analysis of Dip Magnetized Models. Geological publishing house, Beijing.

The Quantitative Inversion of Iron Ore under Strong Constrain in Panzhihua-Baima Districts in Sichuan Province Based on the High-Precision Aeromagnetic Survey

Tengfei Ge^{1,2*}, Jingzi He^{1,2}, Xue Yang² and Xuzhao Huang²

¹China University of Geosciences(Beijing);

²China Aero Geophysical Survey&Remote Sensing Center of land and resources.

Email:564465031@qq.com

Keywords: Magmatic iron ore, inversion, Panzhihua layered intrusion, South-West China

Abstract: The PanXi region in Sichuan province, Sounthwest China is famous for magmatic Fe-Ti-V oxide deposits in the country. The metallogenesis of the Panzhihua type V-Ti magnetite deposits remains controversial. Here we apply an interactive inversion technique on profiles of magnetic anomalies to study the deep geological structure of the Baima area. Combined with previous petrological and sedimentological studies on these rocks, the inversion results indicate that Baima iron deposits consist of several layered iron ore bodies. Different characteristics in the geometric forms of Panzhihua rock body and Baima rock body show different mineralization characters when forming magnetite ore layers under the gravity variation, resulting in different ore structures. Although the large aeromagnetic anomaly could be the signal of the buried huge iron ore bodies at depth in Panxi area, this has not been confirmed by deep drilling exploration. In order to solve this puzzle, we computed the aeromagnetic anomalies along profiles in the proven iron deposits of the Baima districts. The results reveal marked contrast between the calculated and observed anomalies. Based on these results and previous studies on the metallogenic features, we predict the presence of large iron ore bodies at depth beneath the Baima districts.

1 INTRODUCTION

The PanXi region has several large mafic-layered intrusions that host world-class Fe-Ti-V oxide deposits, such as the Panzhihua Fe-Ti-V deposit and Baima Fe-Ti-V deposit that form part of the ~260 Ma Emeishan Large Igneous Province. This region have attracted interest over the last decade because of their association with ore deposits(Zhou et al 2008) (Shellnutt et al., 2010) and the Panzhihua Fe-Ti-V oxide mine makes China a major producer of V and Ti, accounting for 6.7% and 35.2% of the total world production of V and Ti, respectively (Zhou et al., 2005).

Several models have been proposed for the formation of the Panzhihua deposit that are related to the Emeishan large igneous province (LIP): (1) the Panzhihua ore bodies developed concentrations of Fe and Ti through the fractional crystallization of ferrobasaltic or ferropicritic magmas, followed by separation into silicate magma and Fe-rich oxide ore melt (Zhou et al., 2005); (2) early crystallization of

Fe-Ti oxides from a parent magma with 1.5 wt.% H₂O and oxide accumulated through crystal setting at the base of the intrusion (Pang et al., 2008; Zhou et al., 2008); and (3) an increase in magma fO₂ related to the CO₂-degassing of the footwall carbonates resulted in the accumulation of Fe-Ti oxides (Ganino et al., 2008) .The Fe-Ti oxides had crystallized at an early stage of the solidification of the Panzhihua intrusion, in consideration of an effective accumulation of titanomagnetite in the Panzhihua intrusion (Ganino et al., 2008).

Although the depth of exploration conducted so far is shallow, there are some clues to indicate the presence of greatly potential iron ores at depth in the Panzhihua-Xichang area. He have suggested that the known deposits may not have appeared in their overlapping anomaly regions of 1:50,000 ΔT reduced-to-pole upwards vertical second derivative and ΔT reduced-to-pole downwards continuation ,the 3D model of Hongge Fe-Ti-V deposit was also built under the constrain of the drilling profiles and high- precision aeromagnetic data(Ganino and Arndt,

2009). Ge suggested that the deep levels beneath the Daheishan and Minzhengxiang districts are benefit space for future prospecting (Ge et al. 2015).

The interactive inversion technique on profile of magnetic anomalies is a new method that can be used to infer the depth and attitude of deeply buried ore bodies through geophysical data inversion, and has been successfully applied for the prediction of several iron ore bodies (Fan et al., 2010, 2012; Yu et al., 2007). To evaluate the possibility of deep iron ore bodies in these areas, we conducted 15 magnetic inversion lines across both Panzhihua area and Baima area, among them 10 magnetic inversion lines in Panzhihua area and 6 magnetic inversion lines in Baima area proved to be of obvious ore prospecting potential. The results from the inversion aid in evaluating the possibility of the presence of deep iron ore bodies and understanding the distribution of iron ore bodies in the Panzhihua-Baima area.

2 GEOLOGICAL SETTING

Numerous papers have described the geological setting of the ~260 Ma Emeishan Large Igneous Province and the large mafic-ultramafic intrusions that are considered to be part of the plumbing system of the Emeishan flood basalt (Zhou et al., 2008). The Emeishan magmas intruded sedimentary rocks of the Sichuan basin. In the Panxi region, uplift and erosion has exposed large mafic-ultramafic intrusions that are considered to be part of the plumbing system of the Emeishan flood basalts (Figure 1).

The Panzhihua gabbroic intrusion dips 50~60° NW and extends about 19 km along strike. The majority of the wall rocks are Neoproterozoic (Sinian) dolostones (Figure 2a). These rocks are almost pure and most contain very low contents of clay and silica minerals, but they are interbedded with siliceous limestones, marlstones and shales (Pêcher et al. 2013).

From stable isotope analyses, Ganino estimated that the Panzhihua gabbro assimilated 8~13.7 wt.% of carbonate wallrock (Ganino et al., 2013), and provided preliminary descriptions of the marbles and skarns and explained how carbon dioxide released during the metamorphism may have triggered both the ore formation and global climate change (Ganino et al., 2008). Magnetite-rich melanogabbro at the base grades through normal gabbro to leucogabbro near the top. The large Fe-Ti-V oxide ore deposits occur as magnetite-rich

cumulate layers or discordant lenses along the southeast margin of the intrusion. The contact aureole is >300 m thick and is mostly composed of brucite marble that formed from the thermal metamorphism of dolostones, and various calc-silicate rocks (olivine, diopside or garnet bearing marbles) that formed from marly layers. Banded carbonate-serpentinite reaction rims, “zebra-rocks”, surround small dolerite dykes that were probably the early intrusions associated with the emplacement of Panzhihua magma.

The Baima mafic layered intrusion is located in the central part of the Panxi area, SW China (Figure 1). The N-S striking intrusion is 24 km long and 2 km wide, dips to the west in 50–70°, and is emplaced into the Sinian metamorphic sandstone, phyllite, slate and marble (Figure 3). After emplacement, the Baima intrusion was surrounded and cut by ~259 Ma syenitic intrusions and dykes (Zhang, et al., 2012). In addition, several NW-SE-trending faults separate the Baima intrusion into five segments, including Xiajiaping, Jijiping, Tianjiacun, Qinggangping and Mabinglang (Figure 3). Along the strike, the Baima intrusion shows a thickness gradation from a more primitive facies in the north to a more evolved thinner facies in the south. The magnetite ore reserve of Baima intrusion is 1497 Mt (millionton) with mean grades of ~26% total Fe, ~7% TiO₂ and ~0.21% V₂O₅ (Zhang, et al., 2012).

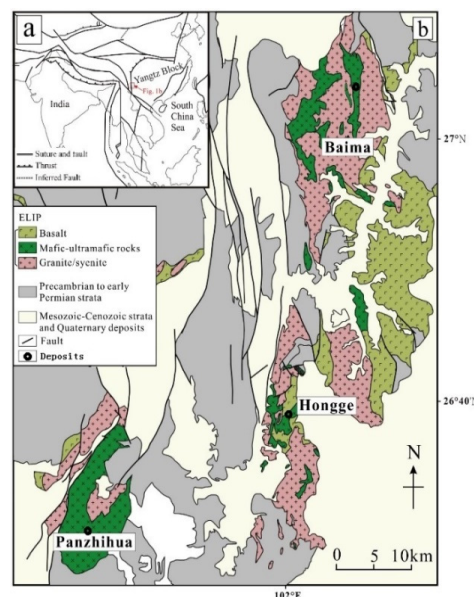


Figure 1: Simplified regional geology of the Panxi area, Emeishan large igneous province, SW China, showing the distribution of Panzhihua, Hongge and Baima mafic-ultramafic intrusions that host Fe-Ti-(V) oxide ore.

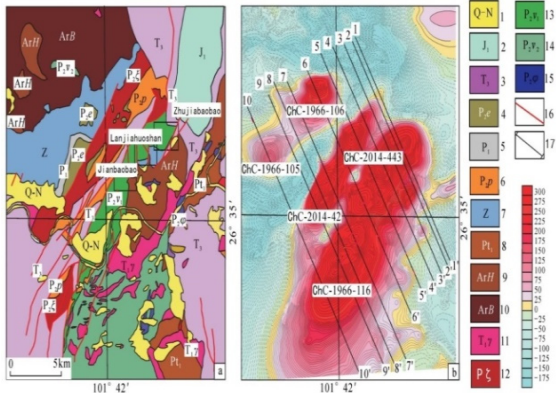


Figure 2: (a) Geological map of the Panzhihua area.; (b) aeromagnetic anomalies in the Panzhihua area; 1 - Quaternary~Neogene; 2 - Lower Jurassic; 3 - Upper Triassic; 4 - Middle Permian (Emeishan basalt); 5 - Lower Triassic; 6 - Middle Triassic phonolite; 7 - Sinian limestone and marble; 8 - Kangding complex Pianjiangtian unit; 9 - Kangding complex Huatan unit; 10 - Kangding complex Bude unit; 11 - Early Triassic granite; 12 - Permian Syenite; 13 - Middle Permian gabbro (containing seam); 14 - Middle Permian gabbro and dioritic; 15 - Middle Permian pyroxenite; 16 - Faults; 17 - Inversion profiles(5 low potential profiles in the northern part are not mentioned).

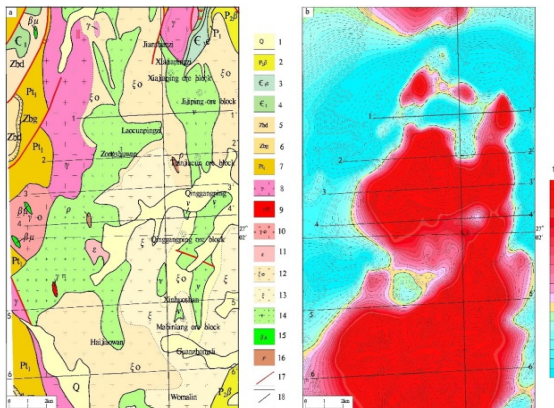


Figure 3. (a) Geological map of the Baima area.; (b) aeromagnetic anomalies in the Baima area; 1 - Quaternary; 2 - Middle Permian (Emeishan basalt); 3 - Upper Cambrian; 4 - Lower Cambrian; 5 - Sinian Dengying Formation; 6 - Sinian Guanyinya formation; 7 - Lower Proterozoic; 8 - Granite; 9 - Granite porphyry; 10 - Plagiogranite; 11 - Huangcao Syenite; 12 - Quartz syenite; 13 - Baima Syenite; 14 - Gabbro; 15- Dolerite; 16 - Diorite; 17- Faults; 18- Inversion profiles(9 low potential profiles in the southern part of this area are not mentioned).

3 GEOPHYSICAL SETTING

3.1 Characteristics of Magnetic Anomalies

On the 1:50,000 contour map of the aeromagnetic ΔT in Baima area (Figure 3b), several anomalies with an intensity 775~ 1200 nT is identified in the Baima area ,known iron ore belts is located along the S-N high magnetic anomaly zone. According to the contour map of the aeromagnetic ΔT , the area of the high magnetic anomalies is much larger than the iron ore belts. From Laocupingzi to Womalin where iron deposits have not been found, the intensity of the aeromagnetic anomalies is more than 1000nT.

3.2 Physical Properties of Rocks and Ores

We measured the physical properties of selected iron ores, the ore bearing layers and cover strata, and the statistical results are listed in Table 1. The susceptibilities of the metamorphic rocks, sedimentary rocks and are in the range of $(0\sim 10) \times 10^{-5}$ SI, which can be generally regarded as non-magnetic. Gabbro (the ore bearing layer) shows a much higher susceptibility of $(11,768.79\sim 116.99) \times 10^{-5}$ SI. The susceptibilities of the iron ore are in the range of $(129,000\sim 20,499) \times 10^{-5}$ SI, which is a geological body that could cause a strong magnetic anomaly in this area, with densities in the range of $3.1\sim 4.2 \text{ g/cm}^3$.

Removing errors in measurement ,the relationship between Susceptibility and Ore grade is positive correlation (Sun et al,1991; Tian et al,2013).We conducted magnetic susceptibility measurement and optical film identification upon 30 magnetite samples (Figure 4) from Panzhihua deposit and Baima deposit , and the results indicated that the magnetic susceptibility can be used as the basis for the division of rich iron ores.

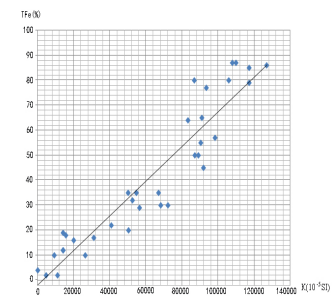


Figure 4. The relationship between susceptibility and ore grade in Panxi area.

Table 1: Physical properties of geological bodies.

Name	Number of measured points	Susceptibility(10^{-5} SI)			area
		Maximal value	Minimum value	Average value	
medium-grade ore	32	116000	38090	76541	Panzhihua area
high-grade ore	31	129000	55741	111521	Panzhihua area
Low-grade ore	34	113000	20063	61041	Panzhihua area
Submarginal ore	30	46062	20499	33618	Panzhihua area
Gabbro	38	6539	2865	4564	Panzhihua area
Gabbro	35	11768	116	6406	Panzhihua area(drill core)
Gabbro(ore bearing)	30	19014	3483	11286	Panzhihua area
Gray marble	33	10	0.2	0.7	Panzhihua area
Syenite	32	3357	1508	2243	Panzhihua area
Phonolite	32	4916	1815	3364	Panzhihua area
Basalt	30	5556	807	4186	Panzhihua area
Sandstone	31	12	0.4	5	Panzhihua area
granite gneiss	30	1244	98	560	Panzhihua area
granite	34	2011	104	1121	Panzhihua area
Pyroxenite	30	15905	6428	11075	Panzhihua area
Low-grade ore	31	89903	30004	59442	Baima area
high-grade ore	31	127000	20163	98134	Baima area
Gabbro(ore bearing)	32	26486	1063	9846	Baima area
Gabbro	36	10497	142	4983	Baima area
Gray marble	32	14	1.2	5.5	Baima area
Syenite	30	5669	2305	4323	Baima area
Basalt	30	5556	807	4057	Baima area
Granite	37	34	1	9	Baima area
dolomite	30	10.9	0.2	3.3	Baima area
Sandstone	31	11	1	3	Baima area
granite gneiss	32	53	2	14	Baima area

4 INTERACTIVE INVERSION TECHNIQUE OF MAGNETIC ANOMALIES ALONG THE UNDULATING TERRAIN PROFILE

Along undulating terrain profiles can be expressed in 2.5-D. The magnetic anomalies are calculated above the initial model with polygonal sections of level prism 2.5-D that are created on the basis of the known geological structures, the property data and semi-quantitative interpretation. Thereafter the model parameters continue to be adjusted until the calculated gravity and magnetic anomalies are

consistent with measured gravity and magnetic anomalies. Finally, based on these, we can understand some important information such as the depth, shape and volume of iron ore bodies (Fan et al., 2012).

Deep ore deposit prediction has been achieved by utilizing this technology (Cong et al., 2012; Fan et al., 2010, 2012; Yu et al., 2007). Yu noted that two iron ore bodies dipping to the south occur at 230–480 m and 630–880 m, with a horizontal distance of 200 m through the aeromagnetic anomaly inversion of Xiangbishan profile across Daye iron deposit in Hubei province, China. The borehole ZK21-8 exploration has successfully confirmed the inversion result (Fan et al., 2012) ,

several layered ore bodies with a total thickness of 14.6m at 40–45% Fe were found at a depth interval of 740–840 m, consistent with the above prediction.

4.1 Calculation Method for Magnetic Anomalies

The three-components of magnetic field for any point P (x, y, z) on the section of the level prism 2.5-D could be calculated by the formula (Fan et al., 2010):

$$H_{ax}(P) = -\sum_{i=1}^N \sin \varphi_i (J_x I_{1i} + J_y I_{2i} + J_z I_{3i}) \quad (1)$$

$$H_{ay}(P) = -\sum_{i=1}^N (J_x \sin \varphi_i - J_z \cos \varphi_i) I_{2i} \quad (2)$$

$$J_y (\sin \varphi_i I_{1i} - \cos \varphi_i I_{3i}) \quad (2)$$

$$Z_a(P) = -\sum_{i=1}^N \cos \varphi_i (J_x I_{1i} + J_y I_{2i} + J_z I_{3i}) \quad (3)$$

which can be further calculated as:

$$I_{ji} = P_{ji}(Y_2) - P_{ji}(Y_1), j = 1, 3 \quad (4)$$

$$P_{1i}(y) = \cos \varphi_i \ln \frac{R_i+y}{R_{i+1}+y} - \sin \varphi_i \left(\arctan \frac{U_{i+1}y}{w_i R_{i+1}} - \arctan \frac{u_i y}{w_i R_i} \right) \quad (5)$$

$$P_{2i}y = \ln \frac{u_i + R_i}{u_{i+1} + R_{i+1}} \quad (6)$$

$$P_{3i}(y) = \cos \varphi_i \ln \frac{R_i+y}{R_{i+1}+y} - \cos \varphi_i \left(\arctan \frac{U_{i+1}y}{w_i R_{i+1}} - \arctan \frac{u_i y}{w_i R_i} \right) \quad (7)$$

The magnetic anomaly of the total field is:

$$\Delta T(P) = H_{ax}(P) \cos I_0 \cos D_0 + H_{ay}(P) \cos I_0 \sin D_0 + Z_a(P) \sin I_0 \quad (8)$$

which can be further calculated as:

$$u_i = x_i \cos \varphi_i + Z_i \sin \varphi_i, u_{i+1} = x_{i+1} \cos \varphi_i + Z_{i+1} \sin \varphi_i \quad (9)$$

$$R_i = (x_i^2 + y^2 + z_i^2)^{1/2}, R_{i+1} = (x_{i+1}^2 + y^2 + z_{i+1}^2)^{1/2} \quad (10)$$

$$\varphi_i = \arctan \frac{z_{i+1}-z_i}{x_{i+1}-x_i} w_i = -x_i \sin \varphi_i + Z_{i+1} \cos \varphi_i \quad (11)$$

$$J_x = J \cos I_0 \cos D, J_y = J \cos I_0 \sin D, J_z = J \sin I_0$$

where, Io: geomagnetic inclination and Do:geomagnetic declination; i: prism corner number; N:prism side number; J: prism magnetization; I: prism magnetic inclination and D: prism magnetic declination. Because the formula applies to arbitrary points on the section, we infer

that it may be applied to almost all undulated terrains.

4.2 The Interactive Inversion Software

The interactive inversion software used in this study is called GMVPS (Sui et al., 2004). It simulates the underground geological conditions at deep level by creating a model or multiple models that consist of finite horizontal prisms with a section of arbitrary polygons. The corner number of the polygons may be added, reduced or moved based on the known geological structures and anomaly characteristics. In addition to inductive susceptibility, inductive magnetic inclination, inductive magnetic declination, residual magnetization, residual inclination, horizontal extension of the model and pattern of the polygonal section,some other relevant parameters, including geomagnetic field strength,geomagnetic inclination, geomagnetic declination, profile azimuth, are also entered and corrected in the dialog box. The computational curve above the model is updated in real time as the change of the model parameters (Fan et al., 2010). The shape of the model is terminated at the least difference between the calculated and measured anomalies. Thus,we can get the final model by an inversion result(Figure 5 as a example).The physical properties used in the software is given according to the physical properties measured (table 2).

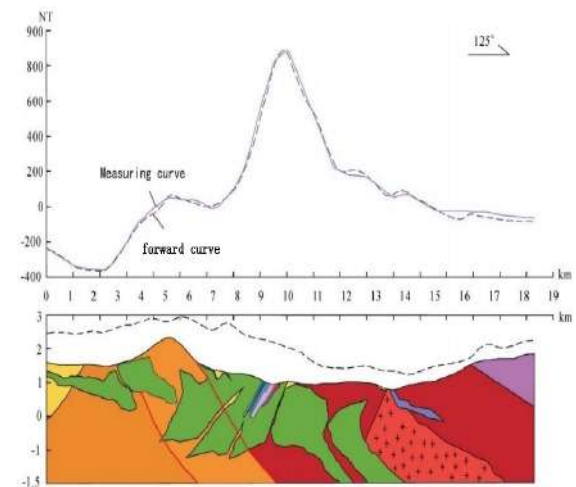


Figure 5: Aeromagnetic anomaly caused by the proven Panzhihua iron deposit along Panzhihua 4-4 profile (Figure legend refer to figure 7).

Table 2: Physical properties used in software.

Area	Name	Susceptibility $\kappa(10^{-5} \text{SI})$	Effective magnetization $\text{Js}(10^{-3} \text{A/m})$	direction of magnetization; $(^\circ)$	Density (10^3g/cm^3)
Baima area	Gabbro(ore bearing)	9840	3761.79	41.7	
	Gabbro	4983	1927.45	41.7	
	Gray marble and dolomite	5.5	2.2	41.7	
	Syenite(mixed with gabbro)	4320	1698.26	41.7	
	Syenite	1850	727	41.7	
	Basalt	4050	1552.81	41.7	
	Sandstone and siltstone	3	1.2	41.7	
	Archean and Proterozoic metamorphic rocks	14	5.6	41.7	
	Granite	9	3.6	41.7	
	High grade ore (more than 45%)	98100	37778.5	47	4.0
Panzhihua area	Low grade ore (<45%)	59442	23367.6	47	3.2
	Gabbro(ore bearing)	11200	4288.99	40.9	
	Gabbro	5600	2144.5	40.9	
	Pyroxenite	11075	4270	40.9	
	Gray marble and dolomite	0.7	0.3	40.9	
	Syenite	2243	857.79	40.9	
	Phonolite	3364	1286.7	40.9	
	Basalt	4486	1715.6	40.9	
	Sandstone and siltstone	5	2	40.9	
	Archean and Proterozoic metamorphic rocks	560	214.449	40.9	
	Granite	1121	428.99	40.9	
	grade I ore ($\text{TFe} \geq 45\%$)	111060	42890	53.0	4.2
	grade II ore ($44.9\% \geq \text{TFe} \geq 30\%$)	76500	30022	53.0	3.7
	grade III ore($29.9\% \geq \text{TFe} \geq 20\%$)	61000	23503.6	53.0	3.4
	Submarginal ore($19.99\% \geq \text{TFe} \geq 15\%$)	33600	12867	53.0	3.1

5 RESULTS

The parameters of the normal maetic field of the Panxi area used in the interactive inversion are the following: geomagnetic field strength = 48,202 nT,

geomagnetic inclination = 40.9° , geomagnetic declination = -1.4° , and profile azimuth = 125° (Panzhihua)/ 90° (Baima). The initial model is built on the basis of cross sections (Figure 6 and Figure 7 for example).

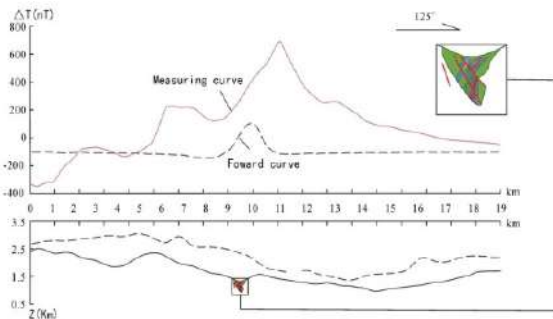


Figure 6: Aeromagnetic anomaly caused by the proven Panzhihua iron deposit along Panzhihua 4-4 'profile (Figure legend refer to figure 8).

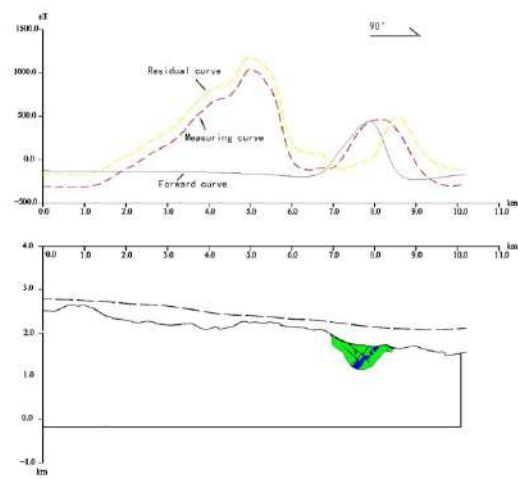


Figure 7: Aeromagnetic anomaly caused by the proven Baima iron deposit along Baima 2-2 'profile (Figure legend refer to figure 9)

5.1 Aeromagnetic Anomaly Caused by the Proven Panzhihua Iron Deposit

The salient features of the Panzhihua iron deposit (Figure 6 and Figure 8) are summarized as follows. The exploration depth is ~600 m. The ore body is ~200m thick, ~5000m long, and dips to the northwest at dipping angle of 50°. The wall rocks around the ore body are mainly Permian gabbro which intruded into Simian limestone and Archean gneiss.(Figure 6 and Figure 8).

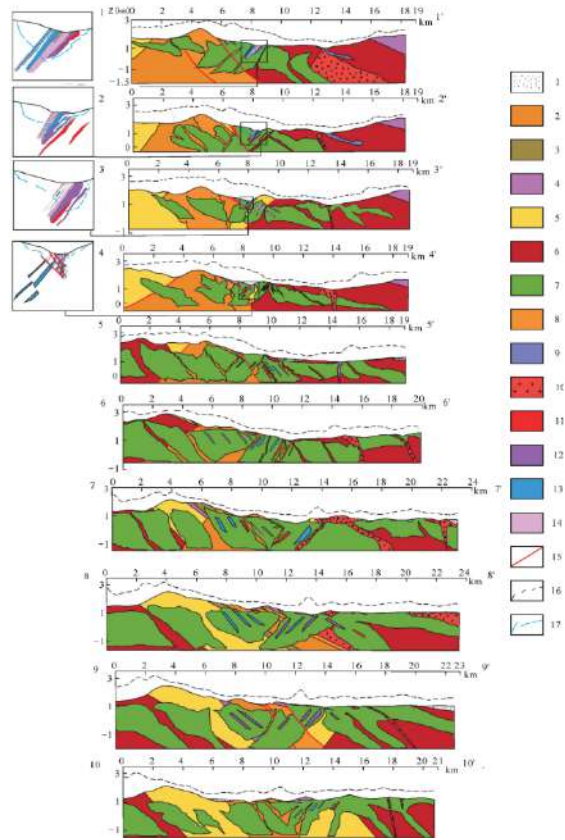


Figure 8: Inversion profiles 1~10 in Panzhihua area.

1- Quaternary; 2 - Permian phonolite; 3 - Permian basalt; 4 - Triassic sandstone; 5 - Simian limestone; 6 - Archean, Proterozoic metamorphic rocks; 7 - Gabbro; 8 - Syenite; 9 - Pyroxenite; 10 - Granite; 11 - Grade I ore ($TFe \geq 45\%$); 12 - Grade II ore ($TFe 30\sim 44.9\%$); 13 - Grade III ore ($TFe 20\sim 29.9\%$); 14 - Submarginal ore ($TFe 15\sim 19.9\%$); 15 - faults; 16 - Flight trajectory; 17 - Drilling controlled part.

On the basis of physical properties and aeromagnetic anomaly features, the aeromagnetic anomaly can be accomplished by running GMVPS, and is shown on the geological section of the proven Panzhihua iron deposit (Figure 6 and Figure 8). The physical properties of the rock and the ore data for modeling are listed in Table1 and shown in Figure 7.

5.2 Aeromagnetic Anomaly Caused by the Proven Baima Iron Deposit

The salient features of Baima iron deposit (Figure 7 and Figure 9) are summarized below. The exploration depth is ~430 m. The ore body is ~200 m thick, ~13000 m long(cut and translated by faults

into more than 5 ore blocks), and dips to the west at a dipping angle of 70° . The wall rocks around the ore body are mainly Permian gabbro (Figure 7 and Figure 9). We calculate the aeromagnetic anomaly of the Baima iron deposit via the abovementioned method (Figure 7 and Figure 9). The physical parameters of the rocks and ores for modeling are listed in Table 1 and shown in Figure 9.

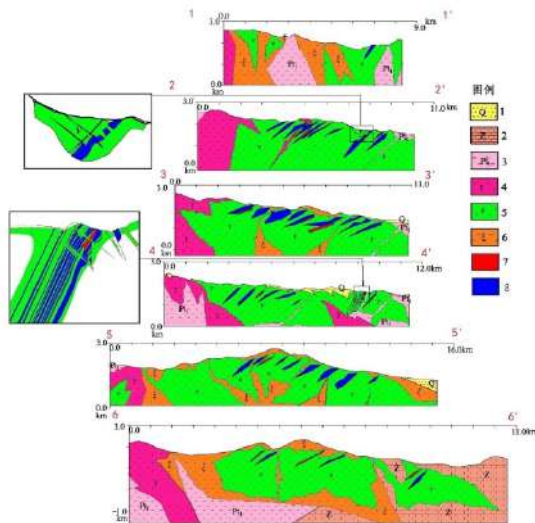


Figure 9: Inversion profiles 1~6 in Baima area(Cross sections were showed in the enlarged views)

1- Quaternary; 2 - Sinian limestone; 3 - Proterozoic; 4 - Granite; 5 - Gabbro; 6 – Syenite; 7 - Rich ore($\text{TFE} \geq 45\%$); 8 - Lean ore($\text{TFE} < 45\%$).

5.3 Results of Interactive Inversion on Magnetic Anomalies along Panzhihua and Baima Profiles

Based on the range of physical properties for rocks and ores in the Panzhihua and Baima area, we can get these physical parameters for modeling (Table 1). The parameters listed in Table 2 indicate magnetite ores are the strongest magnetic, and the ore-bearing layers (mainly gabbro) display the transition between non-magnetic or weakly magnetic limestone and syenite. However, the strength and the center position of magnetic anomalies significantly depend on the shapes of iron bodies. To obtain the best results, we corrected the models of the iron ore bodies constantly, until the residual anomaly between aeromagnetic fitting curve and the measured curve is the minimum. Consequently, when the aeromagnetic residual anomalies are the least, we can obtain the final model for Panzhihua and Baima profiles (Figure 8 and Figure 9).

6 DISCUSSION

6.1 Deep Mineral Exploration in the Panzhihua and Baima Area

Several magmatic Fe-Ti-V oxide deposits in the Panxi region, SW China, are hosted in layered mafic-ultramafic intrusions of the Emeishan Large Igneous Province(ELIP) (Figure 1) (Zhong et al., 2002; Zhou et al., 2005). Examples are the giant deposits of Panzhihua, Hongge and Baima. The Hongge deposit alone contains 4572 Mt of ore reserves with 1830 Mt of Fe, 196 Mt of Ti and 14.7 Mt of V (Ganino et al., 2013). In addition to these three giant deposits, other deposits currently being mined include the Taihe deposit to the north of the Baima deposit. In recent years, With the continuous development of the prospecting work ,several deposits, including Anyi , Mianhuadi and Wuben, were discovered.

Our investigation suggests that there are potential targets for iron ore exploration in the Baima area. As shown in Figure 6 and 7, the calculated aeromagnetic anomalies are much lower than the observed anomalies in Baima deposit. The similar scenario can also be seen in the other inversion lines in Panzhihua and Baima area (Figure 8 and Figure 9, curves were omitted). It suggests that there might be buried large-scale iron ore bodies both in Panzhihua and Baima, because such large measured anomalies cannot be produced by the proven iron ore bodies or the gabbro surrounded them. The Panzhihua and Baima iron ore bodies extend to larger depth level and as shown in Figure 7 and 8. On the whole, the Panzhihua and Baima iron deposit consists of a several layered iron bodies.

The proven iron ore bodies of Panzhihua iron deposit are situated on the southeast part of the iron ore layers and the volume only accounts for ~50% of the volume predicted by the inversion result. Therefore, we believe that there is a great potential to discover large iron ore bodies beneath the Panzhihua and Baima area. The exact results of the prospecting targets of Panzhihua and Baima area were confirmed according to the top projection of the inferred iron ore layers and the vertical first derivative of the magnetic field(Figure 10). According to the study, profiles 1-1', 2-2', 3-3' , 4-4'and 5-5' in Panzhihua have little potential in finding new iron ore deposits near-surface, only deep ores delow the known deposits are expectable. Profiles 6-6', 7-7', 8-8' and 9-9' proved to be most potential for the iron ore in Panzhihua area for the large volume according the study.

Similarly, profiles 2-2', 3-3', 4-4', 5-5'and 6-6' proved to be most potential for the iron ore in Baima area.

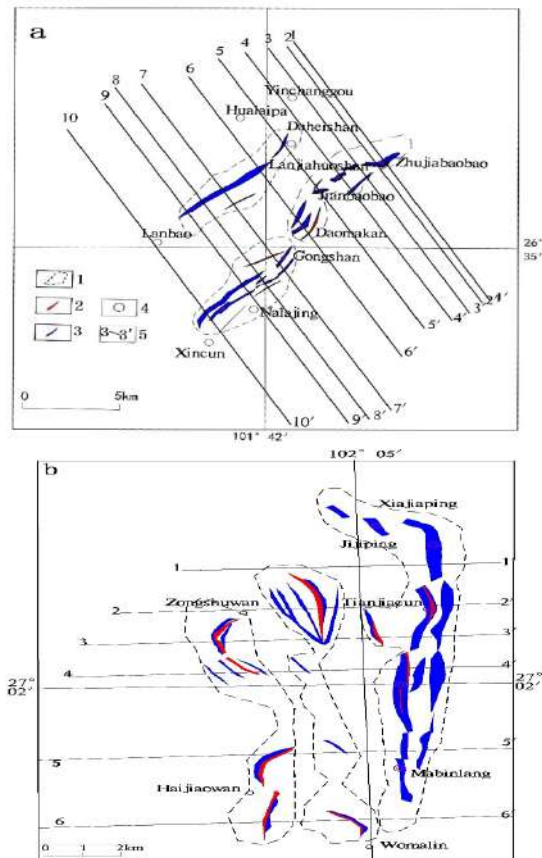


Figure 10: Prospecting targets in Panzhihua and Baima area.

1- Prospecting area; 2 - Prospecting targets(Rich ore); 3 - Prospecting targets(Lean ore); 4 - Locations; 5 - Inversion profiles.

6.2 Shape of Rock Bodies and Its Relationship with Ore Grade in the Panzhihua and Baima Area

Comparing the similarity and diversity between Panzhihua and Baima iron deposit, we concluded that the controlling factors of mineralization are similar: (1)the crystallization of Fe-Ti oxides from iron rich mafic magma in the earlier stage is the prerequisite of mineralization; (2)Gravity separation is the physical mechanism of the formation of Fe Ti oxide ore of vanadium titanium magnetite.

After the parent magma separated into silicate magma and Fe-Ti rich oxide ore melt (Zhou et al., 2005), the Fe-Ti rich magma migrated into Panzhihua and Baima rock body, Olivine, plagioclase and Fe-Ti oxides become liquidus

minerals, forming magnetite ore layer under the gravity variation.

According to the inversion results(Figure 8 and Figure 9),the shapes of Panzhihua rock body and Baima rock body show different characteristics in geometrical forms .In Panzhihua area , as a result of the obvious concave section at the bottom of the magma chamber and the smaller horizontal area of single rock body, the gravity separation of magnetite is more abundant in the process of magmatic flow, leading to the formation of thick massive ore(richer ore) in Zhujiabaobao area. Relatively speaking,in Baima area the bottom of the magma chamber is relatively gentle, and the horizontal area of single rock body is larger , gravity separation is not abundant ,thus formed dense disseminated ore(leaner ore).

6.3 Genesis of Panzhihua Type V-Ti Magnetite Deposits

Different explanations were given for the ore forming proce ss including immiscibility (Zhou et al., 2005), fractionation (Pang et al., 2008) and assimilation (Ganino et al.,2008). Large contact aureoles, mostly composed of brucite marbles and calc-silicate rocks, developed at the contact of the intrusions (Zhou et al., 2008).

Based on the inversions we conducted, we measured the length of the contact aureole on each inversion profiles to make some conservative estimates of the dimensions of the part of the aureole that underwent partial decarbonatization, the thickness was estimated as 300 m. The volume of the aureole between two profiles can be calculated as prismoid or frustum of a pyramid, giving a total volume of 13.6 km³. If the rock density is 2,750 kg/m³, the mass of the dolostone was 37.5Gt. If we assume that 80% of dolomite is transformed into brucite, then 190 g of CO₂ is released for each kilogram of rock (Ganino et al., 2008).The total amount of CO₂ is calculated as 5.7 Gt, which is similar to result Ganino obtained. However,90% of the aureole on the inversion profiles were located near Hualipa area, 6.2 kilometers northwest of the panzhihua deposit. Although large volume of blinded gabbro were inferred in Hualipa area, based on the inversions, the metallogenetic potential is low. How CO₂-rich fluids Interacted with the magma is hard to estimate, and the inversions above does not support the view that assimilation with carbonate rocks is vital condition in the formation of Panzhihua type V-Ti magnetite deposits.

7 CONCLUSIONS

Computation through forward and inverse methods of the magnetic anomalies of Panzhihua and Baima profiles have been conducted through interactive inversion technique. Our study leads to the following three major conclusions.

There is a potential to find large-sized iron ore bodies buried at depth in the Panzhihua and Baima area that remain to be discovered, the inversions we conducted provides prospecting targets for mineral exploration. According to the study, profiles 6-6', 7-7', 8-8' and 9-9' in Panzhihua area and Profiles 2-2', 3-3', 4-4', 5-5' and 6-6' in Baima area proved to be most potential for the iron ore.

The Panzhihua iron deposit is composed of thick massive ore and disseminated ore, while in Baima deposit only disseminated ore was found. The inversions indicated that such phenomenon could be explained by the different shapes of different magma chamber which related to the process of gravity separation of magnetite.

Based on the inversions, the quality of CO₂ released from dolomite that underwent partial decarbonatization is ~37.5Gt. Most of the aureole is located beneath Hualipa area where the metallogenetic potential is low, which probably mean that assimilation with carbonate rocks is not the vital condition in the formation of Panzhihua type V-Ti magnetite deposits.

ACKNOWLEDGEMENTS

Financial support for this work was provided by the The national key research projects(2017YFC0602206), 973 Program(Grant No. 2012CB416805) and Projects of the China Geological Survey Bureau Program (DD20160066, DD2016006637).

REFERENCES

- Fan Z G , Xu Z H, Tan L, Yang X, Zhang H R, Zhou D Q, Liu Q K and Tan L 2014 A study of iron deposits in the Anshan area, China based on interactive inversion technique of gravity and magnetic anomalies *Ore Geology Reviews* **57** 0618–0627
- Ganino C and Arndt N T 2009 Climate changes caused by degassing of sediments during the emplacement of large igneous provinces *Geology* **37** 323-326
- Ganino C, Arndt N T, Zhou M F, Gaillard F and Chauvel C 2008 Interaction of magma with sedimentary wall rock and magnetite ore genesis in the Panzhihua mafic intrusion, SW China *Mineralium Deposita* **43** 677-694
- Ganino C, Harris C, Arndt N T, Prevec S A and Howarth G H 2013 Assimilation of carbonate country rock by the parent magma of the Panzhihua Fe-Ti-V deposit (SW China): evidence from stable isotopes *Geoscience Frontiers* **4** 547-554
- Ge T F, Fan Z G, Huang X Z, Zhang Y J, He J Z and Li J J 2015 Deep metallogenetic potential and prospecting direction of Panzhihua V-Ti-magnetite deposit determined from aeromagnetic data analysis *Geology an Exploration* **51(6)** 1041-1048 (in Chinese with English abstract).
- He J Z, Fan Z G, Huang X Z, Ge T F and Yang R 2015 Three-dimensional inversion of magnetic data and geological modeling for the Hongge iron deposit *Geology and Exploration* **51(6)** 1049-1058 (in Chinese with English abstract)
- Pang K N, Li C, Zhou M F and Ripley E M 2008a. Abundant Fe-Ti oxide inclusions in olivine from the Panzhihua and Hongge layered intrusions, SW China: evidence for early saturation of Fe-Ti oxides in ferrobasaltic magma *Contributions to Mineralogy and Petrology* **156** 307-321
- Pêcher A, Arndt N T, Bauville A, Zhou M F and Ganino 2013 Structure of the Panzhihua Fe-Ti-V Deposit, China *Geoscience Frontiers* **4** 571-581
- Shellnutt J G, Wang K L, Zellmer G F, Iizuka Y, Jahn B-M, Pang K-N, Qi L and Zhou M-F 2011 Three Fe-Ti oxide ore-bearing gabbro-granitoid complexes in the Panxi region of the Emeishan large igneous province, SW China. *American Journal of Science* **311** 773-812
- Sui S W, Yu C C and Yao C L 2004 The semi-intelligent processing and interpretation software for gravity and magnetic anomalies along the profile of rolling topography and its application *Geophys. Geochem. Explor.* **28 (1)** 65–68 (in Chinese with English abstract).
- Sun D M 1991 Application of magnetic susceptibility meter in quality inspection of magnetite. *Metal Mine* **1** 9-11(in Chinese)
- Tian J and Fan M Q 2013 The mathematical model of correlation between magnetic material content and TFe grade in magnetite *China Mining Magazine* **22(10)** 105-108(in Chinese)

- Yu C C, Fan Z G, Wang N D, Xiong S Q, Wan J H and Zhang H R 2007 High-resolution aeromagnetic exploration methods and their application in Daye iron mines *Prog. Geophys.* **22** (03) 979–983 (in Chinese with English abstract)
- Zhang X Q, Song X Y, Chen L M and Xie W 2012 Fractional crystallization and the formation of thick Fe–Ti–V oxide layers in the Baima layered intrusion, SW China *Ore Geology Reviews* **49** 96–108
- Zhou M F, Arndt N T, Malpas J, Wang C Y and Kennedy A K 2008 Two magma series and associated ore deposit types in the Permian Emeishan large igneous province, SW China *Lithos* **103** 352–368
- Zhou M F, Arndt N T, Malpas J, Wang C Y and Kennedy A K 2008 Two magma series and associated ore deposit types in the Permian Emeishan large igneous province, SW China. *Lithos* **103** 352–368
- Zhou M F, Robinson P T, Lesher C M, Keays R R, Zhang C J and Malpas J 2005 Geochemistry, petrogenesis and metallogenesis of the Panzhihua gabbroic layered intrusion and associated Fe-Ti-V deposits, Sichuan Province, SW China *Journal of Petrology* **46** 2253–2280